UNIVERSITY OF Southampton

THESIS FOR THE DEGREE OF DOCTOR OF PHILOSOPHY

Polariton Condensates in Optical Traps and Strong Magnetic Fields

Author: ALEXIS ASKITOPOULOS

Supervisor: Prof. Pavlos LAGOUDAKIS

Laboratories for Hybrid Opto-electronics

School of Physics and Astronomy

Declaration of Authorship

I, ALEXIS ASKITOPOULOS, declare that this thesis entitled, 'Polariton Condensates in Optical Traps and Strong Magnetic Fields' and the work presented in it are my own and have been generated by me as the result of my own original research. I confirm that:

- This work was done wholly or mainly while in candidature for a research degree at this University.
- Where any part of this thesis has previously been submitted for a degree or any other qualification at this University or any other institution, this has been clearly stated.
- Where I have consulted the published work of others, this is always clearly attributed.
- Where I have quoted from the work of others, the source is always given. With the exception of such quotations, this thesis is entirely my own work.
- I have acknowledged all main sources of help.
- Where the thesis is based on work done by myself jointly with others, I have made clear exactly what was done by others and what I have contributed myself.

Signed: _____

Date: _____

Acknowledgements

The work presented herein would not have been possible without the invaluable help and support, of a number of people. First and foremost I owe a special debt of thanks to Professor P.G. Lagoudakis for his valuable insight and inspiration to undertake this research and for his continuing support with constructive criticism, incisive arguments and thoughtful advise. I have to thank Professor P. Savvidis for initiating me in the fascinating realm of polariton physics during my master's thesis and for his encouragement and sound suggestions that opened the way to the present research. I am also deeply indebted to Dr. S. Tsintzos for infusing in me good experimental practices that have enabled me to implement the experiments required for the completion of this thesis. I also have to acknowledge Dr. Hamid Ohadi for cultivating and elevating my lab and analysis skills. A special thanks to Tom Perkins, Justin Harris and Colin Miles for keeping the liquid helium supply going. The ingenious support of the mechanical workshop staff also deserves my sincere thanks for designing and producing a number of devices used throughout my research years in Southampton, especially Damon Grimsey for implementing a novel cold finger insert tube for the magnet setup. Of course all my colleagues from the Hybrid Photonics group, Elena, Junis, Mael, Pasquale,Matteo and Giacomo, for all their support understanding and friendship. Last but not least, a heartfelt thanks to my family, my mother Eleni for instilling in me common sense and always believing in me, my wife and partner in life Katerina for brightening up my life and my son Odysseas for inspiring me to achieve my fullest potential.

Dedicated to Odysseas
May you find your own Ithaka

UNIVERSITY OF SOUTHAMPTON

Abstract

Laboratories for Hybrid Opto-electronics
School of Physics and Astronomy

Polariton Condensates in Optical Traps and Strong Magnetic Fields

by ALEXIS ASKITOPOULOS

Semiconductor Microcavities in the strong coupling regime are an ideal test bed for studying light matter interactions at the micro-scale. The eigenstates of these systems, exciton-polaritons, are bosonic hybrid light matter quasi-particles that have been demonstrated to undergo Bose condensation. Owing to their photonic component polaritons are lighter than atoms so their Bose-Einstein condensation (BEC) is attainable at higher temperatures than traditional BEC phase transitions in atomic systems, while the reduced dimensionality of the system has the implication that the BEC phase transition spontaneously occurs only in the presence of a confining potential. In this thesis, the underlying mechanisms of polariton condensation in optically imprinted trapping potential landscapes is examined. Condensation in the ground state of an optical trap, de-localised from the excitation light is demonstrated and investigated and the confined condensate is shown to exhibit well defined quantum mechanical properties. A comparative study of the observed spectral features with a condensate formed with typical non-resonant excitation methods is conducted revealing a significant reduction of the excitation density threshold due to efficient trapping and relaxation of polaritons inside the trap. Decoupling of the optically induced excitonic reservoir results in increased temporal coherence in this system by suppression of the strong interactions with un-condensed particles. Modification of the geometrical properties of the trap results in single excited-state condensation. Contrary to defect and stress induced trapping schemes the condensation process is here driven by polaritons injected into the potential-trap from the trap barriers. This leads to more efficient pumping of the energetically higher modes extending into the trap boundary. We demonstrate how this feature can be exploited to manifest transitions between energetically neighbouring coherent quantum states in the steady state dynamic equilibrium regime and in the transient domain were the intensity tuning of coherent tunnelling modes is also examined. A by-product of the localisation of the condensate inside the photonic trap and the decoupling from the reservoir is the strong susceptibility of this system to small imbalances in the optical pumping of spin states. The population of the two spin states of the condensate can be controlled by small

imbalances of the circular components of the excitation. The high density regime in this configuration is then investigated where a linearisation of the polariton dispersion is observed under pulsed excitation. However, a vigorous examination of the transient dynamics in this regime demonstrates the artificial nature of this effect due to transient relaxation and momentum narrowing in the transition from photon lasing to a confined polariton condensate. The confined condensate is an ideal subject for studying strong magnetic field effects on the spin properties of polariton condensates as it emits in a single energy mode for a wide range of excitation powers above threshold compared to the "untrapped" case and doesn't suffer from de-coherence effects induced from the reservoir that causes line broadening and inhibits the spectral resolution of the spin components. We have performed initial reference strong magnetic field experiments with "unconfined" polariton condensates and present the predicted density dependent collapse of the Zeeman splitting and the modulation of the previously observed paramagnetic screening by the polarisation of the exciting beam. In the final chapter of the thesis we investigate the modulation of the condensation threshold for the non-optically confined case by the application of a magnetic field in the Faraday geometry. The experimental observations are explained by a model based on the suppression of diffusion in the reservoir and the shrinking of the Bohr radius by the application of the magnetic field.

Contents

List of Figures

Abbreviations

LASER	**L**ight **A**mplificaiton by **S**timulated **E**mission **R**adiation
VCSEL	**V**ertical **C**avity **S**urface **E**mitting **L**aser
GaAs	**Ga**llium **Ars**enide
AlAs	**Al**luminium **ArS**enide
LED	**L**ight **E**miting **D**evice
DBR	**D**istributed **B**ragg **R**eflector
CdTe	**C**a**d**mium **Te**lluride
TE,TM	**T**ransverese **E**lectric, **T**ransverese **M**agnetic
QW	**Q**uantum **W**ell
DOS	**D**ensity **o**f **S**tates
FWHM	**F**ull **W**idth at **H**alf **M**aximum
AOM	**A**cousto **O**ptic **M**odulator
NA	**N**umerical **A**perture
TEM	**T**ransmission **E**lectron **M**icroscopy
FWHM	**F**ull **W**idth at **H**alf **M**aximum
NA	**N**umerical **A**preture
CCD	**C**harged **C**oupled **D**evice
OPO	**O**ptical **P**arametric **O**scillator
FG	**F**unctionl **G**enerator

Introduction

The semiconductor age

It is widely acknowledged that semiconductor devices have given rise to the technological marvel of modern day electronics that have increasingly encompassed almost every aspect of people's lives in the last three decades. Infrared lasers pulse optical data through a global network of silica optical fibres; light-emitting diodes illuminate our homes and backlight liquid-crystal displays in our phones, tablets and televisions; visible lasers store and read data in DVDs; photovoltaic cells harvest clean energy from the sun. Every one of these technologies were made possible by advances and paradigm-shifts in the physics and understanding of semiconductor materials and devices.

Although semiconductors have only recently been the focus of increasing scientific research, the history of semiconductivity spans centuries. The first use of the term "semiconducting" dates back to the 18^{th} century and is attributed to Alessandro Volta [1], but it was not until 1833 that a semiconducting effect was recorded for the first time by Michael Faraday, who observed that, contrary to metals, the electric resistance of silver sulphide decreased with temperature [2]. The next quantum leap in semiconductor physics emerged when the study of the fundamental properties of Silicon and Germanium in 1946 actualised in the invention of the transistor at Bell Labs in 1947 by John Bardeen, Walter Brattain and William Shockley [3, 4]. This discovery coupled with the subsequent invention of the integrated circuit, where a number of transistors and electronic devices are incorporated onto a common silicon substrate, changed forever the field of electronics. Since then, the advances in the understanding of the underlying physics of the microcosm (and nano-cosm), incited by the establishment of the theory of quantum mechanics in the first half of

the 20^{th} century have been monumental, and resulted in the spectacular increase of the applications of semiconductor devices in modern technology.

From electronics to optoelectronics and photonics

The concept of combining optics with electronic signals in semiconductor devices gave birth to a new scientific discipline, that of opto-electronics. The use of indirect band-gap materials like silicon was not favourable for this type of devices as absorption of optical signals in these systems requires the simultaneous absortpion of a phonon in order for and energy an momentum conservation to be achieved. Therefore absorption of a photon in indirect semiconductors is effectively a three particle process (photon, electron, phonon) and will have a considerably lower probability than a two particle absorption (photon,electron) process that is the case for direct band-gap semiconductors. This fact established III-V semiconductor alloys, that exhibit a direct band-gap, as the preferential architecture for optoelectronic devices. The invention of the laser in 1960 [5] gave new momentum to this emerging field especially following the demonstration of the first GaAs based semiconductor laser a couple of years later [6]. In the late 1970s, the first operational VCSEL device was engineered [7], that demonstrated lasing in the weak coupling regime.

To polaritonics and spintronics

Current optoelectronic technologies exploit the advances in the fabrication of semiconductor heterostructures in order to separately manipulate charged carriers and photons. Arguably, coupling together photons and electrons in Bosonic states called "polaritons" and coherently controlling these hybrid quantum quasi-particles can bring about the next paradigm shift in semiconductor physics and devices. Polaritons posses hybrid properties of photons and excitons, combining the mobility and flexibility of light, with the possibility of interactions due to the matter component. Indeed, their physics is quite different from the physics of Fermionic electrons and holes in a semiconductor, on which current optoelectronic devices are based. At high densities, or low temperatures, polaritons collectively collapse into a macroscopic coherent quantum state, a polariton condensate, or a polariton laser. Such a coherent state shows much of the same physics as Bose Einstein Condensation, that has been observed in ensembles of cold atoms decoupled from the requirement of ultra-low temperatures required for these systems.

The history of polaritons dates back to 1958, when Hopfield in a landmark publication set the theoretical basis for the field of polaritons, demonstrating that the

excitonic field can interact with the electromagnetic field of a crystal structure under certain conditions and give rise to new system eigenstates that are a mixture of both excitons and photons [8]. These intriguing quasi particles were initially indirectly probed, in semiconductors, by means of resonance Raman scattering (1979) and through their luminescence [9, 10]. However the definitive experimental observation had to wait until 1992 when Weisbuch and co-workers [11] clearly observed the Rabi splitting of these new eigenstates in a semiconductor microcavity. This experimental realisation established semiconductor microcavities as ideal systems for studying light-matter interactions in the micro scale. The scientific interest for polaritons culminated with the theoretical suggestion of non-linear effects such as condensation and lasing in 1996 [12] and a few years later by the subsequent demonstration of polariton parametric amplification, in a GaAs microcavity at cryogenic temperatures, by Savvidis and co-workers [13]. One year later scientists from EPFL documented this process also in CdTe samples at much higher temperatures of 220K [14]. These experiments confirmed the bosonic nature of exciton-photon polaritons raising expectations for the realisation of polariton condensates and for the development of ultra-low threshold lasing devices.

The prediction of the Bose phase transition was introduced by Bose and Einstein in the first quarter of the 20^{th} century [15, 16]. However it was not until 1995 that the first observation of this unique phase transition was demonstrated in a gas of atoms [17–19]. This paved the way for the pursuit of Bose condensation in solid state systems as well. Polaritons, being bosons, and featuring a very light mass were perfect candidates for solid state condensates and in 2006 polariton Bose-Einstein condensation in cryogenic temperatures in a CdTe microcavity was demonstrated [20]. This discovery was quickly followed by the demonstration of polariton lasing at room temperature in a GaN microcavity [21]. The term polaritronics was introduced [22] following the first demonstration of a strongly coupled GaAs LED device operating close to room temperature [23]. This was an important breakthrough as efficient electrical injection of carriers into microcavities was considered a great challenge, while non-cryogenic temperature operation in the strong coupling regime for GaAs based samples was not considered possible because of the insufficient binding energy of the exciton. In recent years polariton devices have come even more in the spotlight with the appearance of the first electrically pumped exciton-polariton lasers operating from cryogenic [24, 25] to room temperature [26] that hold the promise of the realisation of highly efficient ultra low threshold solid state lasing, as well as the fabrication of novel optoelectronic devices.

Polariton condensates have also been proposed for the realisation of spinoptronic devices. Spinoptronics generally deals with the active manipulation of spin degrees of freedom within a solid state system with the aim of realising devices based on spin transport [27]. Early work on the understanding of spin transport in solid

state systems dates back to Mott and 1936 [28] and was mainly oriented towards the study of these phenomena in metals. However semiconductors have recently emerged as possible architectures for the implementation of spin-logic devices. In this regard, polariton microcavity systems are a unique laboratory due to the efficient spin to photon polarisation conversion, making spin anisotropies straightforward to detect and also due to their demonstrated spin multi-stabilities [29] that can lead to the implementation of polariton spin-logic devices.

Thesis outline

The object of this thesis is to study the fundamental properties and the underlying physical mechanisms of the formation of polariton condensates in optically "sculpted" potential traps. For particles inhabiting a two dimensional plane, a pure Bose-phase transition can theoretically manifest only in the presence of a trapping potential that modulates the density of states. Recent landmark studies in polariton condensates have underlined the remarkable possibility of optically imprinting arbitrary potentials to confine polariton condensates and modulate their propagation. These results triggered the experimental investigations described here.

In the first part of this thesis (part I) an overview of the physics associated with polariton condensates is presented as well as the description of the samples and of the experimental methods used. Chapter 1 details the basic concepts regarding the individual building blocks comprising semiconductor microcavities and gives a brief description of the physics of light matter coupling in these systems. Chapter 2 outlines the basic physics regarding Bose-Einstein condensates and the implications of this phase transition in reduced dimensionality systems. A short review of the pioneering works that eventually culminated in the demonstration of polariton BEC is presented followed by the experimental particularities of polariton condensates as well as the current theoretical framework that describes these coherent light-matter ensembles. A review of the main phenomena associated with polariton condensation is also presented. Finally an extensive discussion on the origin of the experimental "fingerprints" used to identify oblique dark solitons in the wake of a propagating polariton condensate is presented.

Chapter 3 describes the materials and methods used throughout the experiments conducted within the framework of this thesis. The experimental configurations are presented and described, while the second part of the chapter gives a description of the state of the art microcavity samples that were employed, where a novel strain compensated microcavity sample is characterised together with experimental evidence of polariton condensation in this system.

The experimental results on polariton condensation in optically induced potential traps are extensively presented in the second part (part II) of the thesis. In chapter 4 the initial results on the formation of a polariton condensate in an optically induced two-dimensional parabolic potential are presented along with a detailed comparative study with typical condensation formation in the same system. The dependence on the geometric properties of the potential to the resulting condensate mode are documented in chapter 5, where non-ground state condensation in excited higher order coherent bound states is also reported. A mode selection rule is proposed and effectively tested in the dynamic equilibrium and transients domains. Chapter 6 gives an overview of the fascinating spin properties of ground state condensation as well as a robust interpretation of these phenomena. Lastly the high density regime and the transition to photon lasing are examined in chapter 7. A dispersion linearisation in this regime is found to be an artificial feature rather than demonstration of a Bogoliubov excitation spectrum.

In the final part (III) of the thesis we investigate the magnetic field effects on the formation and spin of polariton condensates. In Chapter 8, we investigate the density dependent modulation of the paramagnetic screening of the field by a polariton condensate by studying the Zeeman splitting of the system under CW excitation with linear and circular polarizations. In chapter 9 experimental results on the formation of polariton condensates under magnetic fields are presented and explained, where the importance of diffusion of carriers outside the pumping region as well as the implications of this on the condensation threshold is analysed. As the formation of the optical trapping potential is driven by diffusion of optically injected carriers outside the pumping region the application of a magnetic field can be an important tool in modulating the shape of an optical polariton trap.

Part I

Physics of Semiconductor Microcavities Experimental Techniques and Description of Samples Studied

CHAPTER 1

Light Matter Coupling in Semiconductor Microcavities

In order to realise strong interactions between photons and excitons, it is essential to confine them effectively in relatively small volumes as long as possible. This is accomplished most efficiently using Fabry-P$\acute{e}$rot resonators with high reflectivity mirrors. In these structures, a cavity volume is placed between two parallel asymmetric reflectors. The cavity spacer is imbued with an excitonic resonance designed to resonate with the cavity mode. When the appropriate phase matching conditions are met, photons and excitons strongly couple to form the new eigenstates of the system: exciton-polaritons.

1.1 Building blocks

A semiconductor Microcavity consists of an active region that has an optical length equal to an integer of half the cavity wavelength λ that is placed between a pair of high reflectivity mirrors. While metallic mirrors have been used in polariton microcavity structures the most common option is the use of distributed Bragg reflectors (DBRs) because of their higher reflectivity efficiency. While there is a variety of semiconductor materials that have been used over the years for the fabrication of microcavities, here we will focus mainly on AlGaAs alloys as the samples studied in this thesis were from this family of materials.

1.1.1 Distibuted Bragg Reflectors

A Distributed Bragg Reflector consists of alternating layers of two materials with different refractive indices. The working principle relies on constructive and destructive interference of the transmitted and reflected waves. Electromagnetic (EM) waves propagating in the transmission direction interfere destructively while the ones reflected by the consecutive interfaces interfere constructively. The successive layers are engineered to have an optical length of $\lambda/4$, where λ is the so called Bragg wavelength corresponding to the centre of the high reflectivity band. This high reflectivity region formed for a bandwidth of frequencies (wavelengths) around λ is conversely named the photonic stop band. The characteristics of the stop-band width and reflectivity depend on the refractive index contrast between the individual layers and the number of periods in the structure. The optical properties of these structures can be calculated by the Transfer matrix method. The basic principle behind this method is to attribute a matrix element to each layer of the structure, effectively describing the EM wave arriving and passing through the layer [30, 31]. Using this model a simulation of the Electric field intensity inside a GaAs/AlAs DBR is shown in fig. 1.1. The figure depicts the field in the first 23 pairs of the total 40 of the structure.

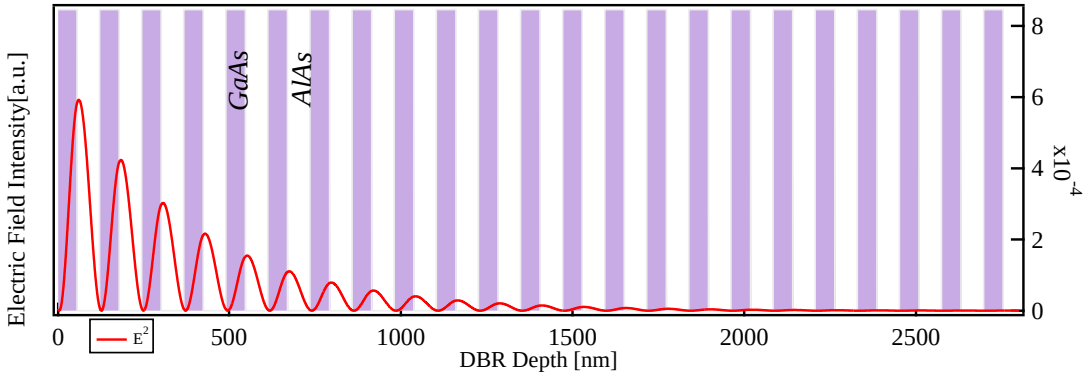

FIGURE 1.1: Transfer Matrix simulation of the Electric Field intensity inside a GaAs/AlAs Distributed Bragg reflector with 40 pairs, for light incident from the left of the structure, for $\lambda = 820nm$.

As seen in Fig. 1.1, although the intensity of the field quickly goes to zero inside the structure, nonetheless there is a finite area where its magnitude is substantial. This is quantified by the so called DBR penetration length which is given by:

$$L_{DBR} = \frac{\lambda_0 n_L n_H}{2n_i(n_H - n_L)} \tag{1.1}$$

where n_H and n_L are the refractive indices of the high and low index materials respectively while n_i is that of the medium from which the light is incident to the DBR structure [32, 33]. The calculated reflectivity spectrum of this structure for

normal incidence is shown in figure 1.2a (red line) where the high reflectivity region is clearly distinguishable between 770nm and 850nm. Simulations of structures with different numbers of pairs are also shown for comparison, while figure 1.2b presents a parametric simulation of the stop band for a varying number of pairs from two to 80. The low reflectivity modes at the edges of the reflectivity stop-band are usually referred to as leaky modes [34].

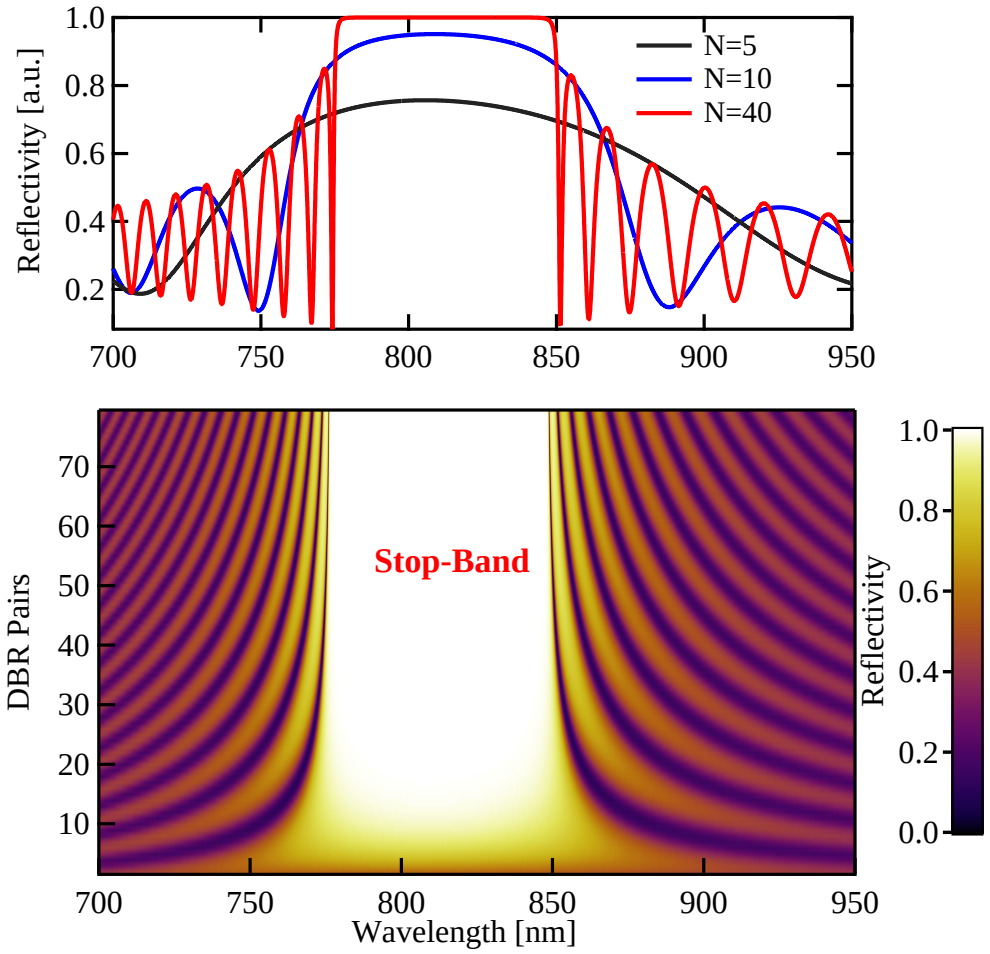

FIGURE 1.2: Transfer Matrix simulations of the reflectivity spectrum at normal incidence of a GaAs/AlAs DBR for varying number of layer pairs. Reflectivity spectrum for N=5 (black line), N=10 (blue line) and N=40 (red line) top panel. Bottom panel, parametric image of reflectivity for N=2 to N=80.

Another important property of DBR stacks is that the reflectivity stop-band has an inherent angular dispersion. That is the stop-band centre varies with increasing angle of the incident light. The reason behind this is that these mirrors rely on an interference condition that is angle dependent. Furthermore this angular dispersion is also different for transverse electric and transverse magnetic electric fields. Figure 1.3 illustrates the angular dispersion of the structure of fig. 1.1 for TE and TM incident light.

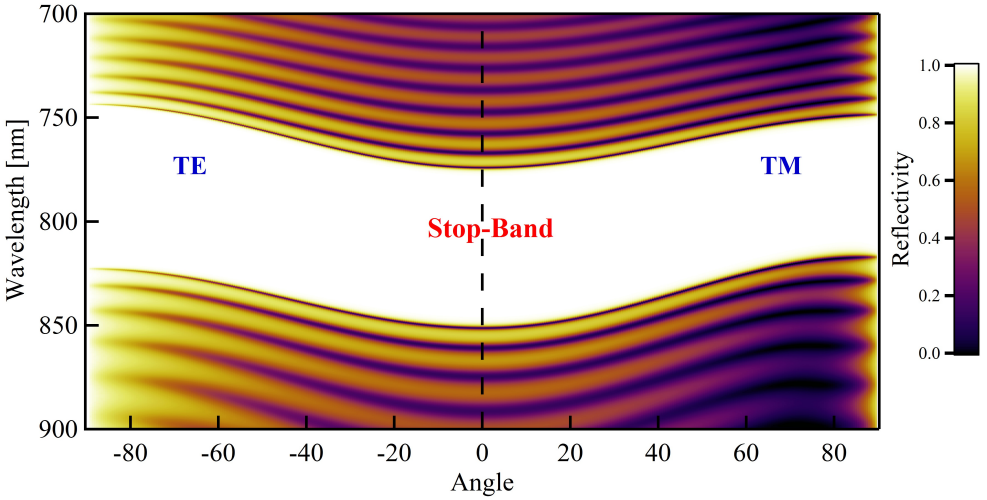

FIGURE 1.3: GaAs/AlAs DBR angle dispersion with 40 pairs. Negative angles for TE mode and positive for TM.

Analytical expressions for the reflective properties of DBR stacks in the limit of high reflectivity are already well established and can be used for calculation of the optical properties of interest. The stopband width is given by:

$$\Delta\lambda = \frac{2\lambda\Delta n}{\pi n_{eff}} \tag{1.2}$$

where Δn is the difference between the high and low refractive index and n_{eff} is the effective refractive index of the structure [34], while the reflectivity maximum R at the center of the stopband is:

$$R = \left(\frac{1 - \frac{n_{out}}{n_{in}} \left(\frac{n_L}{n_H} \right)^{2p}}{1 + \frac{n_{out}}{n_{in}} \left(\frac{n_L}{n_H} \right)^{2p}} \right)^2 \tag{1.3}$$

where p is the number of pairs, n_{in}, n_{out}, n_L and n_H are the refractive indices of the incident, transmitted side, low and high materials respectively.

1.1.2 Fabry-Pérot Microcavities

The French scientists Charles Fabry and Alfred Pérot were the first to implement an interferometer composed of two higly reflective parallel mirrors. Such a device was initially used in spectroscopic measurements in order to spectrally resolve ultra narrow linewidths due to its high finesse. It is feasible to create a Fabry-Perot cavity with semiconductors by placing two Bragg mirror stacks around a cavity spacer. Photons inside such a cavity are free to propagate parallel to the mirror plane but are confined in the perpendicular direction. The photonic confinement along this axis compels the photon wavevector k along this axis to take discrete

values $k_z = N\pi/L_c$, where L_c is the cavity length and N a positive integer. Therefore photons inside the cavity have a total wavevector of $k^2 = k_z^2 + k_{\|}^2$ and energy dispersion:

$$E_N(k_{\|}) = \frac{\hbar c}{n_{cav}} \frac{N\pi}{L_c} \sqrt{1 + \frac{L_c k_{\|}}{N\pi}} \tag{1.4}$$

where n_{cav} is the cavity index of refraction.Eq. 1.4 by Taylor expansion yields

$$E_N(k_{\|}) = E_{N,0} + \frac{\hbar^2 k_{\|}^2}{2m_{ph}^*}, \tag{1.5a}$$

$$E_{N,0} = \frac{N\pi\hbar c}{n_c L_c}, \tag{1.5b}$$

$$m_{ph}^* = \frac{N\pi\hbar n_c}{cL_c} \tag{1.5c}$$

$E_{N,0}$ is the photon energy with zero in-plane wavevector, while m_{ph}^* is the effective mass of photons moving in the plane of the cavity. The differences of the exact formula(1.4) and the effective mass approximation obtained after the Taylor expansion are negligible for angles under 90 degrees.

The cavity Finesse is defined as:

$$\boldsymbol{F} = \pi \frac{\sqrt{R_1 R_2}}{1 - R_1 R_2} \tag{1.6}$$

where R_1 and R_2 are the reflectivities of the two cavity DBRs [35]. Of interest is also the cavity quality factor which is directly linked to the photon lifetime. It can be deduced through the *F*inesse as $\boldsymbol{Q}$=N$\boldsymbol{F}$ but is defined as $\boldsymbol{Q} = 2\pi \mathrm{v} \frac{Energy\ stored}{Power\ loss}$ (where v is the cavity frequency) and more conveniently as the ratio between the mode energy and the energy width of the specific mode of a given cavity.

$$\boldsymbol{Q} = \frac{E_0}{\Delta E} \tag{1.7}$$

More importantly it can give a direct estimation of the photon lifetime in the cavity:

$$\boldsymbol{Q} = 2\pi\nu\tau \tag{1.8}$$

with ν the photon frequency and τ the photon lifetime [36]. The transfer matrix method can be used to simulate the optical properties of semiconductor microcavities. Fig. 1.4 depicts the calculated Electric field intensity in the middle part of a GaAs λ cavity composed of GaAs/AlAs DBRs with 30 pairs top (left) side and 32 in the bottom (right side), for the cavity wavelength. The electric field intensity is maximum in the cavity layer and quickly diminishing in the DBRs. It is worth mentioning that the effective cavity length is modulated by the penetration of the

field in the mirrors and should now be regarded as:

$$L_{eff} = Lc + L_{DBR1} + L_{DBR2} \tag{1.9}$$

where L_{DBR1} and L_{DBR2} is the penetration of the field in the cavity mirrrors.

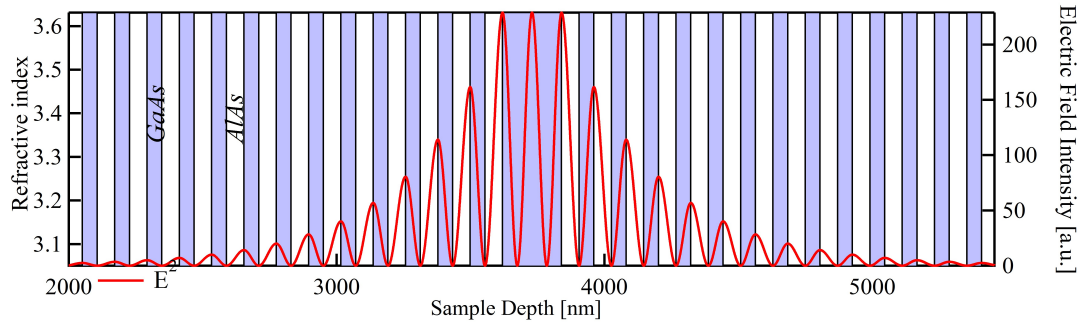

FIGURE 1.4: Transfer Matrix simulation of the Electric Field intensity in a λ GaAs cavity with $GaAs/AlAs$ DBRs of 30 and 32 pairs. Incident direction from left to right.

The reflectivity spectrum of the simulated cavity can be seen in figure 1.5. Introducing the cavity region between the two DBRs gives rise to the cavity resonance at $\lambda_c = 800nm$ as evidenced by the sharp dip in the reflectivity stop band.

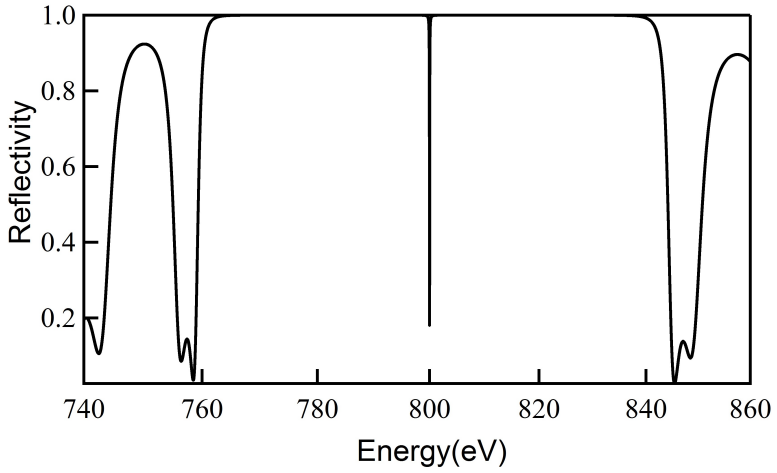

FIGURE 1.5: Simulated reflectivity spectrum of GaAs cavity with $GaAs/AlAs$ DBRs of 30 and 32 pairs.

An angle parametric transfer matrix simulation reveals the parabolicity of the angular dispersion of the cavity. Figure 1.6 depicts the reflectivity spectrum of the simulated microcavity structure for both TE (negative angles) and TM modes reflected modes (positive angles). The slight difference in energy between the TE and TM modes of the cavity are conventionally named the longitudinal-transverse splitting.

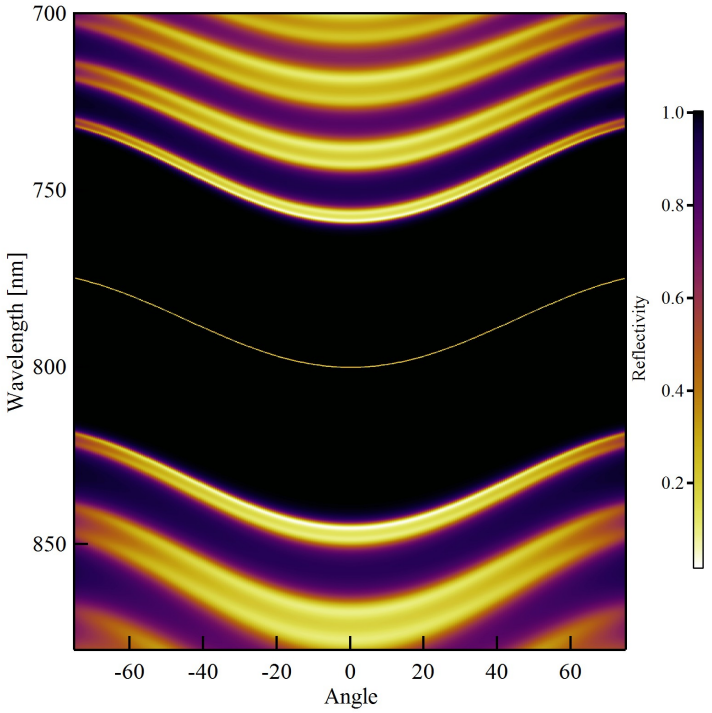

FIGURE 1.6: Simulated angular dispersion of a GaAs cavity with $GaAs/AlAs$ DBRs of 30 and 32 pairs. Negative angles for TE mode and positive for TM.

Depending on the quality of the DBRs, semiconductor microcavities have been realised for quality factors of more than 10000 with typical lifetimes on the order of 1-5 ps.

1.1.3 Excitons

In a direct band-gap semiconductor, an electron excited from the valence band to the conduction band will interact with the remaining electrons of the valence band. This introduces a correction to the repulsive potential of the filled valence band more commonly described by the attractive interaction between the valence band hole and the conduction band electron. This introduces an inter band gap energy that describes a bound electron-hole pair more commonly referred to as an exciton. Excitons depending on their radius are classified as Wannier Mott and Frenkel excitons. Frenkel excitons are more common in organic semiconductor structures where excitons are usually localised in a single molecule. Wannier-Mott excitons are typically found in inorganic semiconductors where the exciton radius is considerably greater than the lattice period [37]. In this thesis when we discuss excitons we refer to Wannier-Mott excitons since the microcavity samples studied where composed of inorganic semiconductors.

1.1.3.1 Bulk Excitons

In Bulk semiconductors under the effective mass approximation the energy dispersion of the valence and conduction band can be described by:

$$E_v(k_h) = -\frac{\hbar k_h^2}{2m_h^*}, \tag{1.10a}$$

$$E_c(k_e) = E_g + \frac{\hbar k_e^2}{2m_e^*} \tag{1.10b}$$

where m_e^* and m_h^* are the effective mass of the electron and hole respectively and E_g the band gap energy. Effectively an exciton is a hydrogen like atom moving in the atomic lattice. Therefore it is essential to introduce the relative position of electron and hole $\mathbf{r} = r_e - r_h$, the total mass $\mathbf{M} = m_e^* + m_h^*$, the center of mass position $\boldsymbol{R}=\frac{m_e^* r_e + m_h^* r_h}{m_e^* + m_h^*}$ and the reduced mass $\mu = \frac{m_e^* m_h^*}{m_e^* + m_h^*}$. The exciton *Hamiltonian* can now be written as:

$$\mathcal{H}_{exc} = \mathcal{H}_{cm} + \mathcal{H}_{rel} \tag{1.11a}$$

$$\mathcal{H}_{cm} = E_g + \frac{\hbar^2}{2M}\nabla_R^2 \tag{1.11b}$$

$$\mathcal{H}_{rel} = \frac{\hbar^2}{2\mu}\nabla_r^2 - \frac{e^2}{4\pi\epsilon_0\epsilon_r r} \tag{1.11c}$$

From where it is easy to deduce that the eigenstates of $\mathcal{H}_{cm}$ are plane waves while $\mathcal{H}_{rel}$ is a Hamiltonian similar to the one of the Hydrogen atom and therefore its eigenstates are orbitals similar to the hydrogen case.

$$E_{cm}(k) = E_g + \frac{\hbar^2 k^2}{2M} \tag{1.12a}$$

$$E_{rel,n} = -\frac{R_{exc}}{n^2} \tag{1.12b}$$

$$E_{exc} = E_g + \frac{\hbar^2 k^2}{2M} - \frac{R_{exc}}{n^2} \tag{1.12c}$$

where $R_{exc} = \frac{\mu e^4}{2\hbar^2(4\pi\epsilon_0\epsilon_r r)^2}$, n is the principal quantum number of the exciton orbitals and $k = k_e + k_h$ the exciton wavevector. This treatment allows to define the exciton Bohr radius as $a_{Bexc} = \frac{\hbar}{\sqrt{2\mu R_{exc}}}$. From 1.12 it is easy to see that the binding energy of the 1s exciton orbital is $E_B = R_{exc}$.

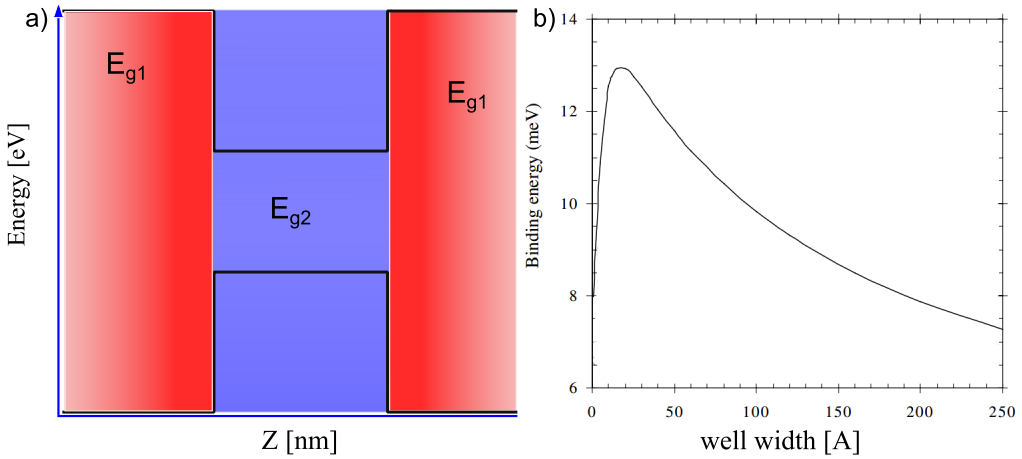

FIGURE 1.7: a) Schematic representation of a Quantum well Bandgap. b) Calculated 1s Exciton binding energy as a function of quantum well width for a GaAs/$Ga_{0.6}Al_{0.4}$As/GaAs quantum well, showing the non-monotonic dependence (exctracted from [38]).

1.1.3.2 Excitons in Quantum Wells

Quantum Wells (QW) are heterostructures composed of a thin layer, of the order of a few nano-meters, of a semiconductor material, usually placed in the middle of a material with a higher band gap used to confine carriers (fig. 1.7a). For efficient confinement of excitons in a QW, the layer thickness must be of the order of the bulk exciton Bohr radius. This inhibits movement along the z (growth) direction of excitons in the structure effectively confining them in this direction while leaving them free to propagate in the plane of the QW. Quantum confinement in QWs results in a significant increase of the exciton binding energy. The exact energy and wavefunctions of a QW exciton are difficult to solve analytically, but it can be shown with a straightforward variational approach that $a_{Bexc}^{2D} = \frac{a_{Bexc}}{2}$ and $E_B^{2D} \geq 4E_B$ [39, chap. 4]. Counter-intuitively the exciton binding energy is non-monotonic with increasing QW width (fig.1.7b), since for very small widths the electron and hole wavefunctions tunnel into the barriers and the confinement is considerably weakened [38, 39]. Furthermore, quantum well excitons are preferential for coupling with light in semiconductor microcavities since they can be positioned exactly at the maxima of the cavity electromagnetic field and so increase the probability of the cavity photon being absorbed to create an exciton. Finally, using quantum wells to increase the exciton binding energy to values larger than the thermal energy at room temperature allows for the observation of stable excitons at 300K which is vital for operational devices.

The exciton oscillator strength, which is a measure of the probability of absorption and emission of photons, is well known to be greatly increased in quantum well excitons compared to bulk excitons [40]. Using the $\mathbf{A}\cdot\mathbf{p}$ Hamiltonian [41] (where $\mathbf{A}$ is the vector potential and $\mathbf{p}$ the momentum operator) it can be shown that the

strength of the optical transition for the bulk exciton per unit volume and for a quantum well exciton per surface unit is:

$$\frac{f_{osc}^{xbulk}}{V} = \frac{2}{ME_{exc}} \left|\phi_{bulk}(0)\right|^2 \left|\langle u_e \left|p \cdot \epsilon\right| u_h\rangle\right|^2 \tag{1.13a}$$

$$\frac{f_{osc}^{2D}}{S} = \frac{2}{ME_{exc}} \left|\phi_{2D}(0)\right|^2 \left|\langle u_e \left|p \cdot \epsilon\right| u_h\rangle\right|^2 \left|\int \chi_h(z)\chi_e^*(z)dz\right|^2 \tag{1.13b}$$

where u_e and u_h are the Bloch amplitudes of the electron and hole, ϕ_{bulk} and ϕ_{2D} are the orbitals of the bulk and quantum well exciton respectively and ϵ is the polarisation vector of the electromagnetic field. Finally $\chi_h(z)$ and $\chi_e^*(z)$ are the electron and hole wavefunctions in the quantum well respectively. Due to the confinement, in quantum wells the overlap of electron and hole wavefunctions of an excitonic state is greatly increased, which in turn results in an enhanced oscillator for QW excitons compared to bulk excitons.

1.2 Light Matter Coupling

The first theoretical proposal that the optical properties of a system can be altered by the surrounding environment, was first made in 1946 by E.M. Purcell who proposed that the spontaneous emission rate of atoms is enhanced when they are placed in a resonant cavity [42], with the enhancement given by the Purcell factor:

$$F_P = \frac{3}{4\pi^2}\left(\frac{\lambda_c}{\eta}\right)^3\left(\frac{Q}{V}\right) \tag{1.14}$$

where Q is the quality factor, V the cavity mode volume and η the refractive index of the medium. Depending on the nature of the coupling of the active medium and the electromagnetic field, the emission of light can be differentiated in two distinct regimes. In the weak coupling regime an emitted photon has a minute probability of getting re-absorbed by the emitter and the energy of the system is quickly dissipated. In this regime the emission follows Fermi's golden rule for transitions to the cavity continuum of states. When the emitted photon has a high probability of being reabsorbed by the medium, before leaving the cavity, then the system is in the strong coupling regime. This regime is characterised by the continuous shifting of the excitation between the electromagnetic mode of the cavity and the excitation in the medium. This Rabi oscillation is damped by the inherent system de-coherence processes while the energy of the excitation dissipates within a time-scale of the order of the lifetime of the uncoupled states. Recently a third light matter coupling regime has been proposed. In the ultra-strong coupling regime, it has been predicted that when light-matter coupling becomes strong enough, the mixing of states breaks down and the Purcell effect is reversed [43]

1.2.1 Strong coupling of excitons and photons

In the strong coupling regime the eigenstates of the system are no longer the exciton and the cavity photon but a mixed state known as polariton. The experimental fingerprint of polaritons is their anti-crossing behaviour. Tuning the exciton resonance through the cavity by increasing the temperature of the system or by scanning across a built in wedge of the microcavity by changing position on the sample this characteristic behaviour can be observed. In the quantum description of light matter coupling, polaritons can be described as the eigenstates of this system that arise from the coupling of two oscillators, namely the QW exciton and the light mode of the cavity. The energy gap, called the Rabi splitting, resulting from this anti-crossing defines each polariton system and depending on the materials used ranges from 5-15 in GaAs structures to 50meV for GaN microcavities and to more than 100meV for ZnO and organic samples.

In the simplest form, disregarding decay terms, the Hamiltonian for uncoupled excitons and photons in the second quantisation representation reads:

$$H_{free} = \sum_{k_\parallel} E_x(k_{x\parallel}) b_{k\parallel} b^\dagger_{k\parallel} + \sum_{k_\parallel} E_c(k_{c\parallel}) a_{k\parallel} a^\dagger_{k\parallel} \tag{1.15}$$

where $b^\dagger_{k\parallel}$, $a^\dagger_{k\parallel}$ (,$b_{k\parallel}$, $a_{k\parallel}$) are the creation (annihilation) operators for excitons and cavity photons respectively. In this representation the exciton-photon interaction Hamiltonian is:

$$H_{int} = \sum_{k_\parallel} \hbar\Omega \left(b_{k\parallel} a^\dagger_{k\parallel} + b^\dagger_{k\parallel} a_{k\parallel} \right) \tag{1.16}$$

where $\hbar\Omega$ is the exciton-photon interaction strength. The eigenenergies of the system in the strong coupling regime are obtained by diagonalisation of the full Hamiltonian of the system ($H = H_{free} + H_{int}$):

$$E_{up}(k) = \frac{1}{2}\left(E_c(k) + E_x(k) + \sqrt{(E_c(k) - E_x(k))^2 + 4\hbar^2\Omega^2} \right) \tag{1.17a}$$

$$E_{lp}(k) = \frac{1}{2}\left(E_c(k) + E_x(k) - \sqrt{(E_c(k) - E_x(k))^2 + 4\hbar^2\Omega^2} \right) \tag{1.17b}$$

where E_{up} and E_{lp} denote the upper and lower polariton states. The difference in energy between the exciton resonance and the cavity mode (at $k_\parallel = 0$) is conventionally called detuning: $\delta = E_c(k_\parallel = 0) - E_x(k_\parallel = 0)$. The dispersion of the new eigenstates relative to the uncoupled ones for positive, negative and zero detuning for a system with a Rabi splitting of $2\hbar\Omega = 9meV$ is shown in fig. 1.8a,c,e. Polaritons can be described by the so called Hopfield coefficients that characterise the contribution of each uncoupled state to the new eigenstates [8], which for the lower polariton state is $E_{lp}(k) = X_{lp}(k)E_x(k) + C_{lp}(k)E_c(k)$ where $X_{lp}(k)$ and $C_{lp}(k)$

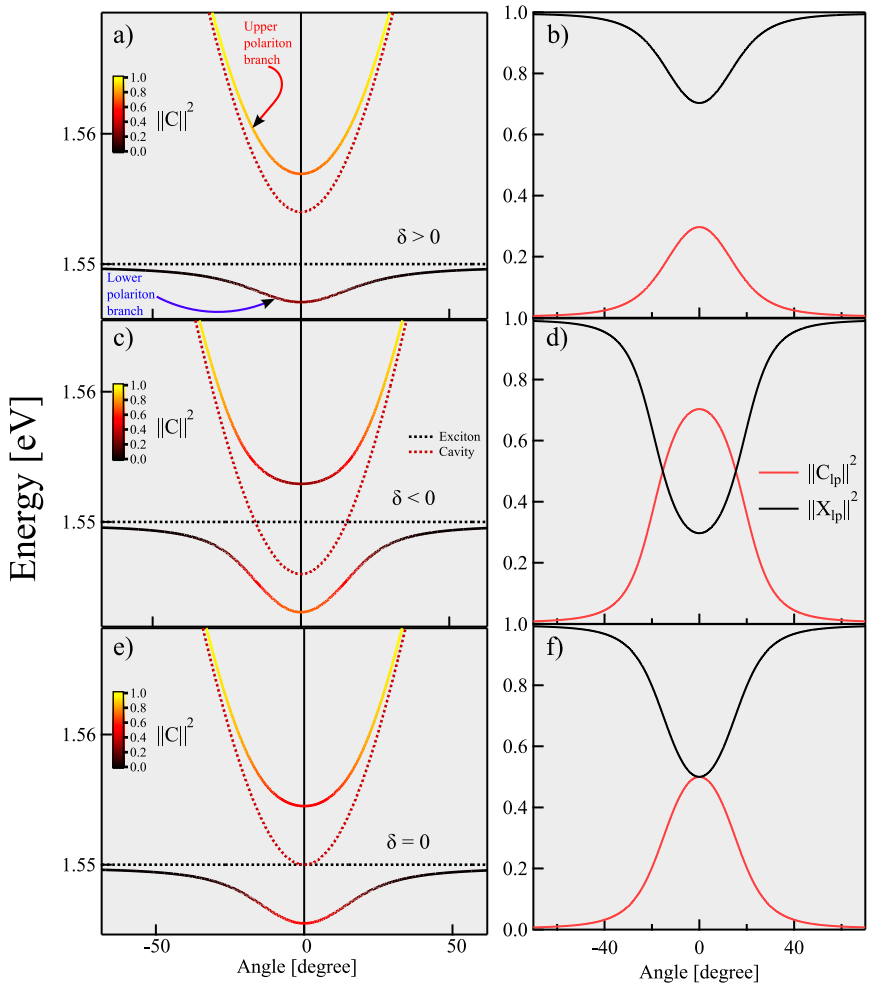

FIGURE 1.8: a),c),e) Angular dispersion of uncoupled exciton and cavity modes compared to the polariton coupled eigenstates for $\delta = -4meV$,$\delta = 4meV$ and $\delta = 0meV$ exciton cavity detuning respectively. The colour-scale for (upper and lower polariton modes) corresponds to the corresponding cavity Hopfield coefficient. b),d),f) Exciton and cavity Hopfield coefficients of the lower polariton branch

are the exciton and cavity Hopfield coefficients:

$$X_{lp}(k) = \frac{E_c(k) - E_x(k)}{\sqrt{(E_c(k) - E_x(k))^2 + \hbar^2\Omega^2}} \tag{1.18a}$$

$$C_{lp}(k) = -\frac{\hbar\Omega}{\sqrt{(E_c(k) - E_x(k))^2 + \hbar^2\Omega^2}} \tag{1.18b}$$

In fig. 1.8a the colour of the polariton modes corresponds to the cavity Hopfield coefficients, while the corresponding angular dispersion of both the exciton and cavity lower polariton coefficients is explicitly shown in fig. 1.8b,d,f.

The previous description is analogous to a coupled harmonic oscillator system. Taking into account the decay of photons in the cavity (γ_c) and the non-radiative broadening of the exciton in the system (γ_x) eq. 1.17 becomes [32]:

$$E_{up,lp}(k) = \frac{1}{2}\left(E_c(k) + E_x(k) - i\hbar(\gamma_x + \gamma_c) \pm \sqrt{(E_c(k) - E_x(k) - i\hbar(\gamma_x - \gamma_c))^2 + 4\hbar^2\Omega^2}\right) \tag{1.19}$$

For $\delta = 0$, it is easy to see that for $\gamma_c - \gamma_x \leq 2\Omega$ the square root is purely imaginary which signifies the transition to the weak-coupling regime where the exciton and cavity energies remain unperturbed and the only contribution is the enhancement of the decay rates. While for $\gamma_c - \gamma_x \geq 2\Omega$ the system lies in the strong coupling regimes

Strong coupling between photonic and excitonic states in vertical semiconductor microcavities is not exclusively limited to the coupling between cavity mode and QWs. In ZnO and GaN based structures for instance, were the binding energy of the bulk exciton has a strong oscillator strength, strong coupling between cavity photons and bulk excitons has been repeatedly demonstrated [21, 44]. Strong coupling has even been demonstrated in the absence of a pure cavity mode with QWs embedded within a DBR structure [45]. In these structures the light component is provided by the propagating Bragg (or leaky) mode that defines the end of the photonic stop-band, while parametric amplification processes have also been reported in these so-called Bragg-polaritons [46].

1.3 Polariton Spin and Polarisation

Polariton spin is determined by the spin of the coupled excitons of the system. Since excitons are composite particles, their spin is defined by their individual components. In zinc-blend crystal lattices (such as GaAs and CdTe) electrons in the conduction band have S-symmetry ($l = 0, s = 1/2$), while electronic states in the upper valence band have P-symmetry therefore featuring a six-fold degeneracy($l = 1, s = 1/2$) (fig. 1.9a). Taking into account spin-orbit coupling, leads to electronic states with total angular momentum $j = 3/2$ and $j = 1/2$ with the $j = 3/2$ states having a four-fold and the $j = 1/2$ ones having a two-fold degeneracy. Spin orbit coupling also opens an energy gap Δ_0 between the $j = 3/2$ and $j = 1/2$ states (fig. 1.9b). Conventionally the $j = 1/2$ band is called the spin-split-off band, while the bands with $j = 3/2$, depending if the spin projection is parallel or anti-parallel to the projection of the orbital angular momentum, are the so-called heavy ($m_j = 3/2$) and light hole ($m_j = 1/2$) bands respectively. In bulk structures the heavy and light hole bands are degenerate at k=0, but in 2D systems, like quantum wells, this degeneracy is lifted by quantum confinement in the growth direction. This results

in the phenomenon of "mass reversal" for the in plane motion of heavy and light holes. Although quantum confinement leads to a crossing of the light and heavy hole bands, in the Lüttinger-Kohn model, band mixing between the heavy and light hole bands results to anti-crossing of the two bands (fig. 1.9c) [47].

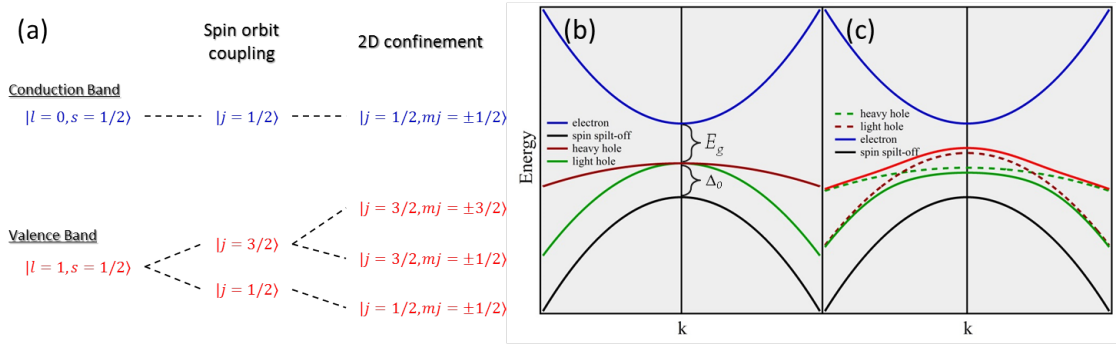

FIGURE 1.9: Schematic of valence and conduction band energy levels. **a)** Lifting of degeneracy of electron and hole levels due to spin orbit coupling and confinement. Electron, heavy hole, light hole and spin split-off band energy levels taking into account spin orbit coupling **b)**, quantum confinement and band mixing **c)**.

Excitons, are thus composite bosonic particles with integer spin of ±1 or ±2. An electron and a hole of a $s = \pm1$ exciton can recombine radiatively by emitting a photon of equal spin corresponding to left or right circular polarisation, while excitons with $s = \pm2$ are the so called dark states that are known to be optically inactive and can decay through non-radiative channels (fig. 1.10a). Nevertheless, dark excitons are optically created whenever electrons and holes are excited and their presence has a significant contribution in interactions with other excitons as well as polaritons.

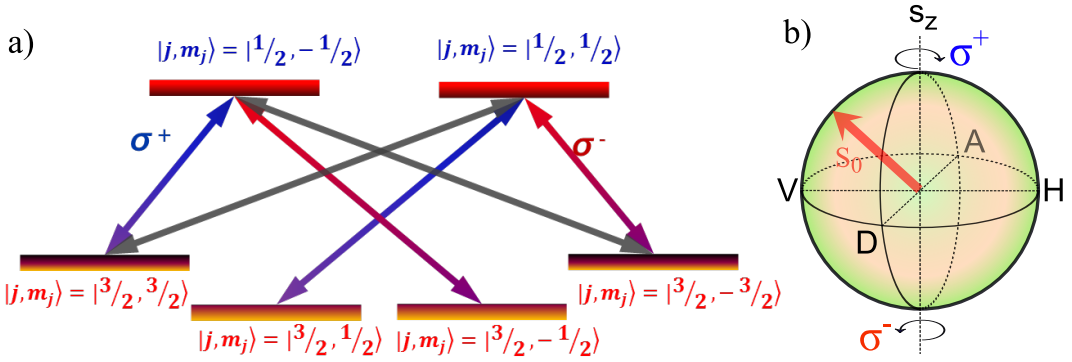

FIGURE 1.10: **a)** Transitions between electron and hole states. Blue (red) arrows denote the allowed optical transitions with σ^+ (σ^-) photon polarisation and grey arrows mark the dark transitions with exciton spin ±2. **b)** Polarisation representation in the Poincaré sphere. Circular and anti-circular polarisations correspond to the poles, while linear polarisation is mapped on the equatorial plane and intermediate latitudes to elliptical polarisation.

Polaritons thus posses spin ± 1 and when a photon escapes from a strongly coupled microcavity system, it will convey information regarding the spin of the polariton state it was emitted from in its polarisation. Compared to a particles spin, this is an easily measurable property, fully characterised by the stokes vector $\vec{S}$ that can be calculated by measuring its three components:

$$S_x = \frac{I_H - I_V}{I_H + I_V} \tag{1.20a}$$

$$S_y = \frac{I_D - I_A}{I_D + I_A} \tag{1.20b}$$

$$S_z = \frac{I_R - I_L}{I_R + I_L} \tag{1.20c}$$

where I_H, I_V, I_D, I_A, I_R and I_L are the intensities of the horizontal, vertical, diagonal, anti-diagonal, left circular and right circular polarisations respectively. S_x,S_y and S_z are thus proportional to the linear ,diagonal and circular polarization degree respectively. The total degree of polarisation (for an ensemble of photons) in this representation is given by $S = \sqrt{S_x^2 + S_y^2 + S_z^2}$. The three stokes components thus correspond to a three dimensional vector within the volume of a spherical surface known as the Poincar$\acute{e}$ sphere. This geometric representation of polarisation is similar to the Bloch sphere of a two level system that maps all complex superpositions of two pure quantum states on its surface. In the case of the Poincar$\acute{e}$ sphere the pure quantum states correspond to left and right handed circular polarisation of light (or polaritons with spin± 1) (fig. 1.10b).

CHAPTER 2

Polariton Lasing and Polariton Condensates

2.1 Bose-Einstein condensates

Bosonic condensation, the build up of a macroscopic occupation in the ground state of a system of Bosons, is a direct consequence of the indistinguishability principle of quantum mechanics that dictates the underlying statistics of elementary particles. Depending on their spin, particles are divided in two groups with radically different statistical behaviour [48]. For ensembles of classical particles the population density distribution among the continuum of available energy states N(E), is known to follow the Maxwell-Boltzmann distribution. However, in systems where quantum mechanical effects play an important role, depending on whether particles obey Pauli's exclusion principle or not, gives rise to two distinct statistical distributions. Fermions have been shown to obey the Fermi-Dirac distribution while Bosons are described by the Bose-Einstein distribution.

$$N(E) = \frac{g_E}{e^{\frac{E-\mu}{k_B T}} + \epsilon} \tag{2.1}$$

Equation 2.1 for $\epsilon = 1$ gives the Fermi-Dirac, for $\epsilon = 0$ the Maxwell-Boltzmann and for $\epsilon = -1$ the Bose-Einstein distribution, where k_B is the Boltzmann constant, T the temperature of the ensemble of particles, μ the chemical potential and g_E the degeneracy of the state with energy E for boson statistics and is equal to one in the rest of the cases. The population density according to each of these statistical behaviours is graphically depicted in fig. 2.1 for two different temperatures.

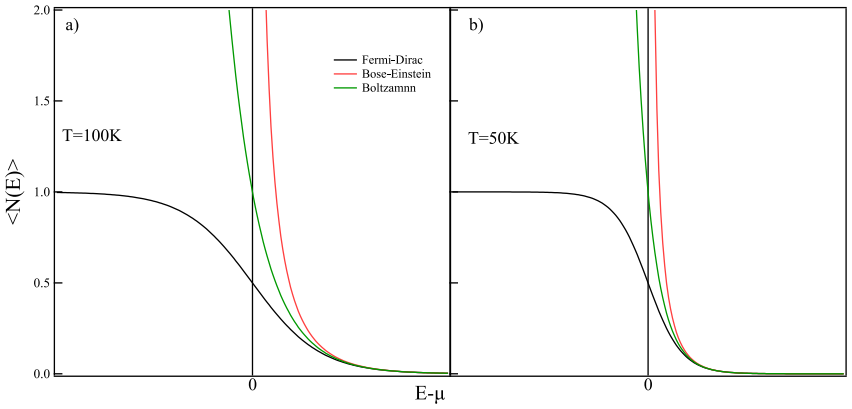

FIGURE 2.1: Fermi-Dirac, Bose-Einstein and Boltzmann distributions for T=100K **a)** and T=50K **b)**

Since the distribution of bosons among the available energy states follows the Bose-Einstein distribution (eq. 2.1 for $\epsilon = -1$), reducing the temperature of a system of Bosons below a critical temperature T_c, eventually leads to a saturation of the excited states and the emergence of a macroscopic occupation (N_0 comparable to N) of the ground state. For a Bose Gas in a three dimensional volume the critical temperature (T_c) for this transition is given by:

$$T_c = 3.31 \frac{\hbar^2 n^{2/3}}{k_B m} \tag{2.2}$$

where n is the particle density and m the particle mass.

Alternatively one can arrive at the BEC phase transition by comparing the thermal de Broglie wavelength of the particles (λ_T) to the mean distance between them. For high temperatures the mean spacing (d) is considerably greater than λ_T and the systems is in the classical regime.

$$\lambda_T = \left(\frac{2\pi\hbar^2}{k_B m T} \right)^{\frac{1}{2}} \tag{2.3}$$

When λ_T becomes comparable to the inter-particle spacing a degenerate gas forms and the bosonic nature of the particles becomes important [49]. This can be achieved either by increasing the density of atoms or by reducing the temperature of the system. For alkali atoms the characteristic temperatures for the BEC phase transition is sub-μK for densities of the order of $10^{13} - 10^{15}$ per cm^{-3}.

More than 80 years past their initial theoretical formulation, in the works of Bose on photon statistics [15] and the expansion of his work by Einstein to a gas of non-interacting massive bosons [16], Bose-Einstein condensates were first realised in vapours of Rubidium [17], sodium [18] and lithium [50] in 1995 and have since been demonstrated in an extensive range of atomic systems (^{1}H, ^{7}Li, ^{23}Na, ^{39,41}K, ^{52}Cr, ^{85,87}Rb, ^{133}Cs, ^{170,174}Yb ,^{4}He*) [49]. Condensation in these atomic systems was

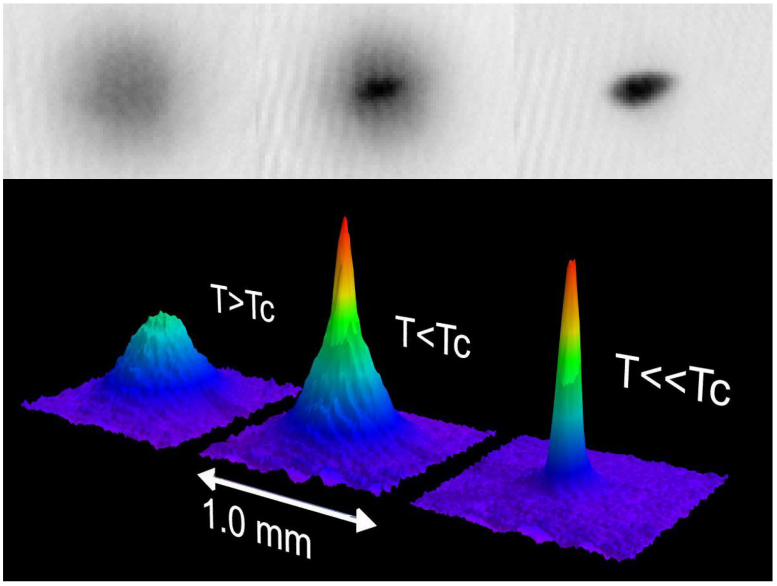

FIGURE 2.2: Observation of the BEC phase transition in an ensemble of approximately 700000 sodium atoms with $T_c = 2\mu K$ [18]. The top panel corresponds to images of absorption imaging vs two spatial dimensions while the bottom panel is a three dimensional rendering of the corresponding images. For $T > T_c$ atoms are thermally distributed, for T just below T_c a sharp increase in the density is observed in the centre of the atomic cloud. For further reduction in the temperature below T_c almost all of the atoms are in the condensed phase

achieved by reducing the kinetic energy and freezing the intrinsic excitations of the system down to the order of micro-Kelvin typically with the use of Magneto-optical traps (MOT).

2.2 Condensation in reduced dimensionality systems

As polaritons are effectively a two-dimensional system, it is meaningful to examine the validity of the BEC phase transition for reduced dimensionality systems. For a uniform bosonic gas where particle eigenstates are characterised by their momentum **k**, in thermodynamic equilibrium the total number of particles in the system and the critical concentration N_0 is given by:

$$N(T,\mu) = \frac{1}{(2\pi)^d} \int N(E(k),T,\mu)_B d^d k \tag{2.4}$$

$$N_0(T) = \lim_{\mu \to 0} N(T,\mu) \tag{2.5}$$

where d is the system dimensionality and $N(E(K), T, \mu)$ the Bose-Einstein distribution. The integral in eq. 2.4 diverges for d=2 for a finite temperature and therefore a non-interacting Bose gas cannot condense in an infinite 2d system [51, 52] while this can also be extended for an interacting Bose gas as well. Similarly it was shown early on (1966) that long range order (see section 2.3.3) cannot appear in 2D systems [53]. Nevertheless, in the theoretical works of Kosterlitz and Thoules, it was predicted that a superfluid phase transition can spontaneously occur in weakly interacting bosonic systems with two dimensions [54].

The above formalism applies to the case of a homogeneous Bose gas, however this drastically changes in the presence of a trapping potential as this significantly changes the energy dependence of the density of states which for 2D is constant (DOS(ϵ)$\propto \epsilon^{d/2-1}$). It can thus be shown that a BEC phase transition can indeed occur in a 2D Bose gas inside a confining potential. For the simple case of a symmetric harmonic potential ($V(x, y) = m\omega^2(x^2 + y^2)$) for instance, the critical temperature T_c^{2d} is:

$$T_c^{2d} = \sqrt{\frac{6N}{\pi^2}}\hbar\omega \tag{2.6}$$

with N being the total number of particles [52]. Effectively the trapping strength can define the critical temperature for the BEC phase transition as well as the density required to reach this.

2.3 From atomic to solid state condensates

The experimental observation of Bose Einstein condensation in dilute atomic gases, renewed scientific interest in the possibility of solid state condensates, leading to the experimental demonstration of condensation of magnons in $TlCuCl_3$ in 1999 [55]. This discovery was followed by the observation of a Bosonic condensation of excitons in a system with two parallel layers of conduction band electrons [56]. The bosonic condensation of polaritons in semiconductor microcavities was unambiguously demonstrated in 2006 in the landmark work of Kasprzak *et al* [20], In quantum well structures the spontaneous emergence of coherence in a cold gas of indirect excitons was reported in 2012 [57] in a coupled quantum well structure (CQW). In 2014 evidence of a "gray" condensate of dipolar excitons in a single quantum well structure was presented [58], were dark excitons were shown to be coherently coupled to bright excitons. More surprisingly, in 2010 a group from Bonn University reported on the thermalisation and subsequent Bose-condensation of an ensemble of photons confined in a microcavity [59].

2.3.1 Condensation of excitons

As mentioned previously (section 1.3) excitons have integer spin and can thus be considered as composite bosons. However, this statement is true in the diluted limit. At high densities the inter-particle interactions tend to dissociate excitons into their individual components due to the small binding energy. Moreover with increasing density the electron and hole fermionic phase space occupation becomes significant leading to phase space filling and the build up of exchange energy between the excitonic components [60]. This leads to the degeneration of the bosonic nature of excitons that can be expressed in the commutation of the excitonic creation and annihilation operators (for QW excitons).

$$\left[b_k, b_k^\dagger\right] \simeq 1 - \mathcal{O}(na_{Bexc}^2) \tag{2.7}$$

Thus excitons can be considered as robust bosons only in the limit of $na_{Bexc}^2 \ll 1$ [61], while the saturation density above which excitons cannot be considered as bosons is given by [60]:

$$n_{sat} = \frac{0.117}{na_{Bexc}^2} \tag{2.8}$$

As the exciton Bohr radius in QWs is inversely proportional to the exciton binding energy (eq. 1.12), excitons in large band gap materials are preferable due to higher saturation densities. For GaAs quantum wells the saturation density is $n_{sat}^{GaAs} \simeq 5 \times 10^{10} cm^{-2}$. Furthermore, for increasing density, screening of the attractive coulomb interaction from other carriers reduces the exciton binding energy. The net impact of the described effects is that at high densities the excitonic components start to dissociate through the reduction of their binding energy while the oscillator strength of the optical transition diminishes and the bosonic nature effectively collapses.

Despite these difficulties the very low effective mass of excitons has made them an attractive system for the realisation of Bose Einstein condensates at cryogenic temperatures. Early experiments indeed reported evidence of a Bose phase transition in an ensemble of bright excitons in Cu_2O system [62]. A different approach is to use excitons formed from electrons and holes from different quantum wells to observe Bose condensation. In these systems the indirect excitonic state has increased radiative lifetime enabling the system to reach a semblance of thermodynamic equilibrium [63]. Recently the build up of spatial coherence (or ODLRO) was demonstrated in such a system when cooled below a critical temperature of 1K [57]. Interestingly, strong coupling of indirect excitons to a semiconductor cavity mode has also been recently reported [64].

2.3.2 Polariton condensates

As has been described previously (section 1.2.1), microcavity exciton-polaritons are composite bosonic particles. Their in-plane mass is thus, the reduced mass of their in-plane excitonic and photonic counterparts, weighed by the Hopfield coefficients with values typically around $10^{-5}m_e$ that can be readily measured experimentally from the polariton dispersion. It follows from eq. 2.2 that the critical temperature for condensation will be significantly greater with respect to atomic systems. Moreover in bosonic systems it has been shown that the scattering rate into an energy state is strongly dependent on the occupation number N of that state and proportional to (N+1). This phenomenon, known as final state bosonic stimulation [65], was proposed in 1996 as the dominant mechanism for the emergence of coherence in a semiconductor microcavity in the strong coupling regime, greatly out of equilibrium [12]. Indeed, initial experiments by non-resonant pulsed excitation in a CdTe microcavity sample showed an unambiguous stimulation of the lower polariton state [66]. The bosonic nature of exciton-polaritons lies at the heart of this inversion-less lasing mechanism and it stimulated efforts to experimentally confirm the bosonic nature of polaritons. Bosonic final state stimulation was demonstrated in a pump probe experiment in 2002 by Savvidis and co-workers who used a weak probe beam resonant with the lower polariton ground state to trigger stimulated scattering [13], demonstrating a parametric amplification of the lower polariton emission [67]. In this process, energy and momentum of the signal and idler states must of course be conserved and this leads to a very specific resonance condition for the angle of the pump, which has been named the "magic angle". However parametric processes have since been shown to also occur spontaneously similarly to an optical parametric oscillator [68, 69]. These results were quickly followed by demonstration of polariton condensation under non-resonant excitation in a GaAs based structure 2002 [70]. In 2005 Richard et al reported non-equilibrium condensation in momentum space [71], and a year later the first report of a non-equilibrium Bose-Einstein condensate was demonstrated under pulsed excitation conditions [72]. One year later in the pioneering article by Kasprzak et al, sufficient evidence of a polariton Bose-Einstein condensate was presented [20]. In this report, the authors clearly demonstrated that condensed polaritons followed the Bose distribution with a temperature close to that of the lattice and more importantly reported on the build-up of long range order which is considered the smoking gun of the Bose phase transition. A year later a polariton BEC was also reported in a stress induced trap [73]. These observations paved the way for exploring the rich condensate physics that was previously studied in atomic condensates and stimulated experimental research in the field of polaritons.

2.3.2.1 Experimental features of polariton condensates

Increased experimental flexibility of semiconductor microcavities, relatively to cold atomic gases, allows for the direct observation of a number of characteristics expected at the polariton Bose phase transition. Manifestations of polariton condensation have demonstrated that the appearance of this intriguing state of matter is accompanied by a non-linear increase in the emission termed polariton lasing [21], long-range spatial coherence [74, 75] and stochastic vector polarisation [76]. However, the most compelling argument demonstrating this phase transition still remains the observation of a population density following the Bose-Einstein energy distribution [20].

2.3.3 Off-diagonal Long range Order

Penrose and Onsager determined that as long as the thermal de Broglie wavelength is considerably smaller than the system size, bosonic condensation should be evident by the appearance of Off Diagonal Long Range Order or ODLRO [77]. ODLRO is a characteristic quantum mechanical property of a system of interacting bosonic (or pairs of fermionic) particles. It arises from the off-diagonal elements of the density matrix that have no classical analogue and its physical meaning is that the memory of the quantum phase is preserved over macroscopic distances [78]. The BEC transition can be experimentally demonstrated by the spontaneous appearance of Off Diagonal Long Range [61] as the coherence properties of the system are critically affected by the macroscopic occupation of a quantum state. The appearance of off-diagonal order in a system manifests itself in the form of first order spatial coherence ($g^{(1)}$) that can be determined by means of interferometric measurements

$$g^{(1)}(r_1,t_1;r_2,t_2)=\frac{E^*(r_1,t_1)E^(r_2,t_2)}{\sqrt{\left\langle\left|E^(r_1,t_1)\right|^2\right\rangle\left\langle\left|E^(r_2,t_2)\right|^2\right\rangle}} \tag{2.9}$$

$g^{(1)}(r_1,t_1;r_2,t_2)$ is a measure of the coherence of an electromagnetic field and is equal to the normalised spatial auto-correlation of the field and its values range from 1 for a fully coherent field to 0 for a fully incoherent radiation.

2.3.4 Theoretical description of Polariton condensates

An effective tool for the theoretical description of Bose Einstein condensates has been the Gross-Pitaevski equation (GPE) [79]. However, as polariton condensates exist in a dynamic equilibrium of constant dissipation and optical pumping, this has to be reflected in the theoretical description as well. Taking this into account,

Wouters and Carusotto introduced in 2007 a Generalised Gross Gross-Pitaevski equation with a mean field description of the interactions between particles to describe the macroscopic wavefunction $\psi(r)$ of this non-equilibrium condensate [80]:

$$i\frac{d}{dt}\psi(r) = \left[-\frac{\hbar\nabla^2}{2m_{lp}} + \frac{i}{2}\left[R(n_r) - \gamma\right] + g\left|\psi\right|^2 + 2\tilde{g}n_R\right]\psi(r) \tag{2.10}$$

In eq. 2.10 γ is a momentum-independent loss rate that describes polaritons escaping the system prior to condensation while R is the amplification rate due to stimulated scattering from a non thermal reservoir. Interactions between the reservoir and the condensed particles are represented with the interaction term $2\tilde{g}n_R\psi(r)$ while the term $g\left|\psi\right|^2$ describes particle interactions within the condensed state. The evolution of the condensate therefore is strongly affected by the reservoir dynamics of the system which can be described phenomenologically by:

$$\frac{d}{dt}n_R(r) = P - \gamma_R n_R(r) - R(n_R(r))\left|\psi(r)\right|^2 + D\nabla^2 n_R(r) \tag{2.11}$$

where $n_R(r)$ is the reservoir density, P is a pumping rate and D the diffusion of particles populating the reservoir. In this description the threshold corresponds to the value of the reservoir density where amplification and losses are perfectly balanced while above threshold the condensate density increases as $||\psi||^2 = (P - P_{th})/\gamma$. This is an intuitive result eloquently demonstrating that in structures with high Q-factors (and polariton decay γ) condensation is much easier to achieve. This straightforward approach has been able to reproduce a wide range of observed effects in polariton condensate systems ([81]).

2.4 Coherent polariton phenomena

The manifestation of polariton condensation is associated with a number of highly interesting physical phenomena that can be readily measured and investigated. The build up of a macroscopic polariton population is clearly discernible experimentally by a non-linear increase in the emission of microcavities and a narrowing of the linewidth of emission characteristic of the emergence of temporal coherence in the system. Furthermore the condensate phase transition is demonstrated with the build up of long range spatial coherence [20]. Above the non-linear threshold polariton condensates have been extensively investigated in order to explore the rich condensate physics that were initially predicted for atomic condensates, such as superfluidity vorticity, soliton nucleation and phase locking.

2.4.1 Superfluidity and vorticity

The relation between condensation and superfluidity is "subtle" since a Bose condensed system does not necessarily exhibit superfluid behaviour, while superfluidity may also arise in non-condensed systems of lower dimensionality [49]. Nevertheless, frictionless flow of a quantum liquid, first observed in liquid helium in 1938 [82], is one of the most astounding phenomena of degenerate boson gases. Following the observation of polariton Bose condensation, a number of experiments have focused on the fluidic nature of polariton condensates and a wide range of effects, expected to occur in the superfluid regime such as suppression of Rayleigh scattering and collective dynamic behaviour, have been documented [83, 84]. Furthermore the “smoking gun” of superfluidity, the linear Bogoliubov excitation spectrum has also been reported under pulsed non-resonant excitation [85, 86] as well as in resonant four wave mixing experiments [87, 88]. Nevertheless, the linearisation of the polaritonic dispersion presented in references [85, 86] has been recorded with a time-integrated spectroscopy system although the system was excited with ultra-fast pulses. This approach can give rise to artifacts, as the recorded images are averaged well over the lifetime of the particles and thus different density regimes are mixed in the measurements. Interestingly, a linearisation of the momentum distribution has not been reported in the dynamic equilibrium regime (with continuous wave excitation) or in the transient domain with pulsed excitation and this will be investigated in chapter chapter 7 of this thesis.

Depending on the inhomogeneity of the potential landscape they populate, coherent quantum fluids are also expected to exhibit a wide variety of topological defects. This allows for solutions to eq. 2.10 with an altered density profile for the condensate, revealing vortex states [89]. Indeed the emergence and propagation of vortices in superfluid helium is a well documented effect [90] and polariton fluids also display a variety of phase dislocations that have received great interest in recent years, such as quantised vortex states [91] as well as spin polarised vorticity [92] and vortices due to polariton turbulent flow [93]. Furthermore it has been demonstrated how quantised vortices can be imprinted onto a polariton quantum fluid by modulating the angular momentum carried by a quasi-resonant pump [94, 95].

2.4.2 Solitons in polariton condensates

Apart from the formation of quantised interacting vortices, the non-linear properties of BECs can give rise to spatial solitons, the latter resulting from the cancellation of the dispersion by polariton-polariton interactions. Solitons are solitary waves that preserve their shape while propagating through a dispersive medium [96, 97] due to the compensation of the broadening by the non-linearity of the medium [98].

Spatial solitons have so far been observed by employing a variety of non-linearities ranging from Kerr non-linear media [99] to photo-refractive [100] and quadratic [101] materials. Apart from their potential application in optical communications [102, 103], solitons are important features of interacting Bose-Einstein condensates (BECs) and superfluids.

In polariton condensates, the source of the non-linearity, essential for the formation of such solitary waves, has been identified in the non-linear polariton-polariton interaction. A type of solitary wave-packets demonstrated in strongly coupled microcavities are the so-called bright solitons [104, 105]. The authors of these studies experimentally demonstrated the non-dispersivity of a propagating coherent polariton ensemble by measuring the evolution of the full-width at half maximum (FWHM) of the wave-packet as it propagated in the sample.

Another special type of solitons are the so-called dark solitons, which feature a density node accompanied by a π phase jump. Since their theoretical prediction in the context of Bose-Einstein condensates (BECs) [106], dark solitons were studied and observed in the field of non-linear optics [107] and then in cold-atom BECs [108]. Experimental observation of BEC of exciton-polaritons, sparked intense interest in the quantum-hydrodynamic properties of polariton fluids culminating also in the report of nucleation of oblique dark solitary wave-packets in the wake of an obstacle in a number of publications [109–111]. In these works, the observation of dark notches in the intensity profiles together with a π shift in the phase have been used as the fingerprints for dark solitons in microcavities. In addition, oblique half-dark solitons have been demonstrated, which carry a non-zero degree of circular polarisation in the presence of the TE-TM splitting of the cavity mode that acts as an effective in-plane magnetic field [112].

2.4.2.1 Observation of oblique dark notches in an photonic cavity

These fingerprint features, however, can also be observed without the presence of non-linearities, which is the fundamental ingredient differentiating solitons from linear wave propagation. Below, we investigate the propagation of uncoupled cavity photons at low densities, excluding a relevant influence of polariton non-linearities and show that propagation in this linear regime across an extended defect can create deep notches in the intensity profile accompanied by a π phase shift.

Bare cavity sample

The investigated sample is a bulk λ GaAs microcavity surrounded by 24 (top) and 27 (bottom) GaAs/AlAs distributed Bragg reflector pairs and held in a cold-finger

cryostat at a temperature of 15 K. It was illuminated by an ultra-narrow linewidth single-mode continuous wave Ti:Saph laser, tuned to the resonance of the cavity around $1.485\,\mathrm{eV}$. The experiments were performed in a transmission configuration with both a Gaussian and half-Gaussian excitation beam and the phase was measured using a Mach-Zehnder interferometer (fig. 2.3). The experiments were performed in the linear regime, facilitated by the large negative detuning of $-29\,\mathrm{meV}$ of the cavity photon mode from the GaAs bulk exciton resonance at 1.514 eV. To verify that we are indeed in the linear regime, we studied the excitation density dependence of our results and found that they are independent of both the shape of the laser beam and the excitation density over a range of four orders of magnitude. Indeed the reported features persist at densities as low as $2.3 \times 10^2\,\mathrm{cm}^{-2}$, seven orders of magnitude lower than the lasing threshold observed in standard microcavities [113].

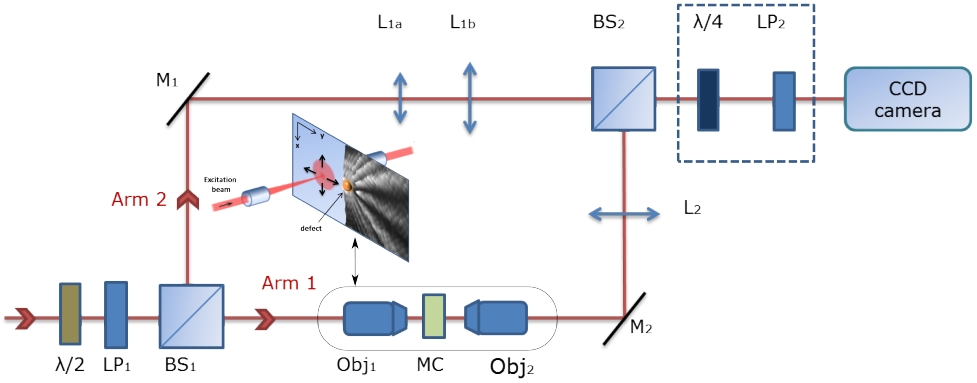

FIGURE 2.3: Experimental setup of the Mach-Zehnder interferometer. BS_1 and BS_2 are non-polarizing beam splitters, M_1 and M_2 are mirrors, Obj_1 is the excitation objective with a 20x magnification and 0.4 NA, Obj_2 is an objective for collection of the transmitted beam, with 10x magnification and 0.25 NA, L_{1a}, L_{1b} and L_2 are convex lenses, $\lambda/2$ and LP_1 are respectively a half-wave plate and linear polariser for controlling the excitation power, while $\lambda/4$ and LP_2 are respectively a quarter-wave plate and a linear polariser for measuring the circular Stokes components introduced only for polarisation resolved measurements. The inset in the centre displays the excitation relevant to the observed features

Oblique dark notches in the linear regime

The real space intensity and interference pattern of a photonic wave propagating across a defect are shown in Fig. 2.4. The experimental results distinctly show the presence of two dark notches in the intensity pattern along with a π phase shift visible in Fig. 2.4(b) as paths of vortices merging in succession with alternating topological charge ± 1. The observed patterns are modelled using simple linear electromagnetic wave propagation, substantiating that these features are not indicative solely of oblique dark solitons in coherent polariton fluids, but also of

interference patterns created by scattering of photons from a defect state. Simulations of the measurements using the realistic experimental parameters are shown in Fig. 2.4(c) and Fig. 2.4(d) where again we notice the distinct appearance of dark notches in the intensity profile accompanied by a π phase shift in the simulated phase map.

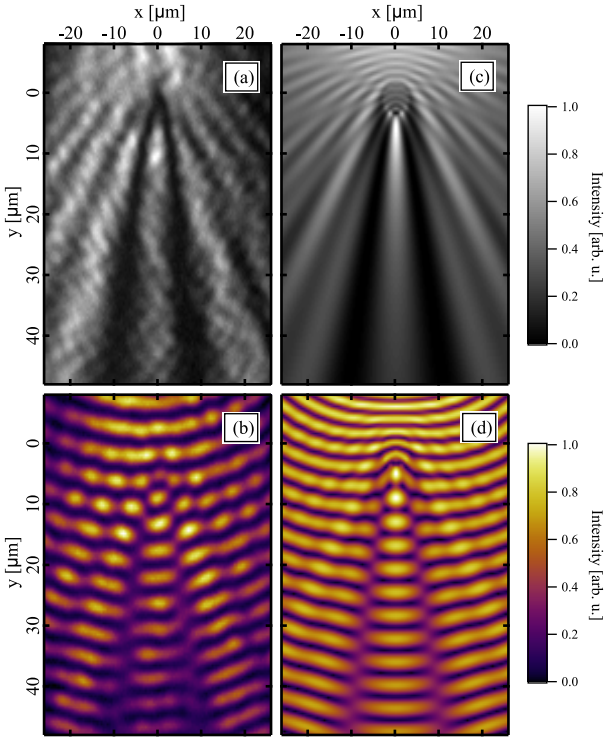

FIGURE 2.4: Experimental (a),(b) and simulated (c),(d) real space intensity and interference patterns showing the two soliton "fingerprints" generated by the scattering of a beam with a point-like defect: a dark notch in the intensity pattern together with π phase dislocations. In the images the polaritons propagating downwards, along the y-axis, are injected with a wave-vector of $1.5\ \mu m^{-1}$ and are scattered by a defect positioned $25\ \mu m$ away from the excitation spots.

In the microcavity polariton literature, the observation of dark-solitons has been claimed using both a Gaussian excitation beam [109, 111] and half-Gaussian excitation beam [109, 112]. To verify that the observed features are indeed not dependent on the density or the geometry of the propagating wave, we performed a series of power dependence measurements with both Gaussian and half-Gaussian excitation beams. In Fig. 2.5 we show the data acquired with a half-Gaussian excitation beam, focused to a spot with FWHM of $3.5\ \mu$m (see Fig. 2.5 e), $90\ \mu$m away from the defect. Here we vary the excitation power by 5 orders of magnitude, from 20 mW (Fig. 2.5 a,b) to 400 nW (Fig. 2.5 c,d) and do not observe any significant changes in the spatial features. The two notches in intensity along with phase vortex lines in the interferograms persist as they arise from the scattering and interference. This is confirmed by the intensity profile and by the FWHM calculated for the left dark-notch in Fig. 2.8f) which is $4.2\ \pm\ 0.5$ at $20\ mW$ and $3.7\ \pm\ 1$ at $400\ nW$. The

half-Gaussian beam was created by a confocal excitation scheme similarly to what is described in the supplementary information in the study of Amo *et al.* [109]. In this scheme, a razor blade is placed between two lenses (at a distance equal to the focal lengths of the lenses) before the excitation objective (Obj_1 in Fig. 2.3). The first lens focuses the laser on a razor blade while the second collimates the image. In this way, by adjusting the position of the razor blade it is possible to shape the excitation beam with a half-Gaussian profile. Observing the same features with both excitation shapes corroborates that our observations arise due to interference effects introduced by the defect.

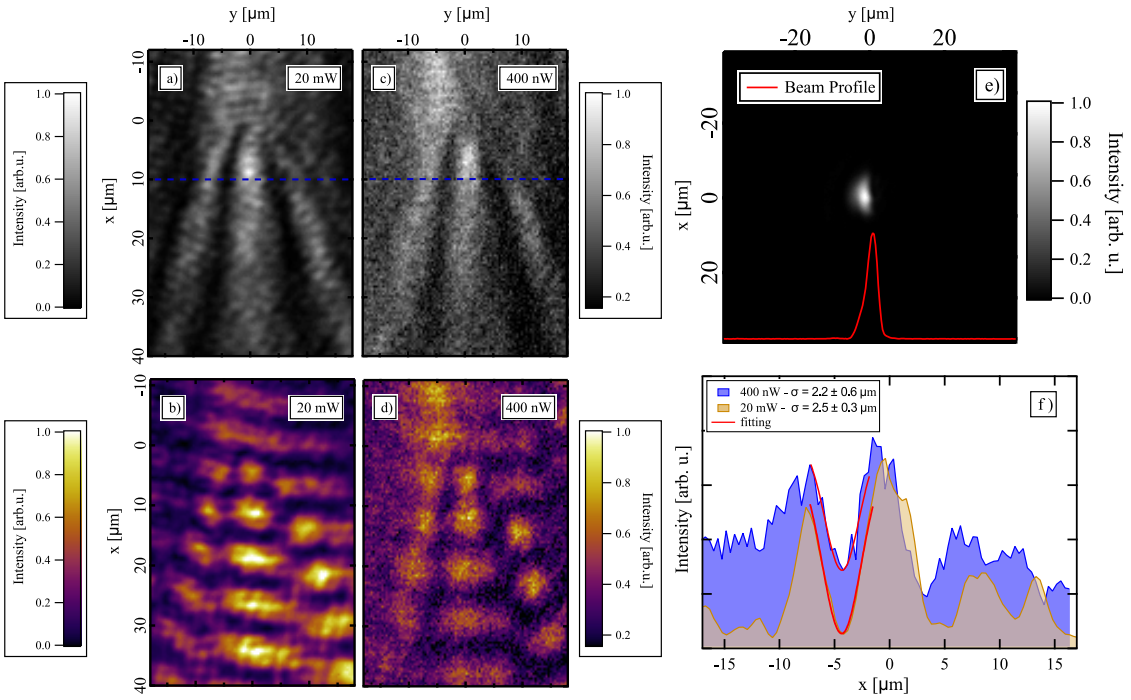

FIGURE 2.5: Experimental real space intensity (a), (c) and interference patterns (b), (d) acquired at 20 mW and 400 nW excitation power. Fig. (c) and (d) have been plotted with an offset of 0.16 (i.e. saturated at low intensities) for the purpose of the illustration. (e) Half-Gaussian excitation spot. (f) Intensity profiles calculated along the dashed blue lines in a) and c), 10 μm away from the defect. The red line represents the inverse Gaussian fitting used to calculate the FWHM of the left dark-notches in Fig. a) and c). The σ of the two fitting used for the calculation of the FWHM $2\sqrt{ln(2)}\sigma$ are also reported in the legend. The 400 nW profile (blue) reported in Fig. e) has been shifted on the left by about 1 μm respect to his original position for clarity purposes.

Solitons are predicted to appear in polariton microcavities as the result of the non-linearity arising from the polariton-polariton interactions [114]. Since our experiments are conducted in an uncoupled microcavity system, it is important to understand how the nature and size of the defect affects the formation process of these soliton-like features. In a study of the structural and optical properties of GaAs/AlAs microcavities grown by molecular beam epitaxy it was shown that the most common point-like defects (PD) were characterised by a circular or elliptical shape [115], formed due to Gallium droplets emitted occasionally during the growth

process [116, 117]. The presence of the defect effectively modifies the effective thickness of the cavity layer, which typically results in an attractive potential for the cavity mode [115]. Consequently, the wave-vector of the photonic mode in this region is higher than in the rest of the cavity. Scattering by a defect state, therefore will depend on the wave-vector mismatch between the photonic mode outside and inside the defect at the energy of the propagating mode fig. 2.6. When the energy shift of the defect photon mode with respect to the unperturbed cavity mode is large enough to make the coupling between them inefficient, the defect behaves like a hard scatterer and the spatial intensity distribution is similar to the complementary case of a single-slit diffraction. However, when there is a finite transmission through the defect it will produce dark and bright traces with a more complicated phase pattern. As it has been shown by Berry *et al.* [118, 119], wave-fronts resulting from interference can indeed contain dislocation lines. In the case of a scattered beam, dislocations are composed of phase shifts at positions where the amplitude of the electromagnetic wave and thus the intensity vanishes, representing nodes of the wave. It is worth mentioning that non-linearities are negligible close to nodes also in the non-linear regime (as the density vanishes), and phase dislocations at zero intensity (i.e. dark notches) are features of both linear [120, 121] and non-linear waves.

Beyond the qualitative discussion above, simulations of the experiments were performed, based on numerical solutions of the linear scattering problem using the classical theory of electromagnetism. The model, simulates the propagation of quasi two-dimensional photons with a parabolic dispersion in a cavity with a fixed width. The incident wave has been treated as coming from a linearly polarised point-like source with polarisation in the plane of the cavity. Defects have been modelled as disk-shaped perturbations of the cavity thickness resulting in an energy shift of the photon dispersion. To model the defect parameters, which are not experimentally known, a disk shape with a radius of $3\ \mu\mathrm{m}$ and a potential of -2.3 meV was used (in agreement with Zajac et al. [115]). Maxwell's equations are then solved using expansion of the fields into the planar cavity eigenmodes in cylindrical coordinates fulfilling the boundary conditions for tangent component of electric and magnetic field on the interface between the cavity and the defect. This linear model reproduces the intensity notch and the phase dislocation previously identified as dark-soliton "fingerprints". In particular, the phase jump visible in the interference pattern depends on the direction of the incoming polariton wave relative to the defect, while the size of the defect relative to the wavelength of the propagating wave affects the formation of higher-order phase dislocations.

Coherent polariton fluids have been predicted to flow almost unperturbed around the defect or experience turbulent flow resulting in the nucleation of vortices and/or solitons beyond the position of the defect, depending on the excitation density or on

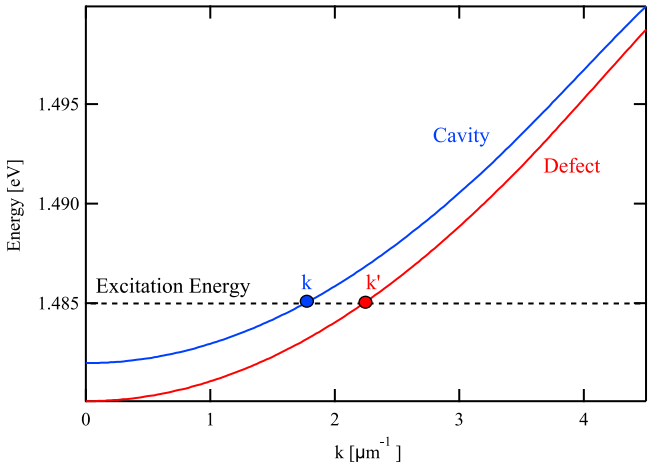

FIGURE 2.6: Cavity and defect state dispersion showing the wave-vector mismatch for a given energy

the energy of the pump [114]. We evaluated the possibility of observing these features, associated in the literature to dark-solitons within a coherent polariton fluid, in the absence of non-linearities. Figures 2.5a,b show the phase and the intensity of soliton-like "fingerprints" in real space. Instead of increasing the excitation power, we fine-tune the energy of the excitation beam, and observe the appearance and disappearance of the soliton-like features. As discussed previously, the appearance of the intensity minima and phase dislocations is a result of interference which is sensitive to the intensity and relative phase of contributing waves. The increase of the energy of the excitation beam by 2 meV causes an increase of the in-plane wave-vector of the propagating mode that, in turn, changes the interference condition so that the oblique dark notches (fig. 2.7(c)) and the phase dislocations (Fig. 2.5d) vanish. The wave-vector dependence of such transitions will depend on the defect structure and the related bound states [115], so that they could be observed also with decreasing wave-vector for other defect types. Intensity profiles measured at a fixed distance from the defect (fig. 2.5e,f) confirm the observed transition. This corroborates that the appearance/disappearance of soliton-like features strongly depends on the wave-vector of the propagating mode. It is worth noting that an increase of the polariton density corresponds to an energy blue-shift of the polariton dispersion. For polaritons excited resonantly with a given energy, this results in an increase of the polariton wave-vector with decreasing density along the polariton propagation. Specifically in non-resonantly excitation experiments, this blue-shift depends on the exciton density in the reservoir.

In a similar experiment, the appearance of oblique half-solitons was addressed, with polarisation-resolved measurements. The intensity images (fig. 2.8a,b) are measured using an excitation linearly polarised parallel to the y-direction. The interference patterns (Fig. 2.8c,d), are obtained by selecting the same polarisation for the excitation and reference beam. The signature of an oblique dark half-soliton

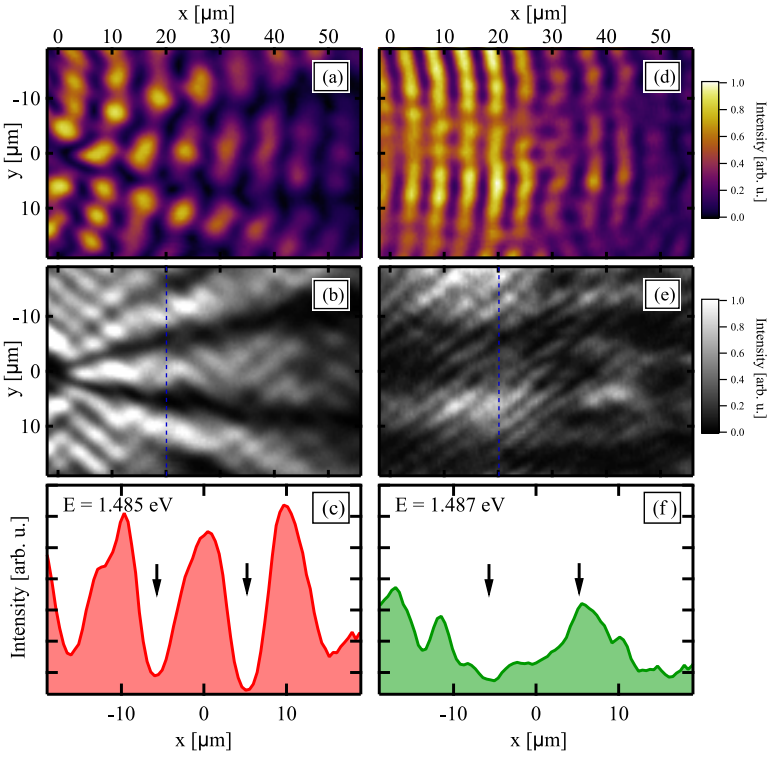

FIGURE 2.7: Experimental interference (a),(c) and intensity (b),(d) showing the transition between the regime where the solitonic features are well defined ($1.485\,\mathrm{eV}$) to a regime where they vanish ($1.487\,\mathrm{eV}$). The intensity profiles (e),(f) calculated along the blue dashed line, 20μm away from the defect, confirm that the dark notches disappear when the energy of the excitation beam is increased. The two arrows indicate the positions of soliton-like fingerprints.

is a notch in only one circular polarisation component [112, 122]. We excite the sample with a linearly polarised beam and detect the two circular polarisation components (σ_+, σ_-) separately. The intensity profile and the interferogram for theσ_+ and σ_- component are given in fig. 2.8(a) and fig. 2.8(c) respectively. The images show the presence of a σ_- "soliton", indicated by the blue arrows, that is absent in the σ_+ component (Fig. 2.8b,d). The same applies to the σ_+ counterpart, where a half-soliton "fingerprint" is observed only on the right side of the image.

By calculating the degree of circular polarisation, given by $S_c = (I_{\sigma_+} - I_{\sigma_-})/(I_{\sigma_+} + I_{\sigma_-})$, with I_{σ_+} and I_{σ_-} being the measured intensities of the two components, we measure the pseudospin state inside the cavity (Fig. 2.9(a). By comparing the position where the solitonic features have been observed (Fig. 2.8), indicated by the black dotted lines in Fig. 2.9(a), we note the presence of a pair of oblique traces with cross-circular polarisation, resembling the predictions and observations attributed to a polariton superfluid [112, 122]. The high degree of circular polarisation that we observe is due to the polarisation splitting of transverse electric and transverse magnetic optical modes (TE-TM splitting) [123]. The latter gives rise to the optical spin Hall effect [124] that has been observed in both polariton [125] and purely photonic microcavities [126]. Simulations of a linearly polarised incoming beam

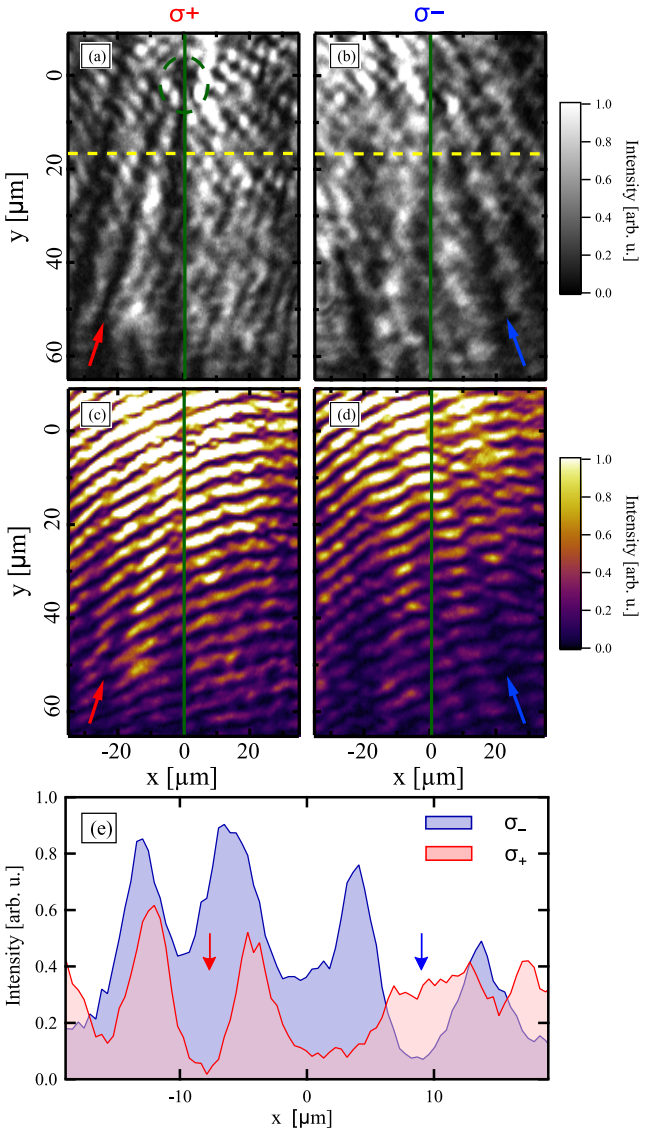

FIGURE 2.8: Experimental intensity pattern (a-b) and real space interference (c-d) showing two half-soliton features as indicated by the arrows. The red and blue arrows indicate respectively the position of the σ_+ and σ_- half-soliton features: a dark-notch with an associated phase jump present in only one circular component. The green vertical line is a graphical guide to distinguish the two different regions while the dashed circle in (a) indicates the defect. (e) The intensity profiles from the yellow dotted line displaying the two dark notches present respectively in only one of the opposite polarisation basis, as indicated by the arrows.

propagating along the y-direction and scattered by a defect, induces the formation of two cross-polarised traces propagating in oblique directions (Fig. 2.9(b)). The detected field is a superposition of the incoming linearly polarised wave and the scattered wave. The TE-TM splitting of the optical mode in a photonic cavity is responsible for an anisotropy in the polarisation flux, as previously shown on the same sample by Maragkou et al. [126] and the same values of the TE-TM splitting have been used to perform the simulations. The polaritons scatter from the defect with wave-vectors of equal modulus but in different directions both in the real

and momentum space. Because of the birefringence induced by the TE-TM splitting, polaritons propagating in different directions experience different polarisation rotation. Photons travelling to the right gain a σ_- component while photons propagating to the left gain a σ_+ component. The anisotropy of the effect manifests itself in the intensity pattern, where it is possible to observe the features of an oblique soliton in one circular component and not in the other.

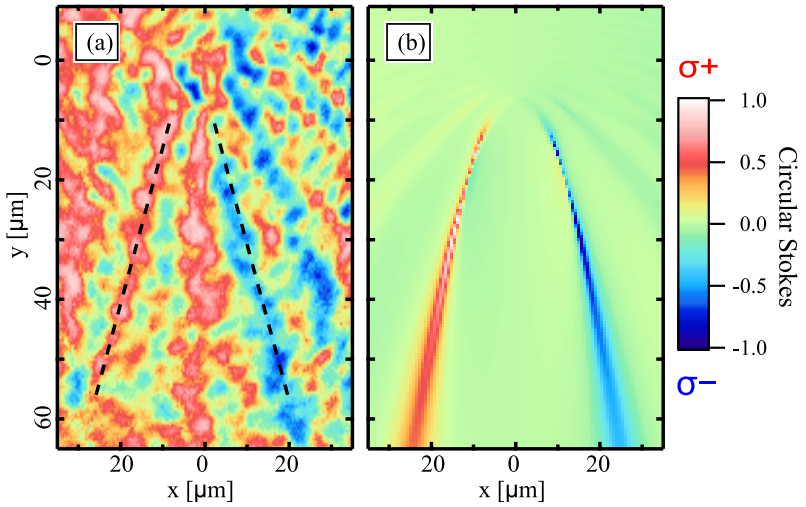

FIGURE 2.9: Experimental (a) and simulated (b) circular Stokes parameter showing half-soliton features. The two black dotted lines correspond to the position of the dark notches present in Fig. 2.8(a) and (b).

Discussion

These results clarify that phase vortex lines in polariton propagation together with dark notches of constant relative depth in the intensity patterns, used as fingerprints of oblique-dark solitons and half-solitons in the literature, are also present in the linear propagation regime. Consequently, these features are necessary but not sufficient evidence to identify solitons. As demonstrated, these features are the result of self-interference of the incoming wave scattered by a defect. We therefore believe a more reliable criterion for identifying dark-solitons, based on the definition of solitons (i.e. solitary non-spreading wave), would be the size of the observed features (dark soliton width) which in turn is determined by the healing length of the condensate which is density dependent ($\xi = \sqrt{\frac{\hbar^2}{2m_p n U_0}}$ where nU_0 is the interaction energy term) as has been used in the case of dark solitons in atomic BECs [108]. In the case of half-solitons it is shown that the intrinsic TE-TM splitting of the cavity dispersion gives rise to cross-polarised oblique traces without the introduction of any non-linearity in the medium. Moreover the appearance/disappearance of these features for different in-plane kinetic energies is reproduced in the linear regime. Interestingly, although there have been experimental demonstrations of

dark solitons in atomic systems [108], *oblique* dark solitons as such, to the best of the author's knowledge, have not been experimentally reported in atomic condensates so far. It is noteworthy that following the publication of this work [127] the discussion on the differentiation of interference features arising from linear and non-linear dynamics has been stimulated [128–130].

Disclaimer:

The author contributed to these results by guiding and assisting the lead author of the publication [127] in the implementation of the main experimental configurations as well as in the analysis of the acquired data and interpretation of results and also contributed in a smaller extent to the editing of the manuscript. The simulations were performed by T. Ostanicky. The original interpretation that the observed features in the experiment are in fact interference patterns of linear wave propagation was first proposed by the author.

CHAPTER 3

Microcavity Samples and Experimental Techniques

3.1 Experimental methods

3.1.1 Coherent excitation sources

In this thesis we have focused mainly on non-resonant excitation techniques for the formation of polariton condensates. Polaritons were created using a number of coherent light sources. A continuous wave (CW) excitation source was employed in order to study condensation phenomena in the quasi steady state dynamic equilibrium regime, while two pulsed excitation sources were also used, mainly for the study of dynamic processes in the picosecond scale with our streak camera system.

3.1.1.1 Continuous wave mono-mode Ti:Saph laser

The coherent light source used in the dynamic equilibrium experiments was a COHERENT MBR-110 monolithic block resonator Ti:Saph laser. This is a tie-bow ring cavity incorporating a thin etalon and electronic stabilisation for hopping-free single mode operation. A birefringent filter in the cavity allows for coarse tuning of the emission wavelength while fine tuning can be achieved by tilting the angle of the etalon. Unidirectional lasing is inhibited by an optical isolator allowing only a single direction for light circulation. Locking of the lasing mode to one of the interference fringes of a stabilised high finesse reference cavity can facilitate the reduction of the lasing linewidth to <75Khz.

The Ti:Saph crystal was pumped by a 10 Watt green diode laser. The system had a typical output power of the order of 1 Watt for the centre of the gain curve around 800 nm while for the typical excitation wavelengths in the experiments of section 4 and section 5 it was of the order of 700mW. Fig. 3.1a shows a measurement of the stability of the laser over 16 minutes of operation. The statistics from the corresponding histogram give a intensity deviation of less than 0.5% for this time range and power Fig. 3.1b.

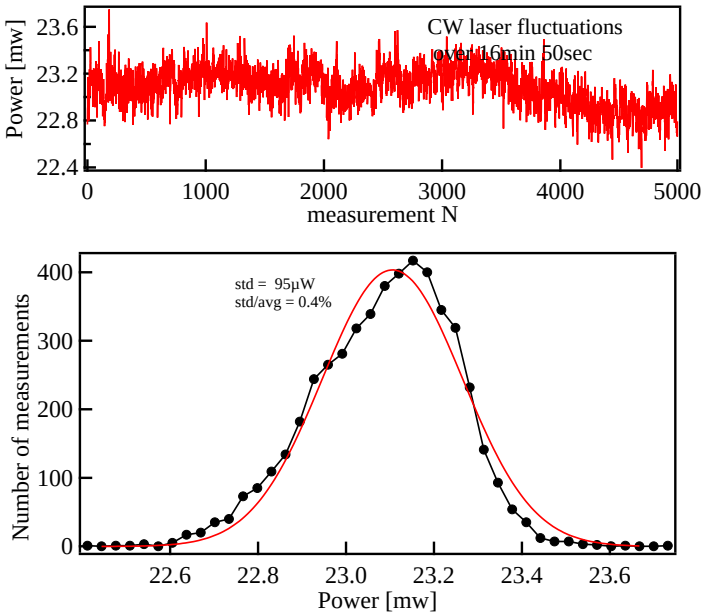

FIGURE 3.1: Continuous Wave laser fluctuations. Top panel, power fluctuations over time, bottom panel, histogram of measurements fitted with a Gaussian distribution.

3.1.1.2 Modelocked femtosecond Ti:Saph oscillator

To study the transient dynamics of polariton condensate formation a pulsed excitation with duration significantly lower than the polariton lifetime is required. For the transient experiments presented here a COHERENT Mira 900-F Ti:Saph ultra-fast laser with a repetition rate of 80MHz was used. In the pulsed lasing operational mode, mode-locking is accomplished by employing a Kerr Lens Mode-locking technique. The optical output is dispersion compensated resulting in 200 femtosecond pulses. The optical pumping power for the Ti:Saph crystal was provided by a 5 Watt green diode laser and the system has an efficiency of the order of 10% at the centre of the gain curve.

3.1.1.3 Regenerative amplifier

For experiments in the high density regime a Q-switched Ti:Saph regenerative COHERENT Rega amplifier was used for amplification of the ultra-fast oscillator pulses. The output of the amplifier has a tunable repetition rate of a 100kHz-250kHz and the pulse energy can be as high as $1\mu J$. A pulse compressor fitted in the system allows for re-compression of the output optical pulses to less than 300fs.

3.2 Experimental configurations

Experimental detection of polaritonic emission is accomplished by detecting the photons emitted out of the cavity upon the radiative decay of polaritons. These emitted photons carry information about all of the properties of the decayed polaritons and this allows for a full characterisation of polariton condensates by optical detection techniques. In this section we describe the majority of the experimental configurations used throughout the rest of this thesis. The experiments with the optical trap were conducted in a cold finger Oxford Instruments low-noise optical cryostat at temperatures of 5K-7K. The temperature was monitored with an Oxford Instruments intelligent temperature controller and was automatically recorded for every set of experimental data.

3.2.1 Polariton spectroscopy in reflection configuration

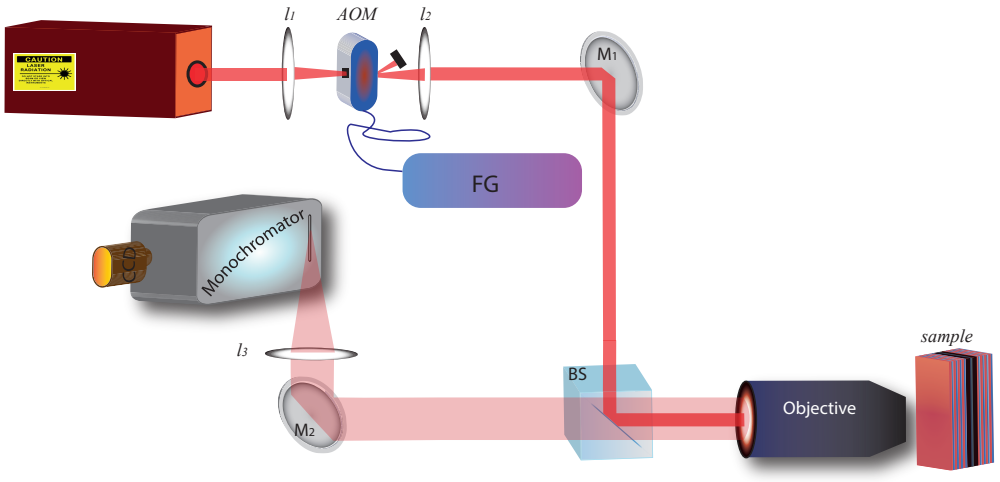

FIGURE 3.2: Polariton excitation and detection setup in reflective geometry. *l1,l2* are convex lenses used to focus and collimate the excitation in an acousto-optic modulator (AOM) driven by a function generator (FG). The first diffracted beam is then directed to the objective and focused on the sample. Polariton photoluminescence is collected with the same objective and focused on the slit of a spectrometer fitted with a CCD camera

The basic experimental setup used is shown in fig. 3.2. The excitation beam is focused on the aperture of an acousto-optic modulator. The first order diffracted beam is then collimated and directed to the focusing objective. A function generator (FG) is employed to switch the acousto-optic signal on and off with variable frequencies from 1KHz-10KHz and to tune the duty cycle of the excitation from 0.5% to 50% while variation of the FG signal strength is used to modulate the intensity of the diffracted beam. This accomplishes two aims simultaneously; the reduction of the relative time that the laser illuminates the sample, which is useful for suppressing laser induced heating effects when using high power excitation, while also providing a robust automated method to perform power dependence measurements by computer control of the FG. Alternatively, for the pulsed excitation a linear polariser and a $\lambda/2$ mounted on an automated rotation stage are used for attenuating the intensity of the laser in a controlled fashion. The excitation passes through a 50-50 beam splitter and directed to the focusing objective. The other half of the beam propagating through the beam-splitter is sent to a power detector sensor for monitoring and automated recording of the power during measurements.

The photoluminescence is then collected with the same objective and focused on the slit of a 300 mm spectrometer system coupled to an electron multiplication charged coupled device (EMCCD). A long (wavelength) pass filter is used to block the reflected part of the beam. The spectrometer is equipped with a triple turret featuring a 1200 grooves/mm grating providing a resolution of $\approx 170\mu eV$ at $800nm$, a 300 groove/mm grating, used for measurements in the near UV and a mirror. Using the spectrometer in the mirror configuration and leaving the slit open we can record the real-space emission from the sample. In the grating configuration we record images with real-space resolution in one direction (parallel to the slit) and energy resolved in the other. Additionally the polariton energy dispersion can be accessed by imaging the far-field of the emission which can be accomplished by imaging the back focal plane of the objective.

3.2.2 Spatial modulation of excitation

The engineering of the energy landscape of a polariton fluid by optical means was first decidedly demonstrated in 2010 in the work of Amo *et al.* [131]. This was followed by experimental reports of polariton condensate confinement by optically induced potentials, first in a semiconductor microcavity etched into a one dimensional ridge [132], and then confined between two excitation spots [133] thus demonstrated the feasibility of sculpting arbitrary potentials in the in-plane energy landscape of polaritons. To this effect a full two-dimensional optical trapping scheme was devised and implemented. Instead of using a spatial light modulator to shape

the beam profile a straightforward analogue scheme was employed making use of conical lenses.

In order to create an optical trap on the sample, a set of two axicons (conical lenses) were used to shape the excitation into a ring-shaped beam [134]. The set of axicons creates a ring shaped image in real space which is then projected onto the sample using a long distance lens and an objective that focus the rim of the hollow beam(fig. 3.3). Different ring sizes are achieved by changing the magnification of the lens-objective system. With this setup annular optical traps with sizes ranging from radii of $8\mu m$ to more than $30\mu m$ were projected on a microcavity sample.

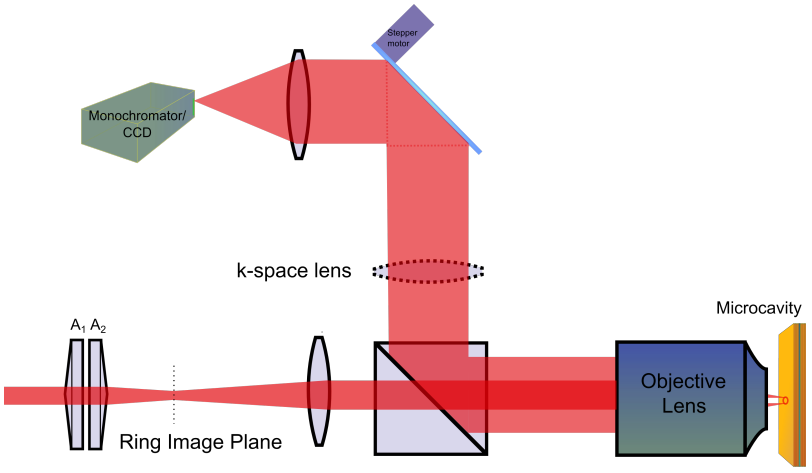

FIGURE 3.3: Hollow beam generation with the axicons used for the polariton trap. Two axicons placed back to back form the beam in the shape of a ring in real space. The image plane of the double axicons is then projected and focused on the sample with the use of a convex lens and an objective.

3.2.3 Stabilised Michelson Interferometry

To probe the build up of long range order as well as to determine the condensate phase, interferometric measurements were conducted using a stabilised Michelson interferometer similar to the one in the study of Kasprzak et al. [20] and originally engineered by Wehner et al. [135]. The interferometer was designed to operate in a mirror retro-reflector configuration with close to zero arm length difference. This configuration has the advantage of allowing direct measurement of the cross-correlation of all distances in one instance. Moreover, the arm length difference was actively stabilised by a frequency stabilised He-Ne laser in a PID feedback loop (fig. 3.4).

The polarisation of the stabilisation laser is initially diagonal while as it passes through the two arms only the vertical and horizontal components for the two different arms are allowed to propagate. This is achieved with two linear polarisers

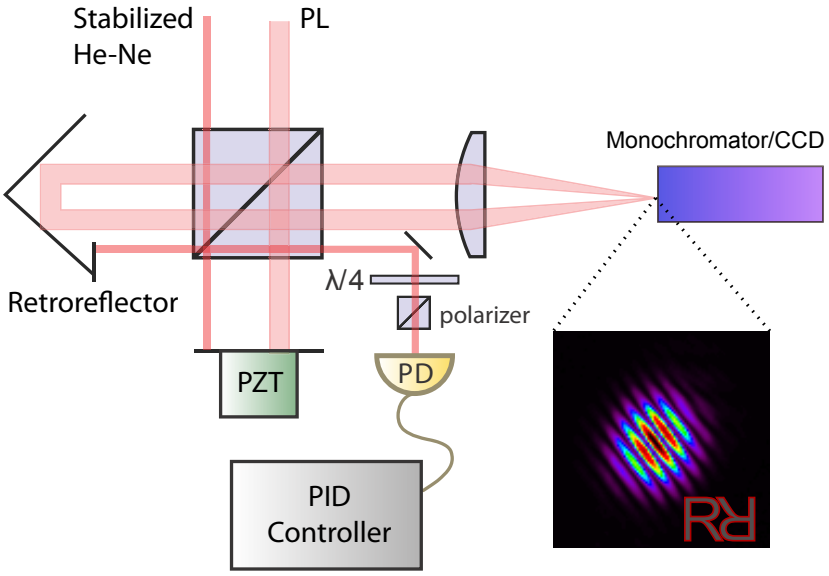

FIGURE 3.4: Stabilised Michelson interferometer in the retroreflector configuration

placed in the path of the reference beam for each arm. A $\lambda/4$ prior to the monitoring photo-diode with one of its axis oriented with a $45°$ relative to the horizontal results in two cross-circular polarisations that don't interfere but have a net linear polarisation with an angle that is dependent on the path difference δ. Finally a linear polariser is introduced. The resulting intensity of the beam that is focused on the photo-diode is dependent on the angle of the last linear polariser relative to the angle of the linear polarisation of the sum of the two beams. The total intensity on the photo-diode is thus $I = 2I_0 cos^2(\frac{\delta}{2} - \phi + \frac{pi}{4})$ where I_0 is the intensity from each arm and ϕ the angle of the linear polariser. The diode signal is passed through a proportional-integral-derivative (PID) controller that sends a signal to the piezoelectric stage in order to compensate for any vibrations that effectively modulate the intensity signal. Thus the contrast of the resulting interference pattern is of high quality. The linear polariser is mounted on an automated rotation stage. This enables scanning of the phase of the interference pattern in a highly controlled fashion enabling the extraction of the first order correlation function $G^{(1)}$ [136].

3.2.4 Spectral and temporal tomography techniques

To examine the full dynamics and energy distribution of polaritons a range of tomography techniques were employed. This enables the reconstruction of the real and momentum space emission of the polariton condensate for a discreet energy bands equal to the spectral resolution of the spectrometer. To accomplish this we scan the angle of the last mirror in fig. 3.2 with a computerised translation stage, effectively scanning the real (momentum) space image across the closed slit of the

spectrometer. From the acquired data the energy tomography images can then be assembled (fig. 3.5a).

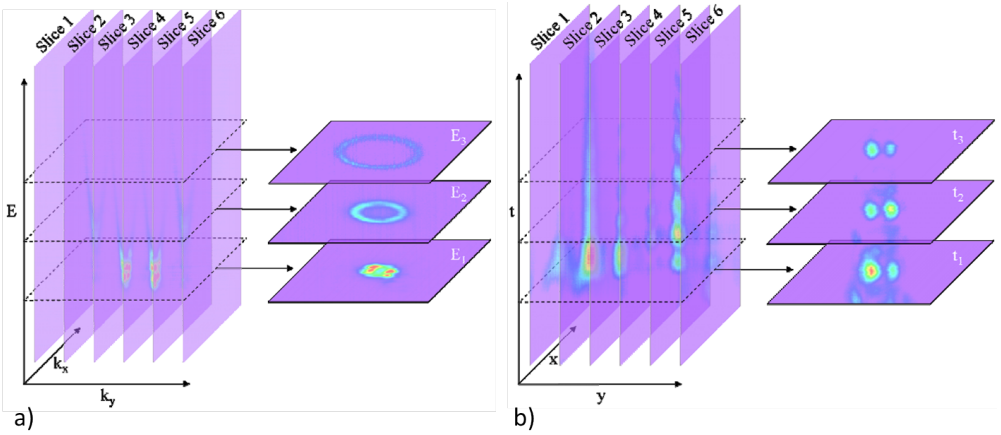

FIGURE 3.5: Schematic representation of the spectral and temporal tomographic techniques. a) A set of energy resolved images are acquired with each one corresponding to a specific k_y (alternatively Y), while the other axis of the image is k_x (alternatively X). This allows for the re-composition of the acquired images into real (or momentum) space images for each energy. b) Schematic representation of the temporal tomographic technique. A set of temporally resolved images are acquired with the use of our streak system. Each image corresponds to a specific y (alternatively k_y), while the other axis of the image is x (alternatively k_x). Re-composition of the acquired images into a set of real (or momentum) space images for different times is then possible. For b) it is also possible to acquire images with one axis being time and the other energy for a specific k_x, thus allowing for the reconstruction of dispersion images for different times. Figures from [136, chapter 2]

In a similar way temporal tomographic measurements can be performed. The streak camera system is coupled to the spectrometer and allows for the acquisition of two dimensional images with one of the axis being time and the other one defined by the spectrometer configuration and detection setup. In this way it is possible to reconstruct real space as well as momentum space images for different times (fig. 3.5b). Lastly it is also possible to scan an energy dispersion image across the slit of the streak acquiring a set of images with one axis being time and the other one being energy, each for a specific k_x (or alternatively x). In this way the momentum distribution for every "time-frame" can be reconstructed. The assembled tomographic images can be refined by bilinear interpolation in order to increase the resolution along the scanned dimension.

3.2.5 Application of external magnetic field

In this section we describe the superconducting magnet cryostat and the setup that was used for the experiments of chapters 8 and 9. The cryostat used was an Oxford Instruments spectromag optical cryostat system allowing for the application of

magnetic fields of up to 7 Tesla on the sample, for magnet operation at 4.2K. The orientation of the field was perpendicular to the plane of the sample (Faraday geometry) and the microcavity was held in the liquid helium boil-off at temperatures of 4K-7K.

3.2.5.1 Magnet Cryostat setup

The excitation from the CW source is passed through an AOM and the first deflected beam is then directed to the sample space and focused by a 200mm 3-inch lens and photoluminescence from the sample is collected by the same lens. The laser can theoretically be focused to less than $15\mu m$ for these excitation conditions and for an excitation wavelength of $\lambda_0 = 752nm$ if the full NA of the lens is employed. However, the measured spot diameter (FWHM) with this system was $\sim 40\mu m$. This value can be further reduced, to the order of $20\mu m$ by magnifying the beam by a factor of 4 before the final focusing lens to take advantage of the full NA of the system. The excitation can be attenuated by the AOM as described previously. For polarisation resolved experiments, a $\lambda/4$ oriented at a 45° angle with respect to horizontal, converts the left and right-handed circular polarisations of the signal, corresponding to the S_+ and S_- polariton states, to linear. A 5^o divergence Wollaston prism then splits horizontal and vertical polarisations into two discrete beams both travelling along the initial vertical propagation axis, which couple to a 800mm double grating (1200 grooves per mm) spectrometer. The signal is finally detected by a CCD camera. The resolution of the system is of the order of $40\mu eV$ for a wavelength of 800nm.

For the requirements of the series of power dependence measurements, a stepper motor connected to an ND filter wheel is utilised to assure that the signal doesn't saturate the CCD as the excitation power is increased. The non-automated part of the procedure consists of initially recording the power for each voltage step. At the end of every power dependence measurement the magnet controller automatically begins raising the field until the next set step and the procedure is then repeated. Furthermore the program also monitors and records the sample temperature for each measurement, helping in the better interpretation of the acquired data.

3.3 Microcavity Samples

In this section the microcavity sample used in the experiments described in the following chapters is thoroughly described. A state of the art strain compensated microcavity sample fabricated in the Sheffield III-V centre is also presented featuring for the first time steady state polariton condensation in a microcavity with InGaAs quantum wells.

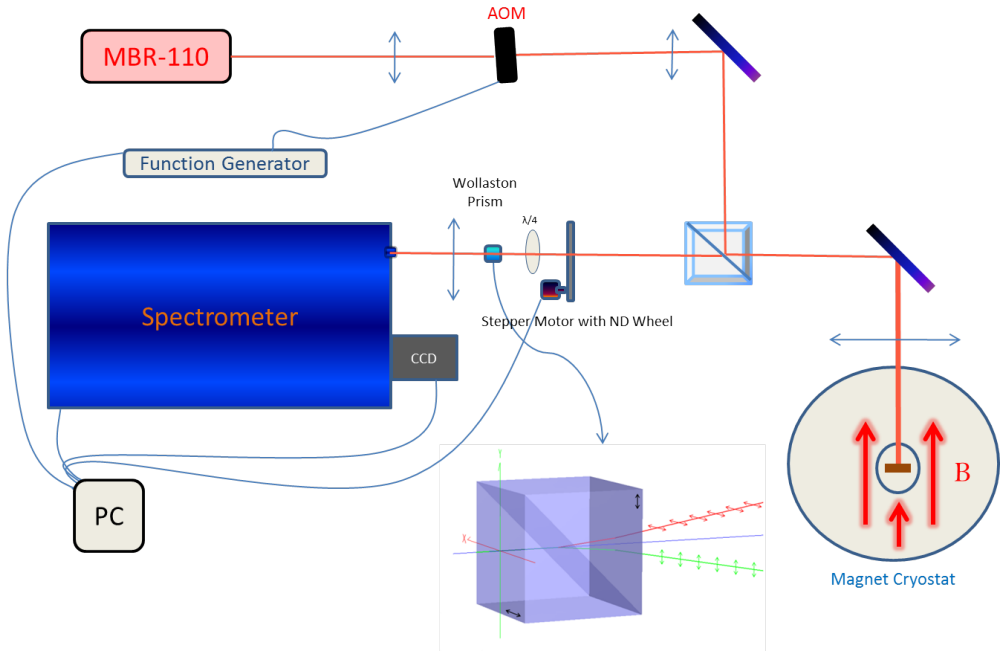

FIGURE 3.6: Experimental setup for the study of polariton condensation under magnetic fields in the Faraday geometry.

3.3.1 High Q factor microcavity with GaAs quantum wells

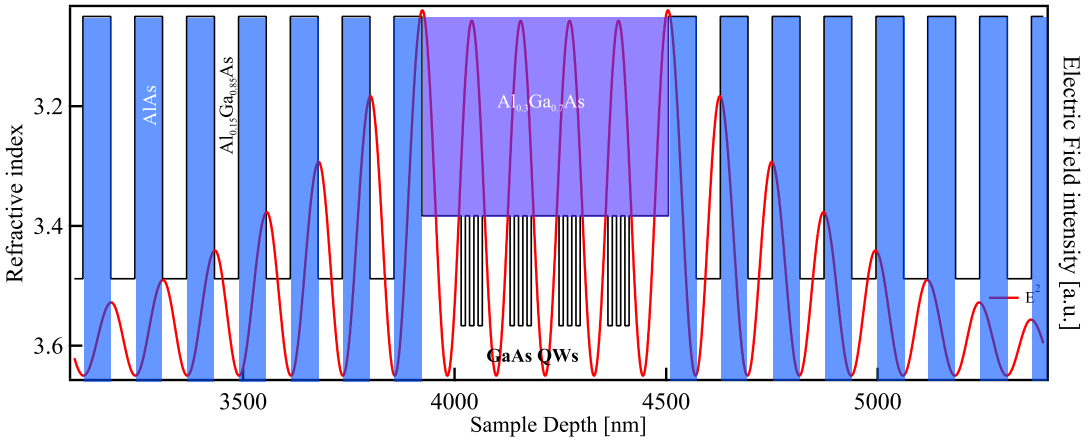

FIGURE 3.7: Microcavity structure overlaid with a TM simulation of the electric field of the lower polariton mode.

The first sample that was studied is a high Q factor (~ 15000) AlGaAs Microcavity that was grown in the Microelectronics Research Group (MRG) of the Foundation of Research and Technology (FORTH) in Crete by molecular beam epitaxy by Professor Zacharias Chatzopoulos and was designed by Professor Pavlos Savvidis and Dr. Simeon Tsintzos. The $\frac{5\lambda}{2}$ cavity consists of 4 triplets of 10nm GaAs QWs embedded within an $Al_{0.3}Ga_{0.7}As$ cavity spacer that is encompassed by two AlAs/$Al_{0.15}Ga_{0.7}As$ DBR stacks of 32 (top) and 35 (bottom) periods.The microcavity has been designed so that the middle QW of each triplet of QWs stands at an antinode of the field inside the cavity as seen on fig. 3.7.

The calculated stop-band width for the structure is approximately 127 meV and exhibits a very high reflectivity of >99.8% as calculated by a transfer matrix simulation of the structure (fig. 3.8). As is often the case with microcavity samples the cavity layer is not uniform throughout the sample but is tapered to allow for tuning of the cavity resonance across the sample by changing position on the sample. The vacuum Rabi splitting of the polaritons has been reported to be 9meV at 5K [137].

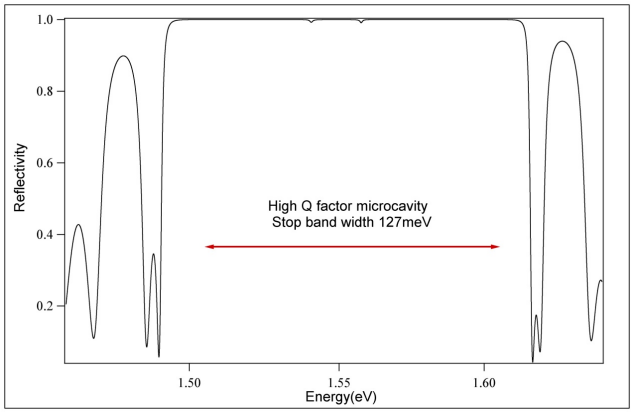

FIGURE 3.8: Transfer Matrix simulation of the reflectivity spectrum of the GaAs microcavity sample.

Transmission electron microscopy (TEM) images conducted by the growth group post growth reveal that the thickness of individual layers is uniform throughout the structure except for a wavy behaviour observed in the final layers of the structure (fig. 3.9a). The structure was designed to have a Q-factor close to 20000. Experimental photoluminescence measurements at a cryogenic temperature (6K) below threshold, conducted by the author with the double pass spectrometer of the magnet setup, at the most negative detuning available on the examined part of the sample ($\delta = -9.5meV$), where the polariton exciton Hopfield coefficient was only 12% revealed a polariton linewidth of $\sim 90\mu eV$ (fig. 3.9b). This corresponds to a low limit for the sample Q-factor of ~ 17000, proving that this cavity structure is indeed state of the art. This measurement was included in the report of Tsotsis *et al.* detailing polariton condensation on this sample and the author's contribution acknowledged therein [137] .

Using eq. 1.8 the measured linewidth can also be used for an accurate determination of the polariton lifetime and this calculation yields τ_{lp}=7ps. The polariton lasing threshold is thus expected to be comparatively low for this structure while contrary the exciton saturation density is theoretically anticipated to be relatively large due to the multiple QWs coupled to the cavity mode.

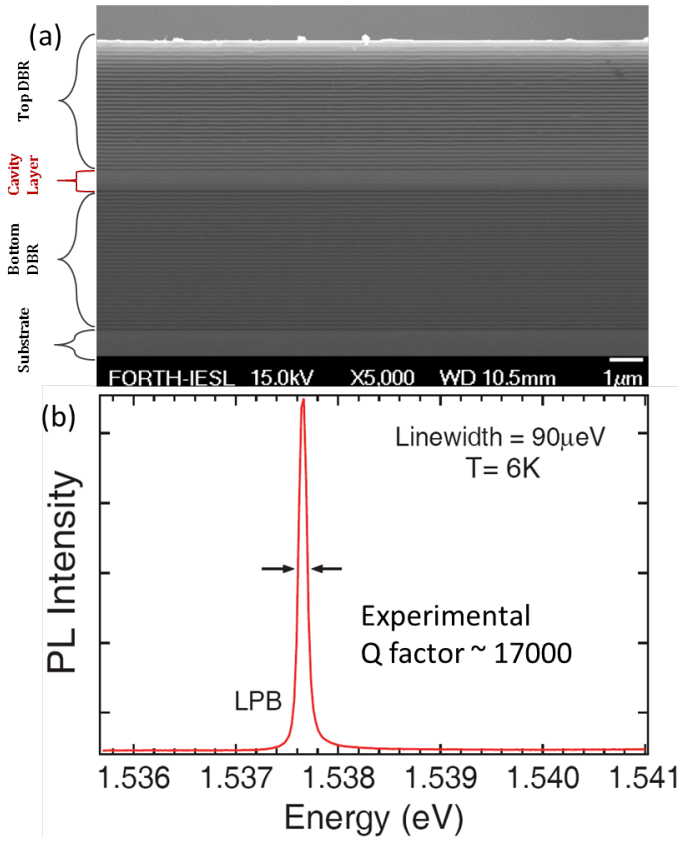

FIGURE 3.9: **a)** TEM image of the sample. **b)** Photoluminescence measurement below threshold for the investigated microcavity used for the determination of the Quality factor from ref. [137].

3.3.2 Strain compensated microcavity with InGaAs quantum wells

Polariton BEC phase transitions have been demonstrated in a wide range of materials. Condensation at room temperature under optical excitation has been reported in GaN [21] and more recently in ZnO [44] and organic semiconductor systems [138]. In III-V materials, polariton condensation and lasing has been reported in MCs with GaAs QWs [139]. The implementation of electrically injected polariton condensates has also been reported in GaAs [24, 25] and recently in GaN at room temperature [26]. Among these materials AlAs/GaAs MCs are currently the preferred system for the study of polariton fluidics due to low photonic and QW disorder combined with a moderate exciton binding energy (~ 10 meV). Nevertheless, the presence of cross-hatched dislocations affects the dynamics of polaritons giving rise to localisation [140] and scattering [141–144] phenomena that limit the propagation of polaritons within the cavity plane.

Sample description and characterisation

In previous related works, Zajac et al [145] showed that the cross-hatched dislocation density can be reduced by introducing strain-compensating AlP layers into the centre of the AlAs layer of the distributed Bragg reflectors (DBRs). To this effect a a strain compensated 2λ GaAs microcavity with embedded InGaAs QWs was developed in Sheffield National Centre for III-V technologies by Dr. Edmund Clarke and Dr. Faebian Bastiman. In this structure strain compensation was achieved by using $AlAs_{0.98}P_{0.02}/GaAs$ DBR layers instead of thin AlP inserts in the AlAs layers used in previous structures [145] as their effective composition could be better controlled during the growth process. The bottom DBR consists of 26 pairs of GaAs and $AlAs_{0.98}P_{0.02}$ while the top has 23 of these pairs as shown in Fig. 3.10a, resulting in very high reflectance (>99.9%) in the stop-band region of the spectrum as shown in Fig. 3.10b. Three pairs of 6 nm $In_{0.08}Ga_{0.92}As$ QWs are embedded in the GaAs cavity at the anti-nodes of the field as well as two additional QWs at the first and last node to serve as carrier collection wells, as shown in Fig. 3.10c. The large number of QWs was chosen to increase the Rabi splitting and keep the exciton density per QW below the Mott density [146] for sufficiently high polariton densities in order to achieve polariton condensation. A wedge in the cavity thickness allows access to a wide range of exciton-cavity detuning. The average density of hatches along the [110] direction was estimated from transmission imaging to be about 6/mm, while no hatches along the $[1\bar{1}0]$ direction were observed, as exemplified in Fig. 3.10d.

In the experiments the sample was held in a cold finger cryostat at a temperature of $T = 6\,\mathrm{K}$. The optical excitation, for all the measurements described here, was at the first reflectivity minimum above the cavity stop band, as shown in fig. 3.10b. The photoluminescence from the lower polariton (LP) was acquired with $\pm 40^\circ$ collection angle, by a 0.65 NA microscope objective and was spectrally resolved using a 1200 grooves/mm grating in a $300\,\mathrm{mm}$ spectrometer coupled to a cooled charge coupled device. The spectrally and in-plane wave-vector (k) resolved emission intensity at low excitation fluence and at a detuning of $\Delta = -5\,\mathrm{meV}$ is shown in fig. 3.10e. Extracting the upper polariton (UP) and LP energy at $k \sim 0$ across the thickness gradient of our sample, we find the detuning dependence shown in fig. 3.10f. To fit the experimental data we use a system of two coupled harmonic oscillators [32]. The strong coupling between the exciton resonance and the cavity mode is observed with a vacuum Rabi-splitting of $2\hbar\Omega \sim 8\,\mathrm{meV}$. From the transmitted spectra at $\Delta = -5.8\,\mathrm{meV}$ shown in fig. 3.10b, at which the LP has a (resolution corrected) linewidth of 120 ± 50 μeV and an exciton fraction of 20.5%, we obtain a LP Q-factor of ~ 12000 while the calculated bare cavity Q-factor, neglecting in-plane disorder and residual absorption, is ~ 25000. This theoretical simulation was performed using the low temperature ($\sim$ 6K) refractive indices of 3.556 and 3.015 for the GaAs

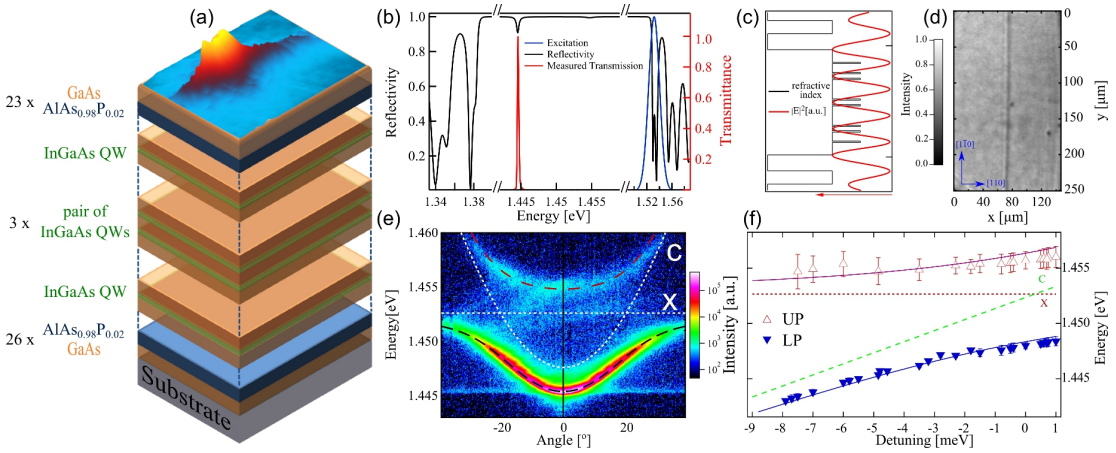

FIGURE 3.10: **(a)** Sketch of the microcavity structure and condensate emission. (b) Calculated reflectivity of the cavity stop band with the transfer matrix method (black line), spectra of pulsed excitation (blue) and experimental transmittance spectrum (red) for detuning $\Delta = -5.8$ meV. (c) Sketch of the refractive index (black line) along the growth direction and the corresponding square of the electric field of the cavity mode (red line). (d) Real space transmission intensity image of the sample surface under white light illumination on a linear gray scale, as indicated. (e) Polariton dispersion at low excitation fluence on a logarithmic color scale as given. The white dashed lines depict the bare exciton (X) and cavity (C) modes and the blue and red solid lines the calculated UP and LP dispersions. (f) UP and LP energy at normal incidence for different detuning conditions. The error bars correspond to the FWHM of a Gaussian fit to the spectra, the blue (purple) line show the calculated UP (LP), and the dashed green (red) line shows the bare cavity (exciton) mode.

and $AlAs_{0.98}P_{0.02}$ layers respectively at the cavity resonance. As the emission energy of the InGaAs QWs is lower than the absorption of the GaAs substrate we can study the photoluminescence of the sample both in reflection and transmission geometry. The transmission geometry, which is not available for GaAs QWs, allows to filter the surface reflection of the excitation, and has been widely utilised to probe the features of polariton fluids [93, 147] under resonant excitation of the lower polariton branch. We use non-resonant excitation from the epi-side, and detect the emission from the substrate side, so that the excitation is filtered by the absorption of the GaAs substrate.

Polariton condensation and transition to photon lasing

In order to achieve condensation into the LP ground state at $k \sim 0$ we excite with a spot of 35 μm full width half maximum (FWHM). For smaller excitation sizes condensation at $k > 0$ was observed, which is due to a steeper potential profile induced by the repulsive exciton-exciton interactions in the reservoir.

The optical excitation pulses of 180 fs duration and 80 MHz repetition rate are provided by a Ti:Sapphire laser. They excite electron-hole pairs in the InGaAs QWs

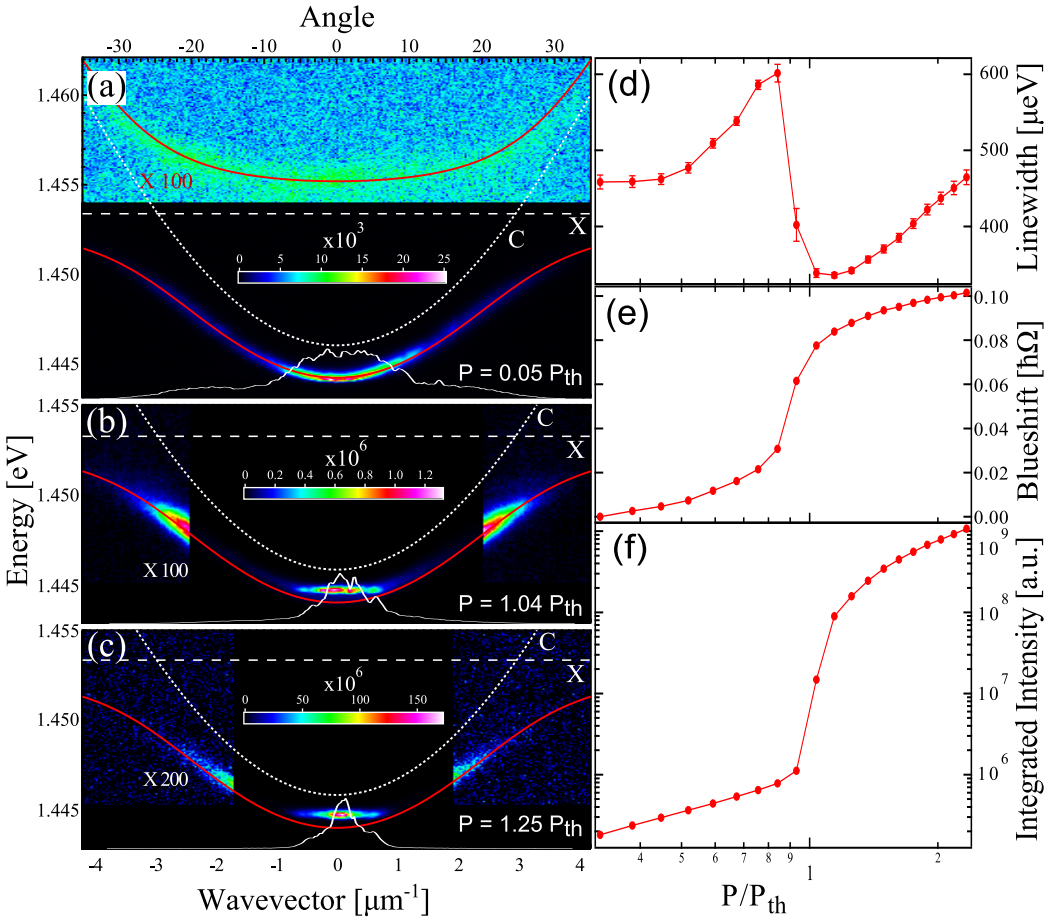

FIGURE 3.11: Energy and wave-vector resolved emission intensity on a linear colour scale as indicated, (a) below, (b) at, and (c) above threshold. The red lines show the calculated LP and UP dispersions, and the dotted and dashed white lines show the uncoupled low-density cavity (C) and exciton (X) dispersion, respectively. In (a) the UP energy range is also shown, scaled as indicated. The data has been scaled in (b) for $|k| > 2.5\,\mu\text{m}^{-1}$ and in (c) for $|k| > 1.8\,\mu\text{m}^{-1}$ as indicated. Profiles of the LP emission along k are also shown as white lines. (d) LP linewidth, (e) energy shift in units of the Rabi Splitting $2\hbar\Omega$ and (f) intensity, at $k \sim 0$ versus excitation fluence.

and GaAs cavity which rapidly relax to populate the LP dispersion and the weakly coupled QW exciton reservoir. With increasing exciton and polariton density the polariton relaxation rate increases, eventually overcoming the threshold for condensation when the relaxation into the ground state of the LP supersedes its radiative decay, resulting in a macroscopic ground state population [20]. Fig. 3.11a shows the energy and wave-vector resolved emission intensity in the low fluence regime, where re-normalisation due to particle interactions is insignificant. The lower polariton mode is clearly discernible, as well as the upper polariton mode but for a significantly lower emission intensity. Already at this very low density polaritons heavily populate the ground state which is a good indication that the cavity lifetime of the system is sufficiently high to allow for thermalisation of carriers before radiative decay. With increasing excitation fluence P we observe a threshold

at $P_{\mathrm{thr}} = 26\,\mu\mathrm{J/cm^2}$ at which the emission shrinks in momentum space as shown by the intensity profiles in fig. 3.11a-c. Also above threshold the emission at high k is following the expected LP dispersion, confirming the strong coupling regime. The LP spectrum at $k \sim 0$ also displays the expected features for polariton condensation, namely linewidth narrowing in fig. 3.11d, a blue-shift of the polariton mode in fig. 3.11e, and a non-linear increase in intensity in fig. 3.11f. Increasing the fluence above threshold, interactions between the polariton condensate and the exciton reservoir increase, resulting in a broadening and blue-shift of the condensate emission (as will be shown in more detail in chapter 4). It is worth mentioning here that we also observe condensation under CW optical excitation for small excitation spot sizes were the condensate forms at a high wavevector as for the spot size required for condensation in the $\mathrm{K}_{\parallel} = 0$ state our setup doesn't have the necessary power requirements.

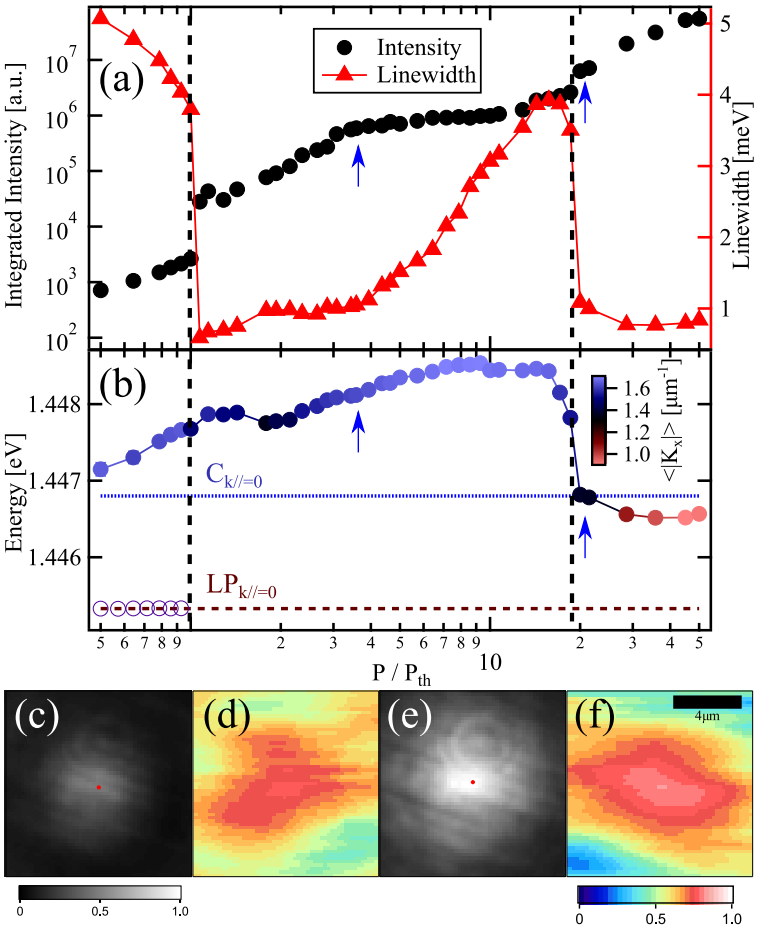

FIGURE 3.12: LP emission using an excitation size of $9.2\,\mu$m FWHM, as function of the excitation fluence P relative to the polariton condensation threshold $P_{\mathrm{th}} = 28\,\mu\mathrm{J/cm^2}$. (a) linewidth, and spectrally integrated intensity, collected over $|k| < 3.4\ \mu\mathrm{m}^{-1}$. (b) Average energy, color coded with the average wavevector $\langle|\mathrm{k}|\rangle$. (c),(e) Spatially resolved emission intensity and (d),(f) fringe visibility in the regime of polariton condensation at $P = 3.8P_{\mathrm{th}}$ (c,d) and photon lasing at $P = 20P_{\mathrm{th}}$ (e,f), as indicated by the two blue arrows in (a,b). The visibility is averaged over 24 different phase shifts. The red spots in (c) and (e) indicate $\mathrm{r} = 0$ used in (d), (f).

To observe the transition from polariton condensation to photon lasing in the weak coupling regime, we need a significantly higher excitation fluence, for which we reduce the excitation size to $9.2\,\mu$m FWHM. The smaller excitation spot leads to polariton condensation at $|k| > 0$ due to a steeper potential profile induced by the repulsive exciton-exciton interactions in the reservoir. To record the evolution of the emission intensity with increasing excitation fluence between the two regimes we integrate the emission over the entire LP, from 1.441 eV to 1.458 eV and $|k| < 3.4\ \mu\text{m}^{-1}$. As shown in fig. 3.12a, we now find two thresholds, with the second one at about 20 times higher fluence than the first, showing an abrupt increase in intensity and decrease in linewidth. We note that directionally integrating the emission broadens the resulting linewidth compared to fig. 3.11 and reduces the intensity difference between the linear and non-linear plateau. Fig. 3.12b shows the energy shift of the emission colour-coded with the average $\langle|\mathrm{k}|\rangle$ of the emission over the intensity distribution along the measured direction. As expected for a small excitation spot, the LP population build up occurs at $|k| > 0$, increasing with the excitation fluence. However upon crossing the second threshold the emission shifts towards the energy of the uncoupled cavity mode and $k = 0$. This second threshold is thus attributed to the transition to photon lasing [148]. To show the coherence build up above threshold we carried out interference measurements using an actively stabilised Michelson interferometer in a retro-reflector configuration measuring the coherence of the emission at $\mathbf{r}$ relative to $-\mathbf{r}$, with $\mathbf{r} = 0$ set to the emission peak as indicated in fig. 3.12c,e. The extracted fringe visibility in the polariton condensate and photon lasing domains are shown in fig. 3.12d,f. The measured visibility V of both the photon lasing and polariton condensate regime is extended and reaches up to about 80%, consistent with the expected coherence of the emission.

The observed non-linear increase of intensity, along with the observed linewidth momentum distribution narrowing and the appearance of a second threshold to photon lasing identify this phase transition as polariton condensation in the strong coupling regime. As this type of strain compensated microcavity has been shown to suppress cross-hatched defects [145], it promises to be a suited system for studying the intriguing nature of polariton quantum fluid phenomena [83, 91].

Disclaimer:

The results on polariton condensation in the strain compensated microcavity were published in reference [149]. The author of this thesis conducted the experiments and analysis of the steady state measurements under CW excitation, as well as the analysis and part of the experiments for the detuning characterisation of the sample

and performed the transfer matrix simulations. The analysis for the fringe visibility and of the $\langle|k|\rangle$ for the pulsed excitation experiments was also conducted by the author and finally the bulk of the manuscript was written by the author.

Part II

Polariton Condensates in Optically Imprinted Potentials

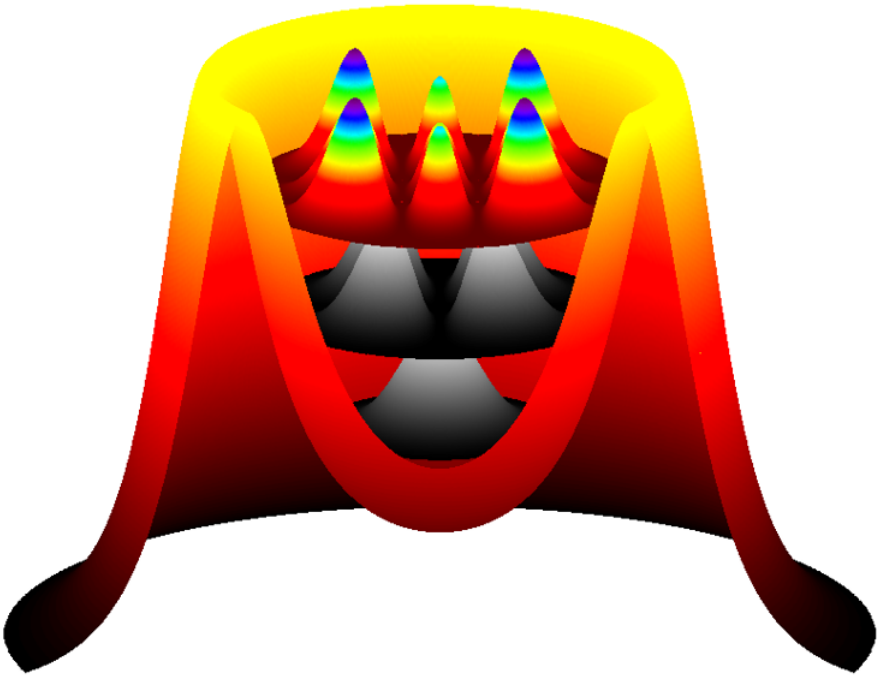

CHAPTER 4

Polariton Condensation Through Optical Trapping

As mentioned previously (see section 2.2) polariton condensation in an ideal infinite two-dimensional cavity is theoretically un-achievable in the absence of a confining potential. In such a system, the polariton gas is instead expected to undergo the Berezinsky-Kosterlitz-Thouless (BKT) phase transition [51]. However in realistic structures, polaritons can condense in traps induced by random optical disorder [20] or mechanically created potentials engineered by applying external stress on the microcavity [73, 150]. Polariton condensation has also been observed in structures of lower dimensionality [151–156] where the structure itself acts as the trapping potential as well as in defect cites of planar structures [157]. More recently, the manipulation of polariton condensates by means of optically "imprinted" potentials has been demonstrated [131–133, 158–160]. In these works the condensation process was not assisted by the optical potential but used to localise an already formed polariton condensate.

In this chapter we study the manifestation of polariton condensation assisted by an optically generated two dimensional potential, in dynamic equilibrium. We describe the trapping and condensation mechanism and perform a qualitative and quantitative comparison of its spectral features with that of a condensate optically pumped with a typical Gaussian excitation spot. This scheme allows for the formation of a polariton condensate spatially separated from the excitation spot. Owing to the efficient trapping in the optical potential we observe a reduced excitation density threshold as well as higher coherence due to the decoupling of the condensate from the exciton reservoir.

4.1 Implementation of optical trapping

For the purpose of imprinting a two-dimensional trap on the microcavity plane, the spatial profile of the non-resonant pump was shaped into a ring and projected onto a microcavity sample. The pump excites a population of polaritons and uncoupled excitons (and dark excitons) around the pumping region. However as excitons are much heavier than polaritons their propagation length is considerably shorter. The pump thus forms a 2D repulsive optical potential originating from the interactions of polaritons with the localised excitonic reservoir [132]. Polaritons propagating towards the centre of the trap can scatter with each other losing energy and becoming localised inside this potential. Increasing the population of particles in the trap eventually leads to the emergence of a confined polariton condensate that is spatially de-coupled from the de-coherence inducing excitonic reservoir, before any build up of coherence on the excitation region is observed. The observation of polariton condensation non-local to the laser excitation profile, prior to the build-up of coherence at the excitation area on the sample, conclusively proves that the coherence of the polariton condensate is not associated with or "seeded" by the coherence of the excitation laser [51]. Finally, we conduct a reference experiment, where the trapping mechanism is switched off, by changing the excitation intensity profile, and observe polariton condensation taking place for optical excitation densities more than two times higher while the resulting condensate is shown to be subject to much stronger de-phasing and depletion processes as indicated by the comparison of the spectral features of the $k_{//=0}$ polariton state.

The trap was created on the high quality factor GaAs/AlGaAs microcavity sample described previously (see section 3.3.1) which was held at $\sim 6.5\,\mathrm{K}$ in a cold-finger cryostat and excited non-resonantly at the first reflection minimum above the cavity stop band with the single-mode continuous wave laser(section 3.1.1.1). The excitation beam profile was shaped into a ring in real space with the use of two axicons and was projected to the microcavity through an objective lens ($\mathrm{NA} = 0.4$) creating a polariton ring with a mean diameter of $\sim 20\,\mu\mathrm{m}$ on the sample (see also fig. 3.3 section 3.2.2), which is of the order of the polariton mean free path in planar microcavities and of the exciton diffusion length of the quantum wells of our sample [156, 161, 162]. The excitation beam intensity was modulated with an acousto optic modulator (AOM) at 1% duty cycle with a frequency of $10\,\mathrm{kHz}$ to reduce heating effects. A high pass filter was used to block the reflection of the excitation beam.

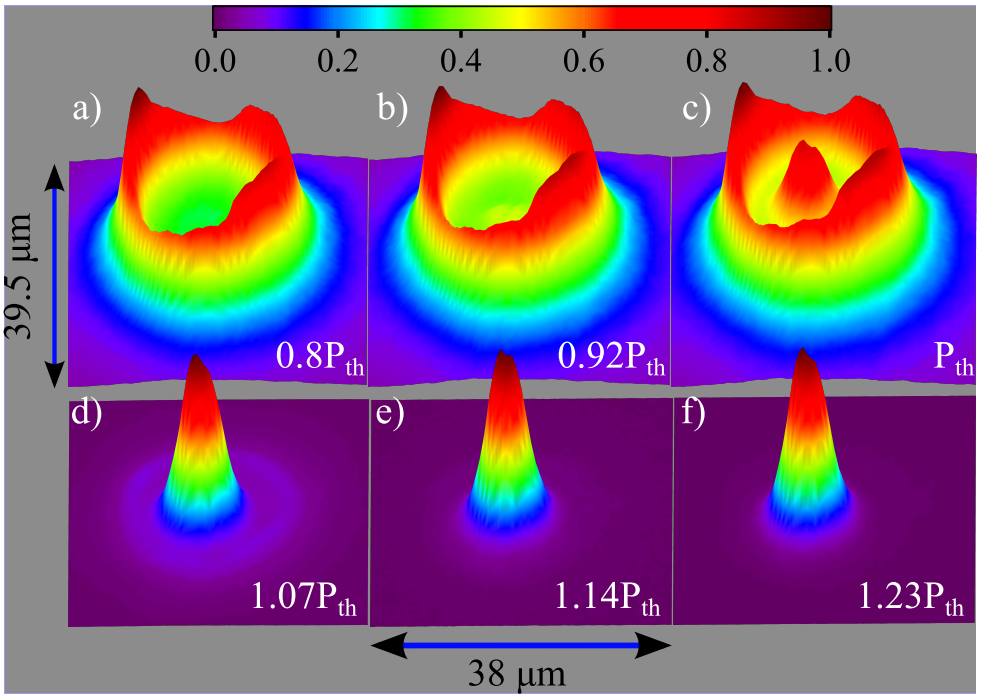

FIGURE 4.1: Observation of polariton condensation in real space inside the optical trap as the polariton density is increased above the condensation threshold from a) to f). a) For densities below threshold, photoluminescence is stronger from the optical excitation region while emission from inside the trap is minimal. b) and c)Increasing the particle density towards threshold a strong emission peak is gradually builds up. d) Just above threshold density the emission from the peak overtakes the emission form the trap barriers for over three orders of magnitude. For even further increase of the density emission from the excitation region can not be detected without saturation of the detector by the condensate intensity e) and f). The intensities of figures b)-f) are scaled by 1.14, 1.23, 21.5, 130 and 356 respectively compared to a).

4.2 Condensation in real and momentum space

Increase of the intensity of the excitation beam results in increased density of particles in the reservoir effectively raising the trap barrier. Polaritons are injected in the trap with increasing concentrations until the stimulated scattering threshold is reached. Upon condensation threshold the macroscopic polariton population remains well confined within the trapping potential resulting in the emergence of a sharp peak in real space that quickly overtakes, in intensity, the emission from the excitation region. A detailed build up of the condensate in real space is presented in fig. 4.1a-f.

In addition to the real space measurements we conduct a series of power dependence experiments in dispersion imaging in to order to monitor the build up of particles populating the centre of the trap and document the emergence of condensation inside the trap. Polariton emission in real space for powers greatly below threshold outlines the pump profile while the emission from the centre of the trap

is minimal (fig. 4.2a). As the excitation density is increased however, emission from trapped particles becomes comparable to emission from the pump region marking the onset of condensation (fig. 4.2b). Above threshold (fig. 4.2c,g) a Gaussian shaped single-mode condensate, with full width at half maximum (FWHM) of $5.46\,\mu\mathrm{m}$ and standard deviation $\sigma_x = 2.32\,\mu\mathrm{m}$, is formed and effectively confined inside the ring. The corresponding dispersion of polaritons originating from the entire emission of

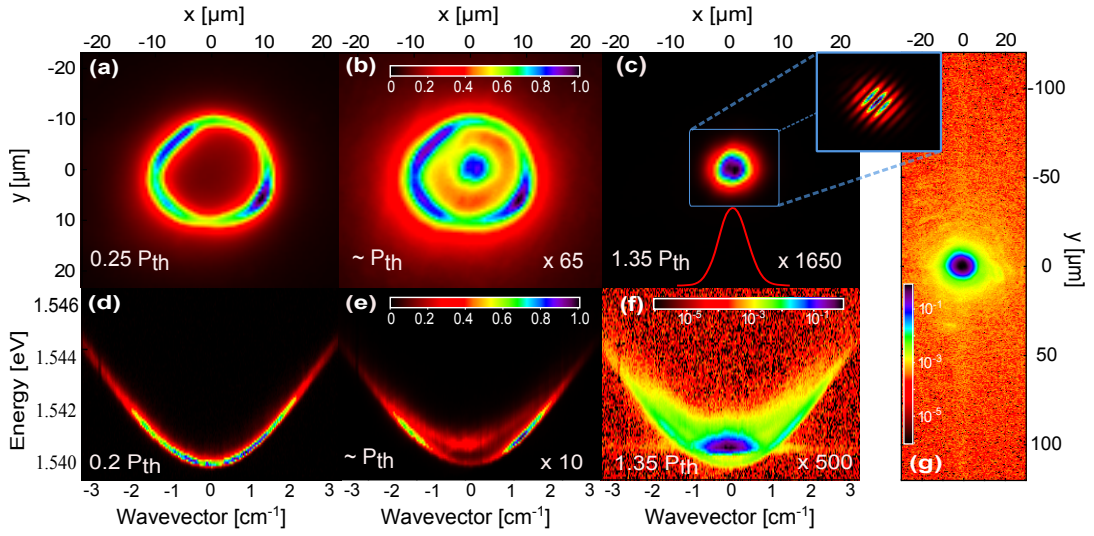

FIGURE 4.2: Single-mode exciton-polariton condensate in a ring-shaped trap. Emission images in real space below (a), at (b) and above threshold (c). The inset in (c) shows the interference fringes of the condensate. Red line in (c) is the condensate profile along the x axis. Polariton condensation is clearly visible in the centre of the ring and is separate from the excitation spot outlined by the emission in (a). (d), (e), (f) Dispersion images below (d), at (e) and above (f) threshold. (g), Same as (c) for a logarithmic colour-scale showing that propagation beyond the trap is suppressed.

the ring and for different pumping powers can be seen at fig. 4.2d-f. Below threshold we observe a typical lower polariton branch. As the polariton density in the centre of the ring is increased close to threshold, we observe a blue-shifted dispersion from the polaritons in the trap, coexisting with the dispersion of un-trapped polaritons as will be made evident from spatially resolved dispersion imaging. The two lobes of the outer dispersion in fig. 4.2e correspond to high momentum polaritons travelling from the excitation region outwards. By further increasing the excitation power a condensate appears in the ground state of the blue-shifted dispersion with zero in-plane momentum and standard deviation $\sigma_{k_x} = 0.24\,\mu\mathrm{m}^{-1}$, shown in logarithmic scale in fig. 4.2f. The macroscopically occupied ground state is very close to the Heisenberg limit, having $\sigma_x\sigma_{k_x} = 0.56$ lower than previously reported values [163] confirming that phase fluctuations within the condensate are strongly reduced and that this is a well defined quantum state.

Interferometric images of the emission above threshold, acquired with the stabilised Michelson interferometer, reveal coherent interference fringes (inset in Fig. 4.2c)

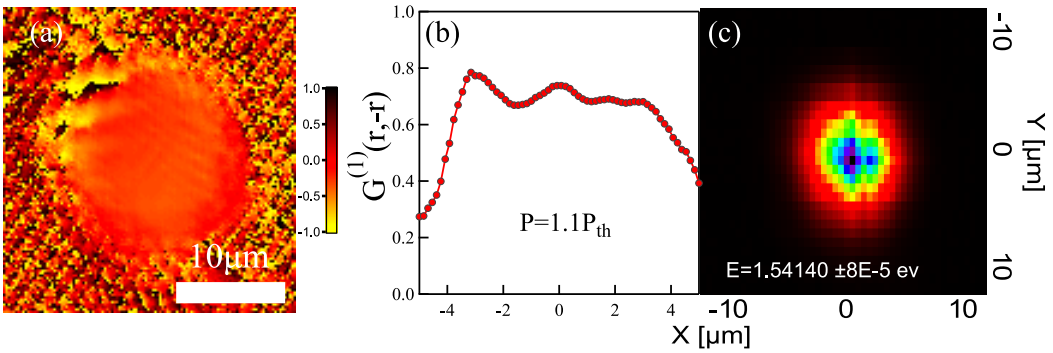

FIGURE 4.3: a) Condensate phase (in units of π) extracted with a digital holographic technique. b) First order correlation function across the centre of the condensate (y=0μm). c) Tomographic image of the condensate at the energy of peak intensity.

confirming the build-up of coherence in the system. Employing a digital Holographic technique [136, 164], the condensate phase can be extracted revealing a uniform phase over the entire condensate wavefunction. Scanning the piezo stage and recording the interference pattern for a number of steps, allows for the extraction of the first order correlation function $g^{(1)}$, similar to what is described in ref. [155], and this can be seen in fig. 4.3a were we observe a plateau of high coherence. Additionally a tomographic experiment (see section 3.2.4) was conducted, where again the real space two-dimensional profile fig. 4.3b at the condensate energy level further corroborates that the above threshold emission originates from a single energy level.

Spatially filtering the polariton dispersion from different regions of the emission, reveals that outside the excitation area, polaritons populate high energies and large wave-vectors (fig. 4.4b), while those in the centre of the trap primarily populate the lower states even at pump powers greatly below threshold (fig. 4.4a). The dispersion of the polaritons escaping the ring does not change significantly with increasing power (for the power range that we have examined), while the dispersion images at the centre of the trap demonstrate condensation at $k = 0$ above threshold. The profile of the trap at threshold can be visualised by energy resolving a central slice ($\sim 1.3\,\mu$m) of the excitation ring (fig. 4.4c). By extracting the energy that corresponds to the maximum intensity along each point of the x axis of fig. 4.4c, the trapping profile can be assembled (fig. 4.4d). The profile of the trap depth at threshold is $\sim 1\,$meV, while the two circles in fig. 4.4d annotate the points where the spatially filtered dispersions were acquired. It is worth noting here that this value gives only an approximate estimation of the trapping depth. Upon closer examination the signal at the trap barriers is of high momentum polaritons and therefore doesn't exactly correspond to the real blue-shift of the k=0 state, while on the contrary the emission from the trap centre is dominated by polaritons around

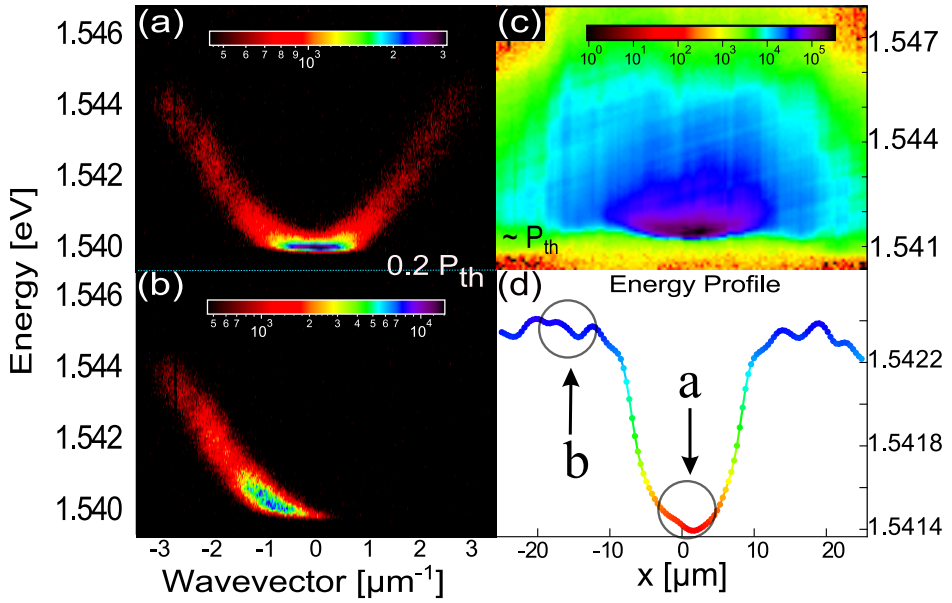

FIGURE 4.4: Trapping potential and spatially-resolved dispersions. (a), (b), Dispersion images below threshold ($P = 0.2P_{th}$) from a $5\,\mu$m diameter spatially filtered region from the centre of the ring (a) and from outside the excitation region (b). Energy profile of the central slice of the ring at threshold (c) and the extracted maxima of intensity along the x axis for visualisation of the trap profile (d). Points **a** and **b** at (d) correspond to (a) and (b) respectively.

k=0. Therefore the actual potential depth polaritons in the centre of the ring experience,due to increased interactions with the reservoir around the excitation region, is expected to be lower than 1meV.

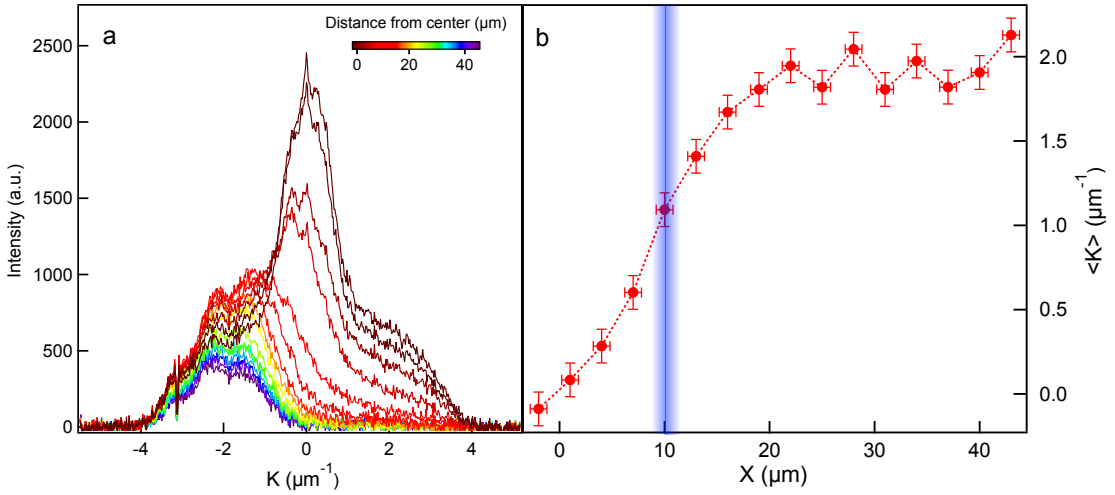

FIGURE 4.5: (a)Energy integrated profiles of the polariton dispersion from different regions of the real space emission for $P = 0.2P_{th}$. Profiles are colour-coded with the displacement from the centre of the ring trap. (b), Extracted $\langle|\mathbf{k}|\rangle$ vs distance from the centre of the trap. The blue line in (b) denotes the excitation region.

The different average momentum of particles in these two regions (excitation region and trap centre) strongly suggests that polaritons inside the trap exhibit an increased relaxation efficiency. This can be directly demonstrated by comparing

the polariton dispersion from different areas of the trap. The real space emission is filtered by a pinhole which is swept with $\sim 5\mu m$ incremental steps along the plane (in the X direction) from the centre of the trap up to $45\,\mu\mathrm{m}$ and for each step the polariton dispersion is recorded. Integrating the dispersion over energy yields the momentum (or wave-vector) profiles that can be seen in figure 4.5a where the colour-coding maps the distance of the filtering pinhole from the centre. It is straight forward to then extract $\langle|\mathrm{k}|\rangle = \frac{\sum k_i I_i}{I}$ for every profile and this is displayed in fig. 4.5b. It is clear from this analysis that inside the excitation region polaritons strongly populate the ground state in stark contrast to the high average momentum observed for particles propagating away from the excitation region. It is therefore clear that inside the trap "boundary" polariton relaxation is considerably more efficient than outside. Taking into account that exciton-polariton interactions are substantially suppressed due to the minimal diffusion of excitons inside the trap region the only other available mechanism that can account for this relaxation is polariton-polariton interactions.

4.2.1 Description of condensate formation

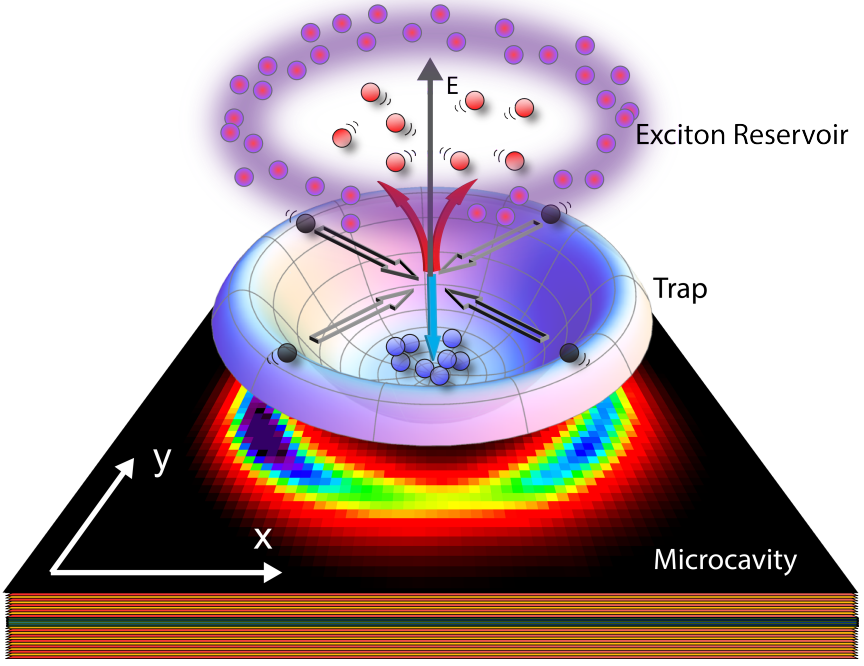

FIGURE 4.6: Polariton trap over real space excitation spot, displaying the trapping mechanism. Polaritons scattered to high energy states leave the trap, while those scattered to low energy and momentum remain confined.

With this insight we can now proceed to describe the entire process of the condensate formation in this novel optical trap. The non-resonant excitation creates a hot electron-hole plasma, which then forms excitons. Hot excitons cool down by exciton-phonon scatterings [165]. When they enter the light cone they couple

strongly to the cavity mode and populate the lower polariton branch on the ring. Excitons diffuse around the excitation area but due to their large effective mass they are unable to reach the centre of the ring. The repulsion of polaritons from the ring-shaped exciton reservoir can be described by a mean-field ring-like trapping potential, which is approximately $1\,\mathrm{meV}$ deep in the center at the pumping power corresponding to the condensation threshold. Un-condensed polaritons start from the blue-shifted states on the ring and ballistically expand [166] either towards the centre or outside. Those which propagate to the centre, eventually collide with each other as well as with excitons (see fig. 4.6). The energy of the ensemble of particles is conserved by these scattering events, so that the kinetic energies of a fraction of the polaritons are reduced, while the rest have their kinetic energies increased. As a result, a fraction of the polariton gas is no more capable to escape from the trap due to the lack of kinetic energy, while the rest can easily propagate over the barriers. Further scatterings of the trapped polaritons lead to the increase of the kinetic energy of some of them so that they become able to leave the trap. By increasing the excitation power, the polariton population inside the trap builds up and a condensate forms at the centre of the ring that is quickly enhanced due to bosonic final state stimulation.

4.3 Comparison with Gaussian excitation

Having demonstrated the build-up of condensation inside this optically induced potential, it is meaningful to investigate whether the resulting condensate has any qualitative differences from typical non-resonant condensates formed by Gaussian spot non-resonant excitation. In a reference experiment we have excited the same sample (at the same detuning, $-4\,\mathrm{meV}$, temperature and pump on:off ratio) with a Gaussian beam with a spot size of FWHM $\sim 5\,\mu\mathrm{m}$. Fig. 4.7 shows the integrated photoluminescence (PL) intensity at $k = 0$ for different excitation powers of the two experiments. Remarkably the condensation threshold power density is found to be more than two times higher in the case of Gaussian excitation. However, in light of the previous discussion concerning the efficient relaxation to the ground state in the previous sections this is not entirely surprising. Furthermore, due to efficient trapping of polaritons in the trap centre the required density for the onset of the stimulated scattering process can be achieved with lower power densities, whereas for spot excitation, diffusion and ballistic ejection of particles away from the pumping region effectively hinders condensation by depleting the coherent state. Arguably the overlap of the condensate wavefunction with the incoherent reservoir can also play an important part regarding the efficiency of particle injection to the coherent state. Therefore, being able to tune this factor can have pronounced effects on the dynamics of the system, as well as in the steady state formation and the modulation

of the density required to reach the onset of coherence (for a more detailed discussion see section 5.2 and section 5.7 in the following chapter). From the description of the condensation process so far, it is evident that condensation will only occur after the trapping potential is deep enough to efficiently contain polaritons. Thus in polariton samples where the exciton-exciton interaction strength is much stronger, i.e. in organic microcavity samples [138], the density required to reach the condensation threshold could be reduced by an even bigger factor than what we observe in our GaAs microcavity sample. The dependence of the condensation threshold to the size of the ring has also been studied (on the same sample) and it has been shown that it is increasing for radii larger than 10μm [167]. Lastly, there could also be some variation of the reduction of the threshold for different exciton-cavity detunings as this changes the exciton fraction of the polaritons which drives bosonic stimulation [168]. In order to quantify the contributions from all these different factors to the threshold reduction a detailed consistent study across different detunings , trap sizes and samples would be required.

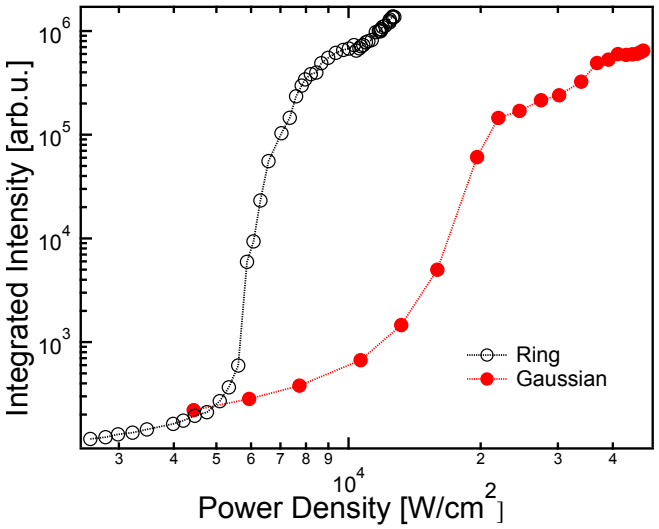

FIGURE 4.7: Integrated intensity with increasing power density from the trapped condensate (open black circles) and from a Gaussian excitation (red circles) measured at $k = 0\,\mu\mathrm{m}^{-1}$ of the spatially filtered dispersions.

Full spatial separation of the condensate from the pump induced excitonic reservoir is also expected to have important implications on the spectral and dynamic properties of polaritons [169] even below threshold. Already in the linear regime the linewidth of the trapped particles in the ground state is almost two times lower ($\sim 250\,\mu$eV) compared to polaritons in the ground state injected by a beam excitation, which interact strongly with excitons from the overlapping reservoir (fig. 4.8a). In the non-linear regime, a clear advantage of the decoupling of the coherent polaritons from the incoherent reservoir is the strong reduction of the depletion processes caused by the condensate-reservoir interactions [170]. Due to the absence of the de-coherence mechanisms instigated by the reservoir, in the case of ring-excitation, the measured linewidth is significantly narrower and close to the resolution limit of

our system. Increase of the density has a negligible effect on the observed linewidth which remains resolution limited even at 2.5 times above the condensation threshold. This behaviour is in stark contrast to the Gaussian excitation condensation. In this case the strong interactions with the un-condensed particles that are present in this configuration have been known to broaden the condensate energy level as the density of the system is raised (fig. 4.8a) red line).

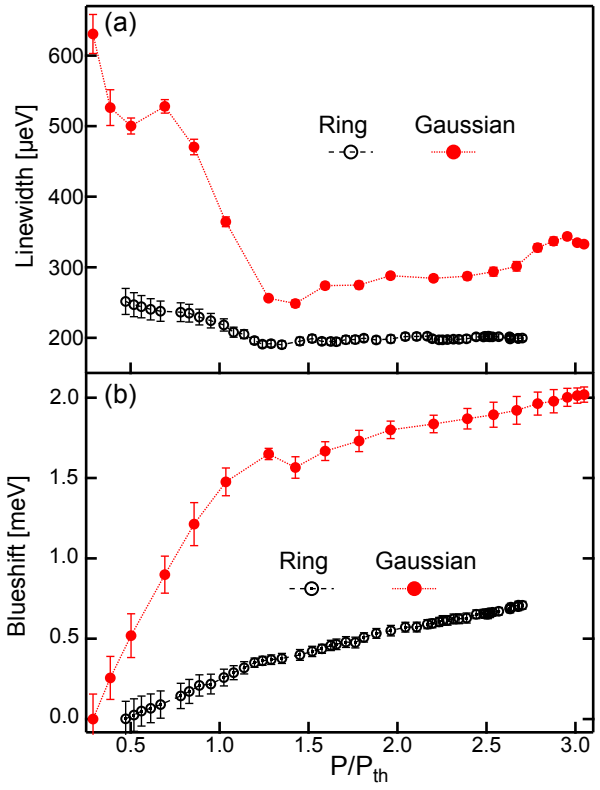

FIGURE 4.8: Linewidth and blue-shift of polaritons from the centre of the ring excitation (open black circles) and from a Gaussian excitation (red circles), measured at $k = 0\,\mu\mathrm{m}^{-1}$ of the spatially filtered dispersions. (a), Linewidth vs excitation power for polaritons at the centre of the ring and a Gaussian excitation. (b) Energy shift of the two condensates vs threshold power. Lines are guides for the eyes.

For the optically trapped polaritons the de-phasing of the condensate due to interaction with the exciton reservoir is strongly suppressed [171]. Thus, above threshold the main mechanism of spectral broadening of the condensate, in the absence of excitons, is governed by polariton-polariton scattering. The linewidth variation of the trapped condensate above threshold is notably small ($\sim 10\,\mu\mathrm{eV}$) evidencing that for the power range and detuning ($-4\,\mathrm{meV}$) that we have examined, the contributions to broadening from polariton self-interactions [172] are negligible. Arguably, this feature is expected to scale with the polariton exciton fraction.

Interactions with the in-coherent reservoir will also affect the energy spectrum of the polaritonic system. The energy shift of the condensate, compared to the unperturbed energy level, increases linearly with the pumping intensity, for the optically

trapped condensate, reflecting a linear increase of the mean number of condensed polaritons fig. 4.8b. In the case of Gaussian excitation, below threshold, the blue shift is strongly affected by the interaction with the reservoir: the increase is four times steeper than in the ring-excitation case while at threshold there is a difference of 1.2 meV. The reduced blue-shift in the centre of the trap, reflects the reduced density of the reservoir around the trapped polaritons. Quantifying the blue-shift as $V_c = n_p V_{pol-pol} + n_r V_{exc-exc}$, where n_p (n_r) is the polariton (reservoir) density, V_{p-p} ($V_{exc-exc}$) the polariton-polariton (exciton-exciton) interaction strength and taking into account that $V_{p-p} \ll V_{exc-exc}$, especially for the negative detuning region of the measurements, it follows that $\frac{V_{cG}}{V_{ctrap}} \approx \frac{n_{rG}}{n_{rtrap}}$ (where n_{rG} (V_{cG}) denotes the reservoir density (condensate energy blue-shift) excited with the Gaussian spot and n_{rtrap} corresponds to the reservoir density at the centre of the trap). Therefore, the ratio between the blue shift of the two cases is approximately equal to the ratio of the exciton density that interacts with each condensate.

4.4 Approaching the Heisenberg limit

In a previous report of polariton condensates in a trap, induced by modulation of the cavity mode by deposition of a thin metal film with an annular hole on the sample surface and excited with a typical Gaussian spot [85], the uncertainty value despite being very close to the Heisenberg limit at threshold (~ 0.98) was reported to quickly diverge to significantly large values, evidencing the disintegration of the robust quantum nature of the condensate. This effect was attributed to the increasing polariton-polariton interactions due to increasing polariton density within the condensate. However it appears much more plausible that interactions between coherent and incoherent particles will have a more significant contribution to the de-phasing of the condensate.

We examine this scenario by performing a real space power-dependence measurement of the real space and energy distribution of the polariton emission, taking extra care to have corresponding power values. Subsequent extraction of Δx,Δk_x and of the corresponding uncertainty principle for every power results in fig. 4.9. We observe that unlike the divergence of Δx observed for increasing density by Utsunomiya et al. [85], in the present experiment the uncertainty over X is relatively stable for a range powers above threshold. Increasing the excitation density results in a deeper potential that more efficiently confines the coherent ensemble of trapped particles (for more on the discussion on increasing excitation density see section 5.3.1). Moreover the uncertainty value for the X direction remains very close to the Heisenberg limit of 0.5 despite some small fluctuations. These observations demonstrate that the inter-condensate scattering events between coherent particles have minimal contribution to de-phasing processes as one would expect

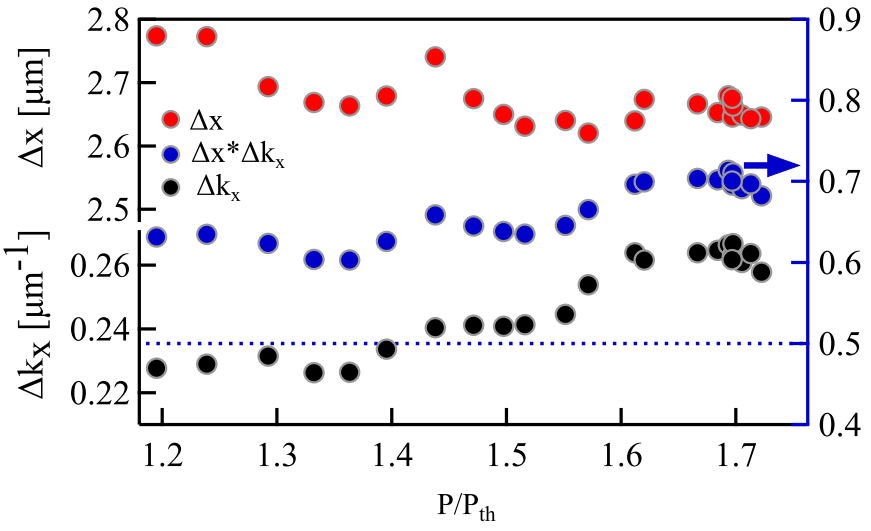

FIGURE 4.9: Position-momentum uncertainty for increasing density

from a coherent state whereas interactions with the incoherent-reservoir have a much more pronounced contribution.

4.5 Conclusion and discussion

In conclusion, we have demonstrated the condensation of a polariton bosonic gas in a two-dimensional optical trap. This configuration allows for the formation of a polariton condensate spatially separated from the excitation area minimizing de-phasing and depletion processes associated with the light imprinted excitonic reservoir. As a result, perturbation of the condensate from incoherent particles is greatly suppressed leading to the lowest reported measurement of the Heisenberg uncertainty for polariton condensates. This highly efficient excitation technique of exciton-polaritons results in the spontaneous formation of a polariton BEC spatially separated from the excitation laser at more than two times lower excitation densities compared to previous experimental configurations. In the case of a polariton BEC formed through optical trapping the linewidth reduces and clamps at threshold clearly evidencing that temporal coherence is not affected by increasing the occupation number of the condensate. Finally, dissociation of the condensate from the excitation beam, conclusively settles the debate on the inheritance of coherence of the polariton condensate from the excitation laser.

Disclaimer:

Part of the results presented within this chapter were published in Physical Review B Rapid communications in 2013

CHAPTER 5

Condensation into Higher Order Modes

Having established the properties of the ground state of the polariton trap, it is purposeful to investigate the effect of the trap size on the resulting condensation mode. We utilise as in the previous chapter a ring-shaped, non-resonant optical excitation scheme to create a size-tunable annular potential trap. Under continuous wave excitation, we study the steady-state regime of trapping and condensate formation. Interestingly increasing the trap diameter results in non-ground state condensation. By controlling the height of the potential trap by tuning the optical excitation density we observe that at coherence threshold, polaritons coalesce preferentially at the uppermost confined energy state that has the largest wavefunction overlap to the exciton reservoir that forms the trap barriers. We observe polaritons condensing in a single pure quantum state rather than condensation into multiple states. To confirm that excited state polariton condensates are realised predominantly by polariton confinement in the optically induced potential trap, we study the transient dynamics of the formation mechanism. For this purpose, we change from continuous wave to pulsed excitation, while keeping all other parameters unaltered, and time-resolve the evolution of the spatial polariton state. Under pulsed excitation, the height of the potential barrier is transiently diminishing following the decay of the exciton reservoir. We observe that the mesoscopic polariton condensate switches between states, progressively transforming to the highest available confined energy state. Finally, the experimental observations are accurately reproduced using an extended Gross-Pitaevski equation.

5.1 Coherent higher order spatial modes in an optical trap

Non-ground state condensates of spatially-confined polaritons were previously observed in optical defect sites and in pillar microcavities, under Gaussian-shaped non-resonant optical excitation incident to the confinement area [157, 174, 175]. While gain competition in thermodynamic equilibrium has been predicted to give rise to occupation of a single or several excited states [176, 177], in both cases, excited state condensates were shown to be driven by the dynamics of energy relaxation across the confined energy states resulting in multi-state condensation. In the case of ring-shaped excitation, two characteristically different regimes of polariton condensates have been realised. For ring radii comparable to the thermal de-Broglie wavelength a phase-locked standing-wave condensate co-localised to the excitation area was observed [178]. For ring radii comparable to the polariton propagation length in the plane of the cavity, the excitation ring acted as a potential barrier and a Gaussian-shaped ground state polariton condensate was realised [179].

Cristofolini and co-workers examined the transition between phase-locked and trapped condensates using multiple-excitation spots and a ring-shaped excitation pattern [167]. Despite earlier work by Manni et al [178], the authors claimed that for ring-shaped pumps, no phase-locked state is geometrically possible. More importantly they have discussed that when the spacing between the pumps reduces (in the transition to the ring shaped pump), the trapped condensate collapses into a Gaussian-shaped ground state. Here, we demonstrate that under ring-shaped excitation, the formation of excited state condensates is driven by polariton confinement in the linear potentials and that the presence of non-ground polariton condensates does not necessitate asymmetries in the shape and/or power distribution of the ring excitation. The dependence of the state selection on the height of the trap's barrier and shape at threshold, provides a robust platform for engineering quantum switches of mesoscopic multi-particle coherent states.

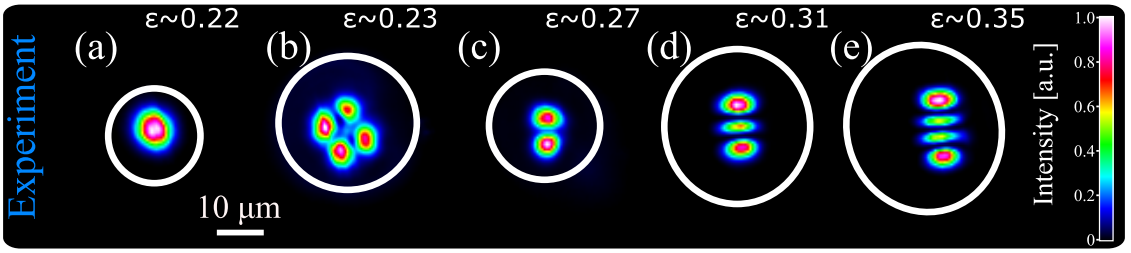

FIGURE 5.1: False color-scale experimental **(a)-(e)** states of polariton condensates. **(a)** Ψ_{00}, **(b)** Ψ_{11}, **(c)** Ψ_{01}, **(d)** Ψ_{02}, **(e)** Ψ_{03}. ϵ denotes the ellipticity of individual configurations.

In the experiment we use the setup described previously for the hollow beam formation (fig. 3.3) with the addition of a variable telescope used to control the radii of the excitation beam, placed between the objective and the collimation lens while the sample is held in the cold finger cryostat at 6 K. We study the steady-state dynamics under non-resonant excitation at 752 nm using a single mode quasi-continuous wave (CW) laser (2% on-off ratio at 10kHz).

Figures 5.1a-e, show the spatial profile of mesoscopic wavefunctions for a range of excitation radii and asymmetries, characterised by the ellipticity and radius of the excitation ring, at the coherence threshold that defines the depth of the trap via the interactions in the reservoir. Theses states resemble the TEM modes of a harmonic oscillator and we will adapt this symbolism to annotate the state of the coherent polariton wavefunction for the rest of our analysis. For an excitation ring with a radius of $\sim$10 μm we observe a ground-state polariton condensate (fig. 5.1a), as described in the previous chapter, which remains in the ground-state as long as the long axis of the asymmetric excitation does not exceed $\sim$10 μm. For larger excitation ring radius ($\sim$17 μm) and similar ellipticity as in fig. 5.1a ($\epsilon = 0.22$) at coherence threshold we observe that polaritons coalesce at a higher symmetric excited state (ψ_{11}) as shown in fig. 5.1b. We note that the symmetry of the excited state wavefunction is robust to small asymmetries (ellipticity) in the excitation ring ($0 < \epsilon < 0.23$) and the transition from ground to non-ground polariton condensates is predominantly dependent on the radius of the ring. With increasing the ring radius and the asymmetry of the excitation it is possible to observe excited state polariton condensates as shown in fig. 5.1c-e. On top of each panel we have annotated the ellipticity of the excitation ring.

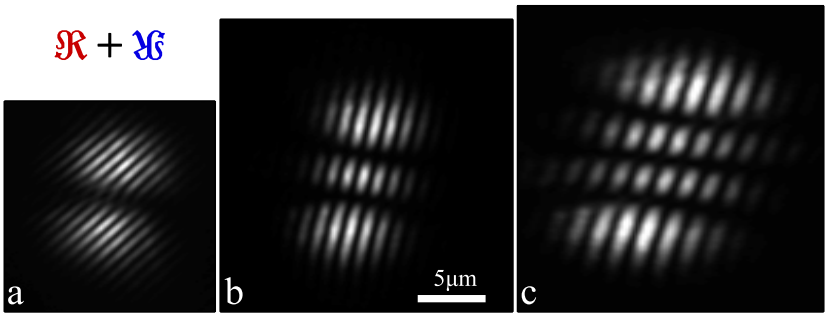

FIGURE 5.2: Interference patterns of trapped polariton condensates: a) Ψ_{01}, **b)** Ψ_{02}, **c)** Ψ_{03}. The interference patterns where obtained with a retro-reflector configuration.

To confirm that these are indeed coherent mesoscopic wavefunctions of extended condensates we perform interferometric measurements with the stabilised Michelson interferometer setup (see section 3.4). The interferograms of modes $\psi_{01}, \psi_{02}, \psi_{03}$ are presented in fig. 5.2a-c. It is worth noting that the real space image is inverted

in a centro-symmetric way (see the inset in fig. 5.2) in one of the arms of the interferometer so that, for instance in fig. 5.2a the top lobe is interfered with the bottom one.

We extract the phase and amplitude of the recorded interference patterns with the use of a digital holographic technique [136, 164]. This process reveals that the phase is smoothly varying along the surface of the condensate bound state (fig. 5.3a,b,c) while the relative amplitudes extracted from the interferograms again displays a well defined high contrast state.

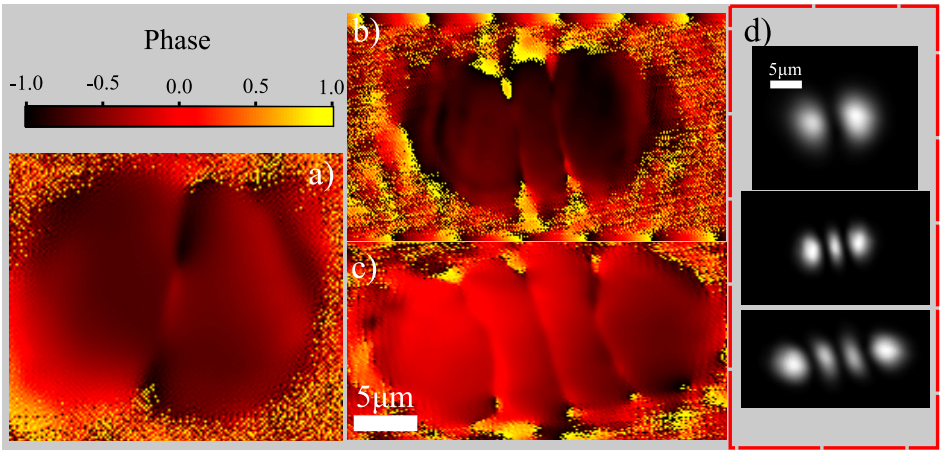

FIGURE 5.3: Phase and amplitude of excited state polariton condensates extracted form the inteferograms of fig. 5.2. a), b) and c) are the extracted phase patterns of Ψ_{01}, Ψ_{02} and Ψ_{03} respectively. In d) the corresponding amplitudes of the modes extracted from the interferograms are displayed.

Interestingly, multi-state condensation is not observed contrary to previous non-optical trapping schemes. The most prominent difference with condensation into non-optical potentials is that the condensate is populated from the trap barriers were carriers are originally formed rather than a trap-overlapping reservoir as in defect [157] and stress traps [73, 150]. Moreover the selectivity of the mode is observed to be driven by the geometry of the trap. This leads to the supposition that the driving mechanism of the mode selectivity is the overlap of the condensate wavefunction with the incoherent "feeding" reservoir. Higher order bound states are by definition more spatially expanded, will have a larger component overlapping with the spatial profile of the reservoir, be more efficiently populated and will therefore reach the stimulation threshold for lower excitation densities. Above threshold stimulated processes will exponentially enhance the density of this state while diminishing the feeding processes to the lower states.

5.2 Simple one-dimensional trap model

It is straightforward to implement a one dimensional model of the trap and numerically solve the 1D Schrödinger equation for the experimentally calculated polariton mass. The 1D profile of the trap can be reasonably approximated by 2 Gaussian beams at a distance equal to the diameter of the trap. Increasing the radius of the trap inevitably modulates the energy levels of the available trapped states. Intuitively for large trap sizes the bound states closely match those of a square well potential while for smaller optical traps the trap profile is increasingly parabolic. Setting a constant barrier height we calculate the energy levels inside this 1D trap for increasing trap radius. Figure 5.4a shows the results of this calculation where the lines are colour-coded for each trap size. Under the simplification that the barrier height (blue-shift) would remain constant it is evident that the highest energy level, where we expect condensation to occur, doesn't have a monotonic dependence on the size of the trap. As expected the smaller sizes display a linear energy dispersion (indicative of the parabolic potential) while the larger ones have an increasingly parabolic one as the system tends to resemble more a finite square potential.

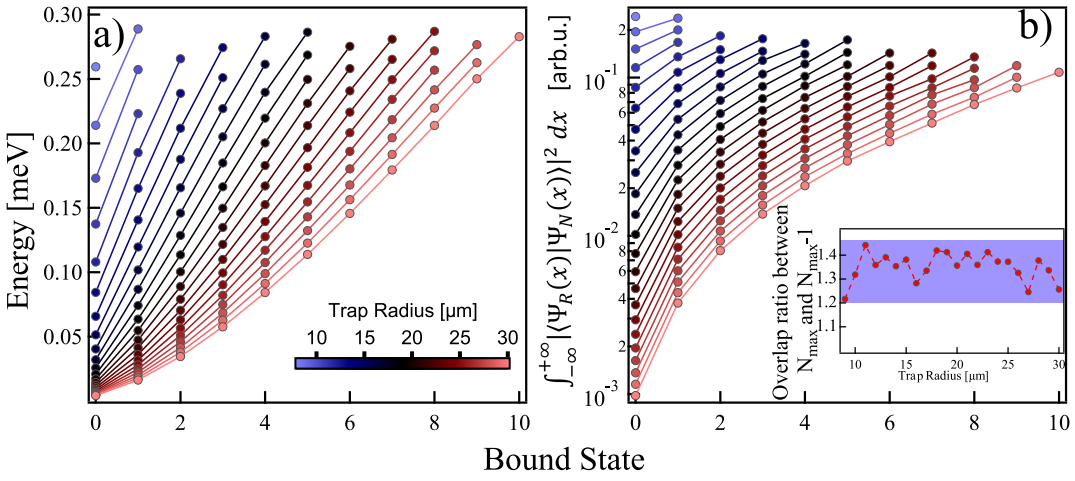

FIGURE 5.4: Energy levels and corresponding wavefunction reservoir overlap for increasing trap radii. a) Calculated energy levels for increasing trap radius for a trap depth of 0.3 meV from a 1D numerical simulation, b) Corresponding calculated overlap of bound states with the reservoir. Inset in b), overlap ratio of N=max and N=max-1 states vs trap radius.

Intuitively the overlap of the bound wavefunctions is greater for the higher order modes for each trap configuration. Nonetheless this should be explicitly demonstrated. Quantifying the overlap of the wavefunction with the reservoir as the integral of $\|\langle \Psi_N(x) | \Psi_R(x) \rangle|^2$ we are able to compare the overlap of the calculated energy levels of fig. 5.4a. Figure 5.4b graphically depicts this calculation for each

trap configuration (radius), showing that indeed the overlap follows a monotonic dependence for increasing N[1].

5.3 Mode switching

This straight-forward interpretation/hypothesis concerning the mode selectivity can be easily tested, both in the dynamic equilibrium regime and the transient domain. Increase of the trapping barrier height, by increasing the reservoir density should eventually lead to a spontaneous mode transition when the trap becomes deep enough to accommodate an additional energy level. For the continuous wave excitation experiment we initialise the system in the Ψ_{04} state as the energy spacing of larger traps is expected to be considerably less and therefore more likely that the expected transition will take place within the power range available in our excitation setup. In the transient domain, where the potential is formed with a femtosecond optical pulse we expect to witness the reverse process as the barriers gradually decay.

5.3.1 Steady state switching by modulation of the barrier height

We investigate the dependence of the quantum state selectivity on the barrier height by varying the non-resonant excitation density of a geometrically fixed, ring-shaped, excitation profile. We use an excitation ring of radius $\sim$16 μm and $\epsilon = 0.27$ that at coherence threshold produces the Ψ_{04} polariton state as shown in fig. 5.5a. By increasing the excitation density above the coherence threshold, while keeping all other parameters the same, we observe the transition from Ψ_{04} to Ψ_{05} (fig. 5.5b) at approximately 1.12 P_{th}. The order of the latter state is clearly revealed in fig. 5.5c, where we plot the normalised spatial profiles along the white dashed lines of the real space intensity images of fig. 5.5a,b. Fig. 5.5c shows the presence of an extra node at the higher excitation density indicative of Ψ_{05}.

Additionally, we perform a similar energy resolved power dependence experiment with the same parameters. Upon activation of the transition to the next state, we expect to observe a sharp energy jump of the energy spectrum of the condensate. In fig. 5.5d we plot the energy shift of the condensate in the transition from Ψ_{04} to Ψ_{05} with respect to its energy at threshold ($\Delta(E_P - E_{P_{th}})$). An increase of the energy shift ($\sim 45\mu eV$) is observed in fig. 5.5d at $P \sim 1.12 P_{th}$. Although the resolution of our spectrometer is approximately $170\mu eV$ we can still differentiate between individually measured peaks by Gaussian fitting of the extracted profiles as shown clearly

[1]For the one dimensional numerical model we used $t_{dec} = 200ps$ for the reservoir decay, $V_0 = 0.3meV$ for a potential consisting of two Gaussian barriers with FWHM of $7\mu m$ separated by 2*radius

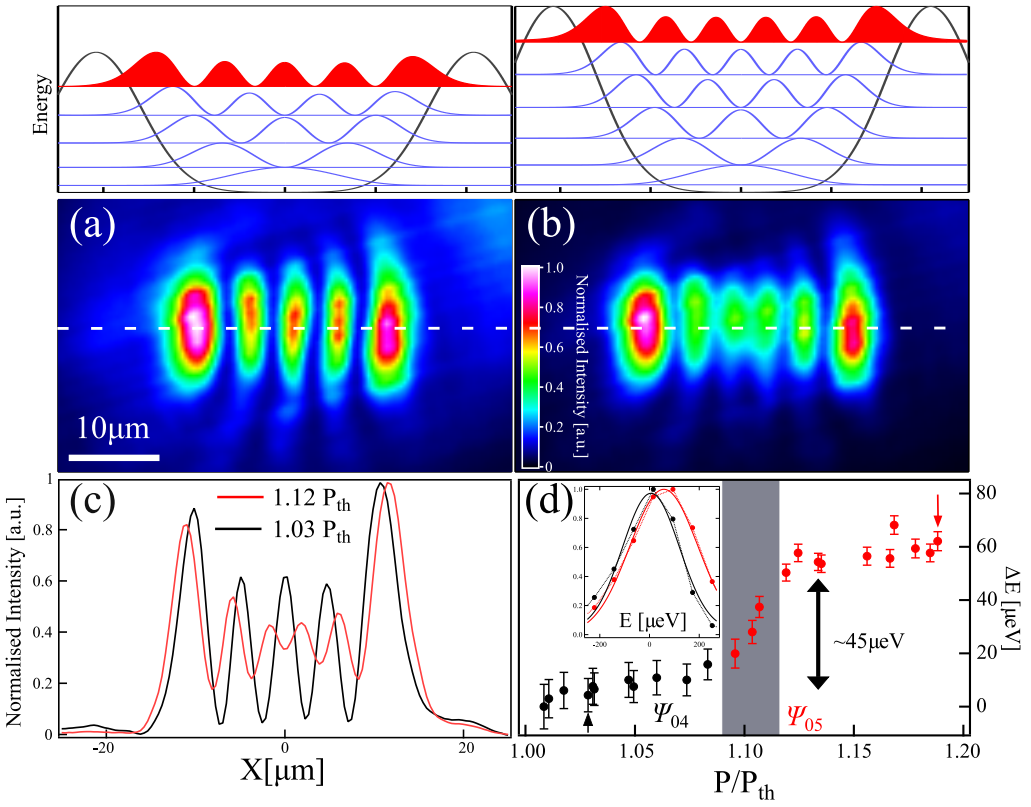

FIGURE 5.5: Evolution of Ψ_{04} for increasing excitation density. Bottom panel: **(a)** Ψ_{04} at P=1.03P_{th}. **(b)** Subsequent increase of the power results in the appearance of Ψ_{05} at P=1.12P_{th}. Top panel: Schematic representation of the confined energy states for two different barrier heights. **(c)** Profiles of the wavefunction for different excitation densities extracted along the dashed white lines at **(a)** and **(b)**. **(d)** Corresponding energy difference with respect to the energy at coherence threshold for increasing excitation power normalised at the coherence threshold power P_{th}. Inset in **(d)** shows the spectra of the points denoted by the arrows

in the inset of 5.5d. However the energy transition is not as sharp as theoretically expected. Nevertheless, taking into account the intensity fluctuations of the excitation beam during the acquisition time of the measurements can artificially blur the two states. The top panels in fig. 5.5a,b depict the calculated energy levels for the trap shape and the corresponding probability density of the confined states. In both panels, the red-filled probability density corresponds to the occupied state. It is worth noting here the greater overlap of the probability density of the highest energy level (Ψ_{04} in fig. 5.5a and Ψ_{05} fig. 5.5b) with the reservoir compared to the lowest energy levels. Evidently, with increasing the barrier height a polariton condensate is realised at the next confined energy level as a pure-quantum-state that can be singularly described by the principal quantum number n ($\Psi_{0,n}$).

It is worth pointing out the remarkable quantitative agreement of the 1D model, regarding the energy difference of the fourth and fifth excited states for a trap radius of the order of $\sim 20\mu m$ in fig. 5.4, with the experimentally measured value of $\approx 45\mu eV$.

5.3.2 Dynamic mode switching

We further explore the robustness of the formation of the observed pure-quantum-states on density fluctuations in the exciton reservoir by extending our study from the excitation density dependent switching between successive states in the dynamic equilibrium regime to transitions in the time domain under non-resonant pulsed excitation. We use a ring-shaped non-resonant 200 femtosecond pulse at 755 nm with $\sim 11\mu$m radius of the major axis and $\epsilon = 0.3$ at $\sim 1.6 P_{th}$. To resolve the spatio-temporal dynamics of the emission we employ the real space-transient tomographic setup as described in section 3.2.4 and then reconstruct the real space images for each pixel of the time axis of the streak.

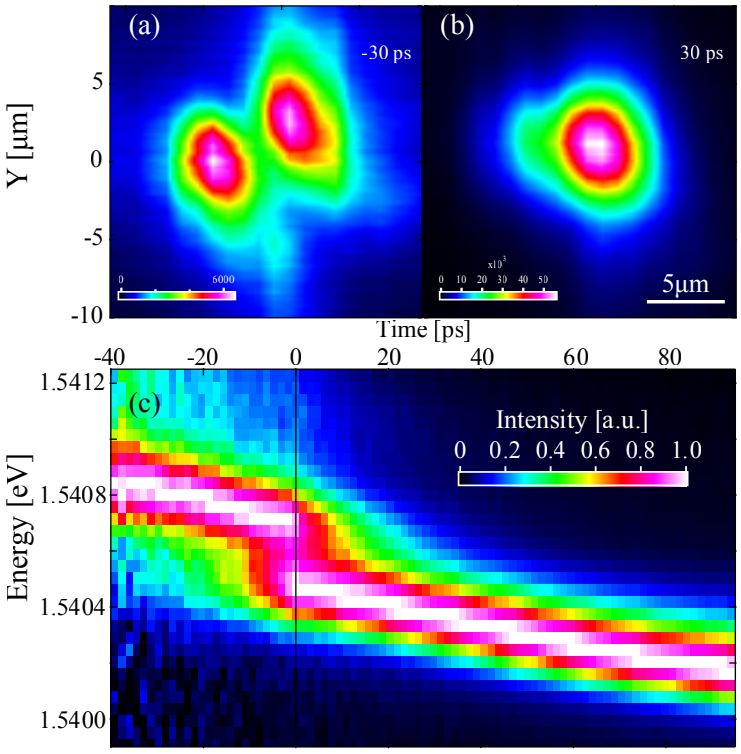

FIGURE 5.6: **False color-scale real space tomographic frames in the time domain. (a)** $\Psi 01$ state at -30ps and **(b)** subsequent transition to Ψ_{00} at 30ps. **(c)**Intensity normalised time evolution of the emission energy over $|k| \leq 1.4\mu$m.

For early times we observe the formation initially of the Ψ_{01} polariton state and its subsequent transition to Ψ_{00}. We set the transition point to define the zero time frame for the rest of our analysis. Figure 5.6a shows a snapshot of the Ψ_{01} state at -30 ps. At later times, the two lobes of the Ψ_{01} state drift closer together and the condensate rapidly transforms to the ground polariton state (Ψ_{00}) of fig. 5.6b. The decrease of the density in the barriers in the time-domain results in a shallower trap in which the Ψ_{01} state is no longer confined, leading to the formation of a polariton condensate at the next available state, here the ground state Ψ_{00}, while the emission from the Ψ_{01} mode quickly decays with the polariton decay rate.

In order to visualise the energy jump of the emission at the transition point, we time resolve the full dynamics of the dispersion with our tomography streak setup. From the time-resolved dispersion, we extract the profiles for each time "frame" along the energy axis, integrated over an angular width corresponding to $|k| \leq 1.4\mu$m. The normalised (for clarity) profiles are assembled in fig. 5.6c, where we observe a sharp energy jump upon the transition from Ψ_{01} to Ψ_{00}. The energy resolution of our system however limits us in this case from extracting a precise measurement of the energy jump at zero time when the intensity of the two modes is comparable. It is also worth noting that intensity normalisation at every time-frame gives the artificial impression that energy-time uncertainty is violated. This dynamic transition further illustrates that under optical confinement a polariton condensate spontaneously occurs at the higher confined state as defined by the barrier height of the trap and that the transition to the ground state is hindered solely by the existence of higher energy levels that are more efficiently populated.

5.4 Theoretical treatment with a dissipative Gross-Pitaevski model

The optical confined condensate can be theoretically modelled with a non-linear Schrödinger equation, namely the Gross-Pitaevski equation. Simulations with the Gross-Pitaevski equation with a potential similar to the one from the experimental measurements in our system qualitatively reproduce the states recorded experimentally. Using a potential $V(r)$ that consists of the exciton-exciton interactions in the reservoir, that blue-shift the polariton energy levels at the barriers, and of the polariton-polariton interactions in the condensate,the Hamiltonian of the system can be summarised to:

$$H(r) = T + V(r) \tag{5.1}$$

$$V(r) = V_r(r) + V_c(r) \tag{5.2}$$

$$V_r(r) = N_r U_{ex-ex} f_r(r) \tag{5.3}$$

$$V_c(r) = U_{pol-pol} \Psi_c(r) \tag{5.4}$$

where N_r is the density of excitons in the reservoir, N_c the condensate density, U_{ex-ex} the exciton-exciton interaction strength, $U_{pol-pol}$ the polariton-polariton interaction strength and $f_r(x)$ is the spatial distribution of the exciton reservoir taking into account exciton diffusion. $V_c(r)$ represents the energy shift caused by inter-particle interactions in the condensate. In addition to kinetic and potential energy terms in the above Hamiltonian, to account for polariton spatial dynamics, a generalisation of the extended Gross-Pitaevski equation is required to include incoherent

pumping and decay [180]. In continuous wave experiments one expects the excitation of a steady state of hot excitons with the spatial profile set by the optical pumping extended by exciton diffusion. One can then make use of the Landau-Ginzburg approach for describing the dynamics of the 2D polariton wavefunction [89]:

$$i\hbar\frac{d\psi(\mathbf{r},t)}{dt} = \left[-\frac{\hbar^2\hat{\nabla}^2}{2m_p} + (U_{pol-pol} - i\Gamma_{\mathrm{NL}})\,|\psi(\mathbf{r},t)|^2 + (U_{pol-ex} + ir)\,N_r f_r(\mathbf{r}) - \frac{i\Gamma}{2}\right]\psi(\mathbf{r},t) + i\hbar\Re\left[\psi(\mathbf{r},t)\right] \tag{5.5}$$

where m_p is the polariton effective mass and $f_r(\mathbf{r})$ describes the 2D spatial distribution of N_r excitons. The condensation rate r describes the gain of polaritons in the presence of the exciton reservoir. The polaritons experience both a linear decay Γ and non-linear loss Γ_{NL}, which represents the scattering of polaritons out of the condensate when its density is high [89]. The final term in eq. 5.5 represents a phenomenological energy relaxation [181] in the system, which can play an important role when non-ground state polaritons interact with a potential gradient [81, 159, 182]:

$$\Re[\psi(\mathbf{r},t)] = -\lambda N_r f_r(\mathbf{r})\left(\hat{E}_{\mathrm{LP}} - \mu(\mathbf{r},t)\right)\psi(\mathbf{r},t) \tag{5.6}$$

Kinetic energy relaxation of this form was derived with a variety of methods [183, 184] and offers a simple model for the qualitative description of our experiments. We note however that this model does not distinguish between different mechanisms of energy relaxation, which may have different power dependences [185].

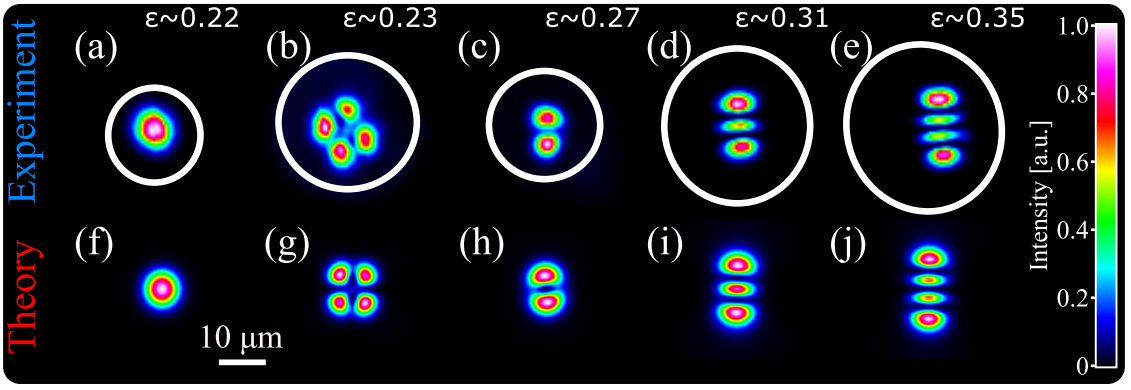

FIGURE 5.7: False color-scale experimental **(a)-(e)** and theoretical **(f)-(j)** states of polariton condensates. **(a),(f)** Ψ_{00}, **(b),(g)** Ψ_{11}, **(c),(h)** Ψ_{01}, **(d),(i)** Ψ_{02}, **(e),(j)** Ψ_{03}. ϵ denotes the ellipticity of individual configurations.

Fixing $N_r f_r(\mathbf{r})$ to represent a ring shaped excitation (with slight asymmetry), the numerical solution of eq. 5.5 gives the steady state intensity profiles shown in fig. 5.7f-j. Different configurations are accessed by varying the spatial distribution ($f_r(\mathbf{r})$)

and population of hot excitons (N_r) , as in the experiment[2].

5.5 Higher order assymetric modes

Apart from the modes presented so far, there is a plethora of extended modes observed for greater trap sizes (radius>15μm) fig. 5.8. With the "analog" experimental configuration we employed for the spatial shaping of the beam, it was increasingly more difficult to achieve a fully symmetric (i.e circular or elliptical with small ellipticity) trap configuration. Moreover as the trap radius is increased the number of modes that it can accommodate (for similar barrier height) increases and these higher order multi-lobed modes are more sensitive to the asymmetries in the trap profile. Nevertheless, they still share the common characteristics of the modes examined previously: they are observed above some condensation threshold, they occupy a single energy level and have spatial coherence. The most extended mode that we were able to observe, within the power range available in our experimental setup, on the high Q microcavity sample that we studied corresponded to a trap size with a radius of approximately 35μm and the condensate extended over an area of $\approx 3000\mu$ m^2 fig. 5.8f). Recently, it has been reported that on a new state of the art GaAs microcavity sample with a Q factor of more than 300000 and thus increased polariton lifetime [186], condensation has been observed in a trap with a diameter of 85μm [173]. In this sample, where polaritons can propagate for hundreds of mi-

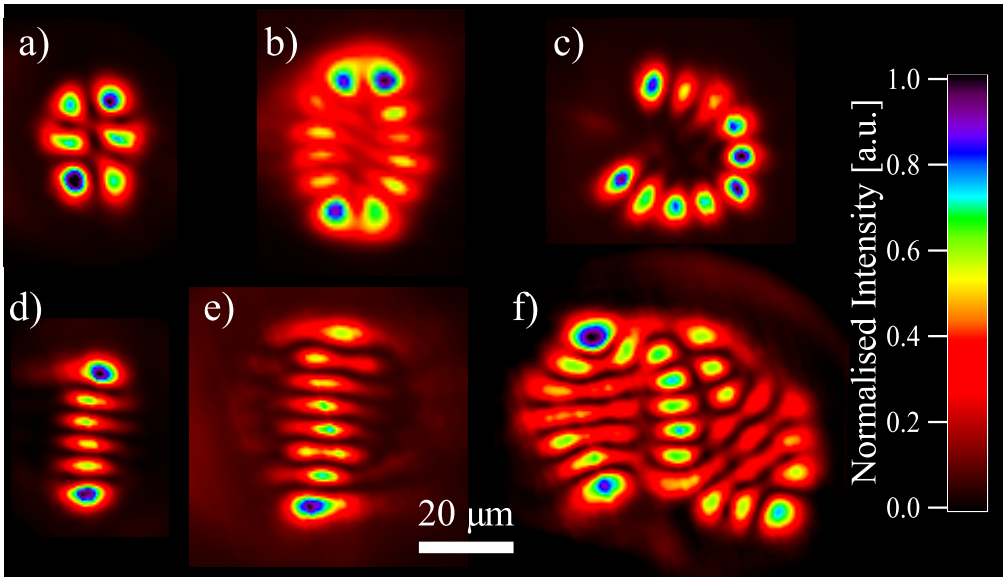

FIGURE 5.8: Higher order modes of the optical trap. a) Ψ_{12}, b) Ψ_{15}, c) petal shaped mode with 10 lobes, d) Ψ_{05}, e) highly asymmetric 10 lobe mode, f) extended asymmetric mode with 30 lobes covering approximately 3000μm^2

[2]The following parameters were used in the simulations of the experiment our system: $m_P = 7 \times 10^{-5} m_e$, $U_{pol-pol} = 2.4 \times 10^{-3}$ meVμm^2, $U_{pol-ex} = 2U_{pol-pol}$, $\Gamma_{\rm NL} = 0.3U_{pol-pol}$ [89], $r = 6 \times 10^{-4}$meVμm^2, $\lambda = 1.2 \times 10^{-3}\mu$m^{2}ps^{-1}meV^{-1}, $\hbar/\Gamma = 5$ps (also see Appendix A).

crometers [186, 187] it is conceivable that polariton condensation into traps with a radius greater than 100μm can be observed.

5.6 Dispersion dynamics and dynamic tunnelling

The examination of the transient dispersion time-frames from which the evolution of the condensate mode energy has been extracted can further underline and clarify the dynamics of the condensate within the optical potential. In fig. 5.9, three characteristic snapshots of the dispersion evolution are presented. Fig. 5.9a corresponds to the Ψ_{01} state 30 ps prior to the onset of the transition and features a non-zero momentum distribution. The two centro-symmetric lobes observed along the k_x axis are in fact the two counter-propagating components of the coherent standing wave of this mode [188]. At 0ps (fig. 5.9b), Ψ_{01} starts diminishing in intensity while the Ψ_{00} energy level ignites as particles from the reservoir coalesce at this energy as previously discussed, while fig. 5.9c displays the momentum distribution of the system 30 ps after the transition. Extracting the energy profile along the white dotted lines of fig. 5.9a for the entire experimental time range, while intensity normalizing for every frame yields fig. 5.6c.

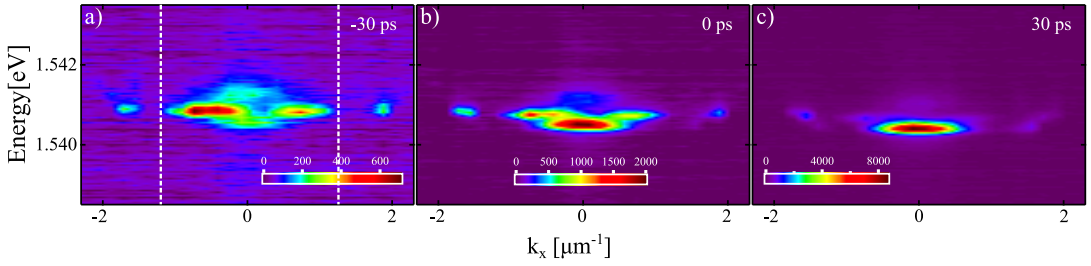

FIGURE 5.9: Transition dispersion dynamics. False colour-scale dispersion images for t=-30 ps (a), t=0ps (b) and t=30ps (c)

As the barrier dynamically decays and the Ψ_{00} mode is switched on as previously discussed, it quickly overtakes Ψ_{01} in intensity at $\sim$0ps. The first excited state quickly dissipates after this point with the polariton lifetime and the dispersion is dominated by the emission of the trap ground state. Interestingly, figures 5.9a-c also reveal distinct satellite modes at the same energy of the confined modes but for greater in plane wave-vector. For quantum states in traps with a finite barrier width (see fig. 5.10a), coherent tunnelling modes are a characteristic feature. Moreover, in our system these modes will be accelerated by the potential landscape outside the trap eventually acquiring momentum characteristic of the difference between the energy level in the trap and of the unperturbed polariton dispersion of the system outside the excitation region (fig. 5.10a). From this description it becomes clear that the tunnelling modes are expected to be at the same energy but with higher momentum, as observed in fig. 5.9a-c.

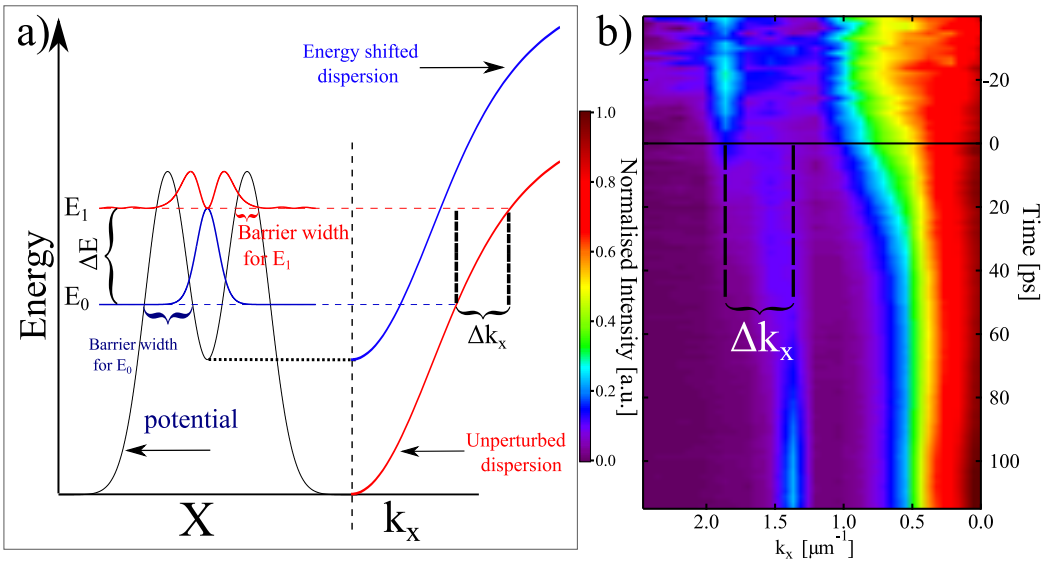

FIGURE 5.10: a) Schematic representation of the momentum acquired by polaritons tunnelling outside of the potential trap (potential and dispersion energy not in scale). b) Intensity normalised time evolution of k_x showing the characteristic Δk_x jump of the tunnelling mode.

.

Integrating the time-dispersion images over energy, while intensity normalising for every time frame, we compile the time evolution of k_x (fig. 5.10b). This analysis reveals the expected Δk_x difference of the tunnelling modes of the two states. Intuitively, the relative (to the trapped state) intensity of the Ψ_{01} tunnelling mode at the transition is substantial, as the width of the barrier goes to zero at this energy level, in contrast to the tunnelling amplitude of the ground state that is effectively suppressed as the potential width at the Ψ_{00} energy level is still significant. Nevertheless, following the dynamic dissipation of the barrier, due to the decay of particles as well as draining of the reservoir by the condensate, we observe a continuous increase of the relative intensity of the tunnelling amplitude of the ground state at $k_x \sim 1.4\mu m^{-1}$. Indeed as exemplified by fig. 5.11a the intensity ratio of the satellite mode relative to the ground state intensity exponentially increases toward unity. The observation of the satellite to condensate ratio close to unity signals the collapse of the trapping efficiency and that the coherent mode is no longer effectively confined.

We further examine this behaviour with our 1D model, by simulating a trap with similar geometric properties imposing an exponential decay of the trapping potential with decay constant $\tau = 200ps$ and monitor the energy level of the ground state of the trap and the relative barrier width at this energy level. Fig. 5.11b displays the time evolution of the energy level of the ground state along with the energy of the top of the barrier of the trap (in logarithmic scale, left axis) and of the barrier width at the ground state energy (in linear scale, right axis). We find that for an exponential decay of the trap potential, the barrier width of the ground state decays

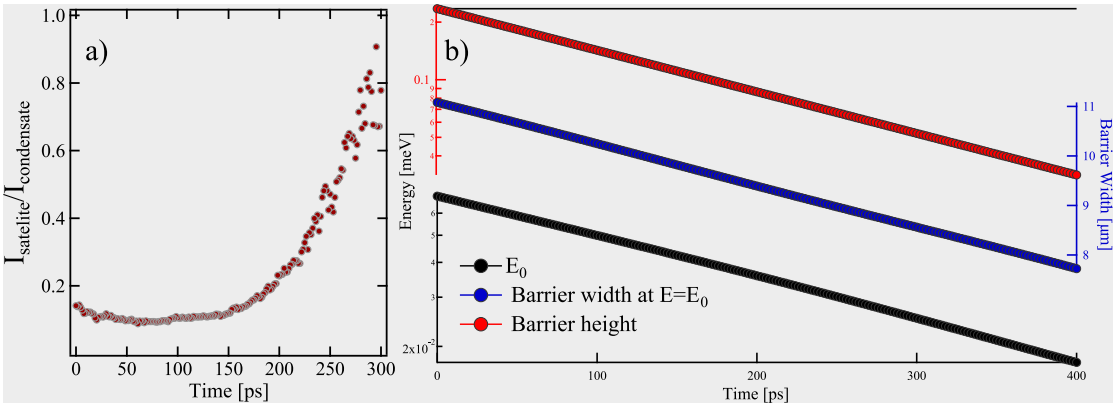

FIGURE 5.11: a) Experimental evolution of tunnelling-condensate intensity ratio over time. b) Simulated dynamics of barrier height (red dots, left axis), ground state energy level E_0 (black dots, left axis) and calculated width of the trap barrier at the level of E_0 (blue dots, right axis)

linearly. Indeed a linear decay of the confining barrier would facilitate an exponential increase of the coherent tunnelling as observed in the experiment (fig. 5.11a).

5.7 Effect of the reservoir condensate overlap on the transient dynamics of the system

In section 5.2 it was demonstrated that bound states have substantially different overlap with the trapping potential. Indeed this value was calculated from the one-dimensional model to range for over two orders of magnitude for the trapped modes of the bigger ($r = 24\mu m$) trap sizes. Under a Gaussian excitation scheme the overlap of the condensate with the feeding reservoir is expected to be close to unity, much greater than what was calculated in fig. 5.4b for any trapped state. It is easy to see that when the condensate-reservoir overlap is greater the population of the reservoir will be depleted faster through increased scattering of particles to the condensate. Similarly, when condensate and reservoir are spatially de-localised, the drain of particles from the reservoir will be strongly suppressed and the dynamic behaviour of the coherent state will be much slower. To further quantify this discussion we can construct a coupled rate equation model for the condensate and reservoir populations. For a detailed description, one has to take into account the spatial characteristics of the system and also incorporate the slow diffusion kinetics of the reservoir. However, since the reservoir kinetics are much slower than the characteristic decay times, for a first order approximation we can neglect them and

encode the spatial dependence of the system in the condensation rate R.

$$\frac{dN_r(t)}{dt} = -RN_r(t) - \frac{N_r(t)}{\tau_r} + P(t) \tag{5.7a}$$

$$\frac{dN_c(t)}{dt} = RN_r(t) - \frac{N_c(t)}{\tau_c} \tag{5.7b}$$

$$P(t) = \frac{N_0}{t_w\sqrt{\pi}} e^{-\left(\frac{t-t_0}{\sqrt{2}t_w}\right)^2} \tag{5.7c}$$

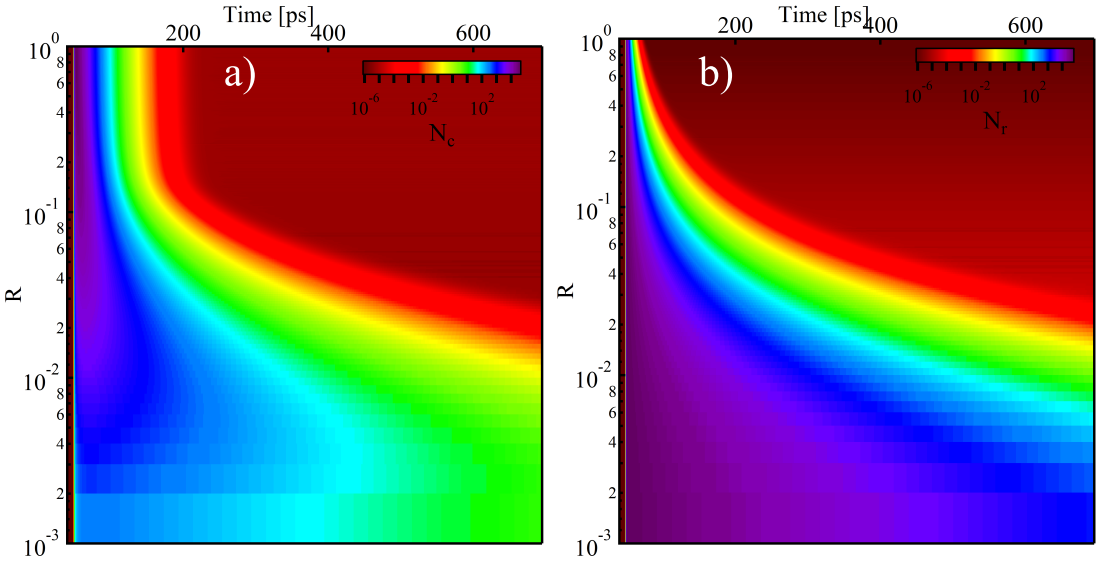

FIGURE 5.12: Simulated condensate (a) and reservoir (b) population dynamics for varying condensation rate R.

In eq. 5.7a,b N_r and N_c are the population of the reservoir and of the condensate respectively, $\tau_r = 200ps$ and $\tau_c = 7ps$ are the reservoir and condensate decay rates respectively, while eq. 5.7c represents the initial excitation of a population N_0 in the reservoir by the laser pulse, where $t_w = 500fs$ is the pulse width and $t_0 = 50ps$ the pulse arrival time. As mentioned before R is the condensation rate, describing particles scattering into the coherent quantum state, and will be proportional to the condensate reservoir overlap $R \propto |\langle\Psi_c|\Psi_r\rangle|^2$. In order to examine the effect of varying R on the transient dynamics of the system we set the proportionality constant to 1 (in ps^{-1}) for the rest of this analysis. We then proceed to numerically solve eq. 5.7 for a range of values of R.

The results for varying R from $10^{-3}ps^{-1}$ to $1ps^{-1}$, for an initial pulsed induced population $N_0 = 10^5$ are presented in Fig. 5.12a,b. As expected the condensate dynamics are radically affected by a change of R. The relevant time parameters extracted from the simulation are presented in fig. 5.13a. The time it takes for the condensate to reach peak population, after the arrival of the pulse (at $t_0 = 50ps$, brown dotted line in fig. 5.13a), is shown to increase with reducing R, while

as R approaches unity (in ps^{-1}) it asymptotically approaches the pulse arrival time ($t_0 = 50ps$) (fig. 5.13a red line and dots). Similarly, the time that is required for the condensate density to fall to half its peak density, or the half-life of the condensate ($t_{1/2}$), is found to be substantially increased for low values of R, despite the very fast decay ($t_c = 7ps$) of polaritons (fig. 5.13a blue dots). Nonetheless, for increasing R, $t_{1/2}$ approaches the limit of $ln(2)t_c$ (dotted blue line) that is the time required for the population of a system with lifetime t_c to decay to half its initial density. A collateral effect of the decrease of the condensation rate, is that the peak population of the condensate (N_{max}) will also be strongly affected as shown in fig. 5.13b . This is due to the fact that for a slower condensation rate, a number of particles in the reservoir will decay before they have the chance to scatter into the condensate. Additionally, as was described previously, a smaller R also results in the peak density of the condensate (N_{max}) being reached later in time ($t(N_c = N_{max})$, fig. 5.13a), which in turn allows for a number of particles from the condensate to quickly decay (with the polariton decay rate t_c) and thus reduce the maximum intensity of the system.

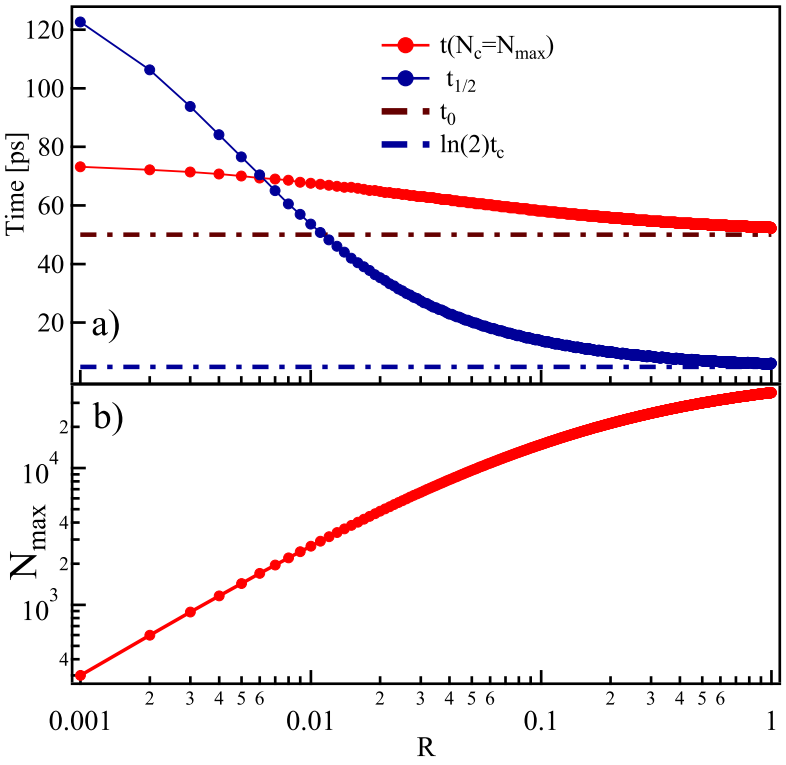

FIGURE 5.13: Calculated condensate half life $t_{1/2}$ and time of peak density $t(N_c = N_{max})$ a) and maximum population b) for the simulations of fig. 5.12

It is worth pointing out that modulation of the rate of condensation by an order of magnitude for the lowest simulated values, from $R = 0.01ps^{-1}$ to $R = 0.001ps^{-1}$ yields more than a two-fold increase of the condensate half-life. Taking into account that the condensate-reservoir overlap has been found to be strongly modulated with increasing trap size it is reasonable to assume that the condensate lifetimes of

the extended modes that we have experimentally observed will also be strongly affected.

Although, the coupled rate equation model of eq. 5.7 can serve as a good first order approximation in order to examine the dependence of the system dynamics on the condensation rate R, it nonetheless has some inherent limitations. The stimulated scattering process is enhanced by the presence of a population of particles in the condensate, therefore realistically R will depend also on the density of the condensate for low densities of N_c. Moreover, this description is effectively that of a two level system neglecting the continuum of polaritonic states. However, the qualitative features presented here can provide a valuable insight for the much more complex dynamics of optically confined polariton condensates.

5.8 Conclusion

In conclusion, we have investigated the dynamics of polariton condensates under optical confinement and observed that, in contrast to previously reported excited state condensation in defect traps and pillar structures, the injection of polaritons from the trap barriers leads to the preferential population of a single bound state, which upon reaching coherence threshold manifests itself as a pure-quantum-state with a mesoscopic coherent wavefunction. We have investigated the state selectivity of this system on the geometric properties of the trap and have demonstrated a highly controllable switching between successive mesoscopic coherent quantum states, in the dynamic equilibrium regime and in the time domain. These results demonstrate the capability of tailoring and manipulating on-chip pure-quantum-states in semiconductor microcavities. Taking into account that the extensive propagation and malleability of the polaritonic flow has been widely demonstrated, optically confined polariton condensates emerge as a promising platform for applications such as many-body quantum circuitry and continuous-variable quantum processing.

Disclaimer:

Part of the results presented within this chapter were published in Physical Review B in 2015. The simulations and theoretical modelling presented in section 5.4 were performed by Tim C.H. Liew.

CHAPTER 6

Optical Manipulation of Condensate Spin Imbalance

Implementation of all optical, integratable spin-polarisation switching devices is one of the essential ingredients for the realisation of novel solid state optoelectronic spin-logic architectures [27]. Semiconductor microcavities operating in the strong coupling regime, have recently emerged as ideal systems towards this end due to their inherent spin multi-stabilities [29, 189] and fast spin dynamics [190–194] that arise from their strong optical non-linearities [13]. As previously discussed (see section 1.3), exciton-polaritons, inherit the spin properties from their excitonic and photonic components while their decay gives rise to photons with a polarization defined by the polariton spin. This robust spin to photon polarization conversion is favourable for fast non-destructive readout of the spin state of the system. The advancement of fabrication techniques has yielded microcavity structures of high finesse featuring polariton lifetimes of the order of 10 picoseconds enabling the emergence of optically excited polariton lasing and condensation [137, 139] even at room temperature [21]. In state of the art microcavity structures, polariton condensates propagate ballistically [166] and this has enabled the first demonstrations of polariton condensate optical switches [158, 195, 196].

Initial realizations of resonant polariton spin-switches [197], followed by experimental demonstrations of extensive polariton spin transport in planar [198] as well as 1D structures [199], has emphasised the potential of theoretical propositions for fully integrated polariton based spin circuits [200, 201]. The short lifetime of polaritons considered to be an impediment for thermodynamic equilibrium and bosonic condensation can now be seen as an advantage in creating ultra-fast spin logic devices. In this regard, as non-resonant excitation schemes more closely resemble

polariton formation under electrical injection, they hold greater promise for the implementation of electrically controlled polariton spin devices. This remarkable possibility has been further highlighted by the development of novel electrically pumped polariton lasers [24, 25].

In this chapter we demonstrate that the spin imbalance of a polariton condensate can be vigorously modulated by the polarization properties of the non-resonant excitation when the interactions between coherent and incoherent states are suppressed due to the spatial separation of condensate and reservoir in the optical trap configuration. We show that the microcavity sample in the non-linear regime features a strong linear to circular polarisation conversion enabling the manipulation of the condensate circular polarization by tuning the linear polarization angle. The contribution of the exciton reservoir spin dynamics to the spin imbalance of the condensate is confirmed by a perturbation of the dynamic equilibrium state by a cross-polarised weak femtosecond pulse which is shown to trigger a spin flip on the order of tens of picoseconds. Moreover, the condensate density is shown to strongly effect the resulting spin imbalance leading to a spin reversal at high densities. This reversal is explained within the framework of coherent Josephson coupling between the condensate spin states while results of theoretical simulations closely reproduce the observed features. These experiments confirm that the polarization of non-resonant excitation indeed survives the relaxation mechanisms from electron and holes to excitons and polaritons and its effects are exacerbated when the strong interactions from the reservoir are filtered out. Furthermore, Josephson coupling effects between spin up and spin down coherent states are demonstrated to be an important factor governing the anisotropic population of the condensate spin states at high densities.

6.1 Polarisation build-up in polariton condensates

In polarization resolved experiments with resonant excitation [197], parametric stimulation [193] as well as in the OPO configuration [202], the extensive correlation of the polarization of the exciting photons with the polarization of the optically imprinted polaritons has been extensively studied. For non-resonant excitation, prior studies have demonstrated that upon condensation, the polarization of the condensate is pinned to one of the crystallographic axis of the microcavity structure independent of the exciting polarization [20, 203]. This effect has been originally attributed to a linear polarization splitting of $\approx 0.1meV$ (at $k_{\|} = 0$), disputing that the emission polarization is inherited from the excitation under non-resonant excitation [20]. The spontaneous emergence of a strong linear polarization upon condensation threshold has in-fact been treated as a suitable order parameter for determining the emergence of coherence in the system [204, 205]. In more recent

experiments however, a higher total degree of polarization was reported for circular non-resonant pulsed excitation than for linear [76]. Moreover in polariton spin textures generated under circular polarisation excitation a high degree of co-circular polarisation was reported in the vicinity of the pump spot [198, 199]. These experiments confirmed that there is indeed, to some extent, correlation between the optical excitation with the polarisation of the condensate, at least in GaAs/AlGaAs samples that don't suffer from optical disorder to the same extent as CdTe samples.

6.2 Polarisation resolved study of optically trapped polariton condensate

To study the polarization properties of the optically trapped polariton condensate we initialize the condensate using the optical trap configuration of chapter 4. Using a non-resonant continuous wave (CW) linearly polarised pump spatially shaped in the form of an annular ring we create the Ψ_{00} coherent state in the optically induced trap. The S_+ and S_- components of the emission below and above threshold are resolved with the use of a $\lambda/4$ wave-plate and a linear polariser and we then reconstruct a real space image of the S_z stokes component.

6.2.1 Circular polarisation build-up at threshold

Below threshold we do not detect any significant circular polarization from polaritons inside the trap (fig.6.1a), however, just above threshold we detect a strong circularly polarised emission with circular polarisation degree (CPD) of ≈ 0.6 (fig.6.1b). This is in stark contrast to the linear polarization build-up previously reported for polariton condensates [20]. It is worth noting that the circular component originates exactly from the emission of the condensate while the CPD of the surrounding reservoir is negligible. Interestingly, this strong S_z stoke component persists far from the peak of the condensate and has a value of > 0.5 even where the condensate intensity is 10% of its peak intensity (fig.6.1d). Comparison with the effective trapping profile in the form of the emission below threshold demonstrates that this spin anisotropy quickly goes to zero at the potential barrier of the trap.

6.2.1.1 Effects of tight focus

Although the emergence of a strong spin imbalance from a linearly polarised optical pump appears counter intuitive at first, it can nevertheless be interpreted if one takes into account that the polarisation of a monochromatic tightly focused optical field does not have a uniform polarisation in the focal plane. For high numerical

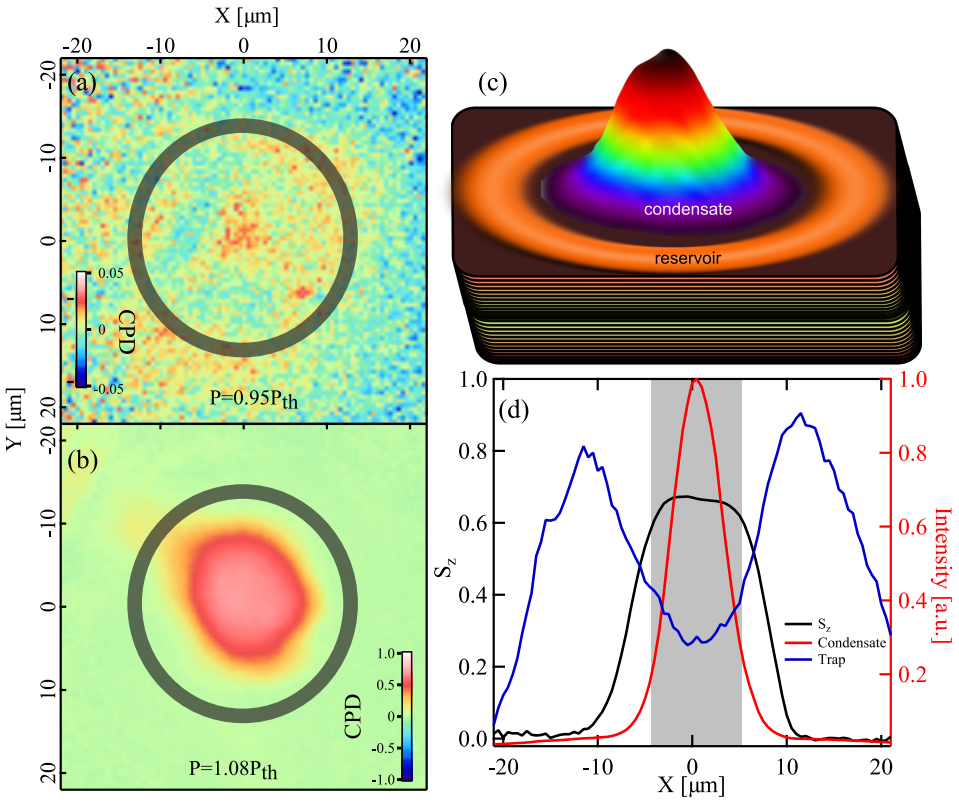

FIGURE 6.1: Real space Circular polarisation map below ($P = 0.95P_{th}$), **(a)**, and above ($P = 1.08P_{th}$), **(b)**, condensation threshold.**(c)** Schematic representation of reservoir and condensate on the microcavity structure. **(d)** Profile of polariton emission intensity above threshold (red line, right axis) and below threshold (blue line, right axis) and degree of circular polarisation (black line,left axis) vs distance from the centre of the trap.

aperture systems, scalar diffraction geometry is insufficient to accurately describe the electromagnetic field in the focal plane. A vectorial analysis of light is required in order to precisely describe the electromagnetic field in the focal plane [206]. Indeed it is a well studied effect that the electric field in the focal plane of a high numerical aperture aplanatic system can induce a small degree of ellipticity even for a fully linearly polarised source [207, 208]. In our setup, we employ a microscope objective with $N_A = 0.4$, that yields a measured degree of circular polarisation at the centre of a focused linearly polarised beam of 0.1. Moreover, this ellipticity is calculated to be greater towards the periphery of the focal plane, where our ring-like excitation pattern is found, than in the central region [206].

This induced ellipticity does not play an important role below threshold where the emission is stronger in the excitation region. Indeed, it has been predicted that spin noise fluctuations are extremely sensitive to the ground state occupation number and strength of interactions in polariton systems [209]. The authors of ref.[209] also demonstrate that the spin noise spectrum strongly depends on whether the system is described by thermal or coherent statistics and that in the case of coherent statistics the spin noise spectrum is suppressed and the spin correlation time is

considerably enhanced. Therefore in the in-coherent state a small imbalance (pump with small ellipticity) in the injection of carriers is not expected to have a noticeable effect in the polarisation of the emission due to fast spin de-coherence. This effect has been demonstrated even for fully circular optical excitation schemes [76], where below threshold the degree of circular polarisation is negligible. However, upon crossing the condensation threshold, a drastically different picture emerges. Spin fluctuations are greatly suppressed and density dependent bosonic amplification favours the polariton spin state with higher occupation. Absent any spin relaxation mechanism between S_+ and S_- polaritons this mechanism gives rise to a strongly circularly polarised polariton condensate. Furthermore the de-localisation of the condensate from the exciton reservoir further aggravates this behaviour as spin de-coherence channels associated with scattering with incoherent particles are considerably suppressed(fig.6.1b, section 4).

6.2.2 Polarisation modulation with angle of linear polarisation of excitation

In order to further characterise the origin of this spontaneous circular polarisation in the condensate it is meaningful to establish whether it is isotropic and independent of the angle of the linear polarisation of the optical pump. To this end we initialize the condensate above threshold ($P = 1.1P_{th}$) as before and using a half wave-plate we rotate the linear polarisation of the excitation. Figure 6.2a displays the circular stokes component map for horizontal ($0\,^\circ$) excitation showing a high degree of circular polarisation. Rotating the angle initially has a marginal effect on the circular stokes component of the condensate. However, for polarisation rotation above $90\,^\circ$, the coherent emission starts to becomes less strongly circularly polarised eventually leading to a complete reversal of the polarisation at $130\,^\circ$ where the condensate emission is now cross-circularly polarised (CPD= -0.6) (fig. 6.2b). After a π rotation the condensate has regained its original polarisation as expected. Figure 6.2c depicts the CPD when it is closest to the tipping point where some internal structuring can also be observed. Interestingly the CPD of the system has almost a 2θ relation with the angle of the linear polarisation of the excitation, shown in figure 6.2d where the value of each point is the average of the CPD in the central region of the condensate. Although a strong correlation between the angle of the linear polarization of the excitation and the resulting linear polarization of the condensate has been previously reported in the OPO configuration [202], a correlation between the angle of the linear polarization of the pump and of the circular polarization degree of the condensate has not been reported.

The demonstrated 2θ dependence on the angle of the excitation polarisation is a strong indication that a potent optical anisotropy is present in the sample. Light

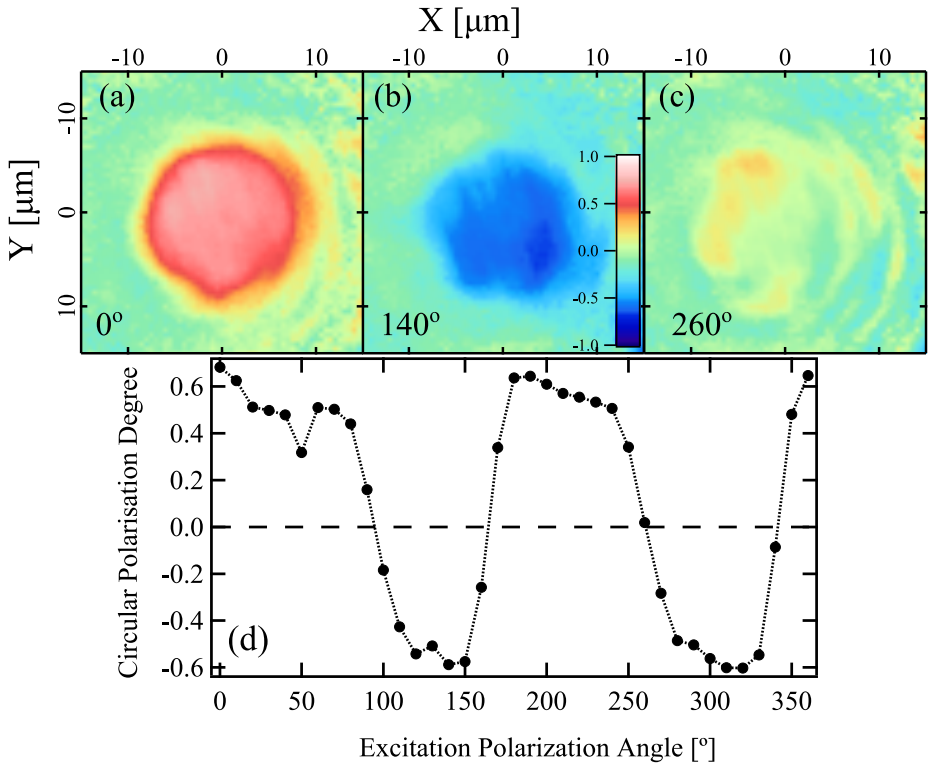

FIGURE 6.2: Variation of the condensate circular polarisation degree with the angle of the linear polarisation of the excitation. Circular polarisation maps of the confined polariton condensate above threshold for $\theta = 0$ **(a)**, $\theta = 140$ **(b)** and $\theta = 260$ **(c)** of the linear polarisation. In **(d)** the average CPD is plotted versus external polarisation angle featuring a 2θ dependence.

focused on the surface of the sample propagates through the top DBR mirror, where there is no absorption for the excitation wavelength ($\lambda_{laser} = 752nm$), before exciting electrons and holes in the cavity and the QWs. As previously described (section 3.3.1), in our sample the DBR consists of pairs of AlAs/$Al_{0.3}Ga_{0.7}As$ layers. A number of reports, of multi-layered structures composed of GaAs and AlAs, have reported linear birefringence [210–212]. The linear birefringence of the DBR will therefore exacerbate the ellipticity of the exciting electromagnetic wave. However the phase shift, between longitudinal and transverse modes, accumulated while propagating through the structure will not result in full circular polarisation, since under normal excitation conditions (Gaussian excitation) a linearly polarised pump in this specific sample features a linear polarisation upon threshold independent of the linear polarisation angle.

6.2.3 Condensate perturbation with a cross-polarised pulse

It is interesting to examine whether the spinor state is resilient or adaptable to external perturbations and if the condensate adjusts its final spin state if it is seeded with a different spin imbalance. To examine this, we devise a hybrid CW-pulsed

excitation scheme. The trap and condensate are formed with linearly polarised ($0\,^{\circ}$) CW excitation just above threshold (P=1.1P$_{th}$) with a strong circular polarisation degree of 0.65. We proceed to perturb it with a non-resonant, cross-circularly polarised $200fs$ Gaussian pulse with a spot size of FWHM of $5\mu m$ which is comparable to size (FWHM) of the condensate. The optical power density of the pulse is adjusted to be well below the threshold power for condensation ($\approx 0.5P_{th}$), in order to only weakly affect the geometry of the trapping potential. In this way we effectively create an incoherent reservoir overlapping the condensate. We then resolve the evolution of the condensate spin populations over time by time-resolving the two spin components of the emission using a streak camera.

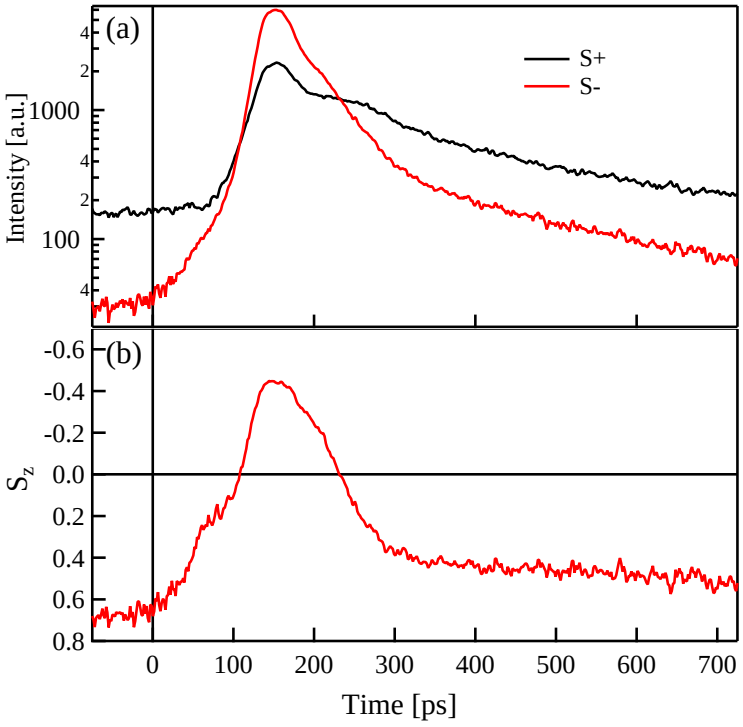

FIGURE 6.3: **Spin Dynamics of the perturbation of the confined polariton condensate by a femtosecond pulse**

Figure 6.3a depicts the time evolution of the two spin components, while the arrival of the pulse is set at zero time. Figure 6.3b displays the corresponding z component of the stokes vector. We observe a fast rise in the population of the S_{-} component shortly after the arrival of the pulse, eventually triggering a spin reversal in the condensate approximately at 110ps. This population reversal persists for more than 100ps orders of magnitude greater than the pulse duration, inadvertently demonstrating that this is a process driven by a highly polarised reservoir. Ultimately both spin populations decay towards their pre-pulse levels with a decay time of $\approx 190ps$, indicative of the reservoir dynamics.

6.3 Density dependent spin switching

In the previously discussed results, the excitation power of the non-resonant, non-local pump and therefore the condensate population density was kept constant and close to the threshold value (P=P_{th}). In polariton condensates, increase of the density has been shown to have a strong impact on the resulting polarisation through the increase of spin dependent polariton-polariton interactions that tend to depolarize the emission [76, 213]. It is therefore interesting to investigate if this effect is also observable under optical confinement or if the de-localisation of the reservoir will lead to a density independent polarisation. To investigate this, we perform a power-dependent polarisation resolved experiment in the optical trap configuration.

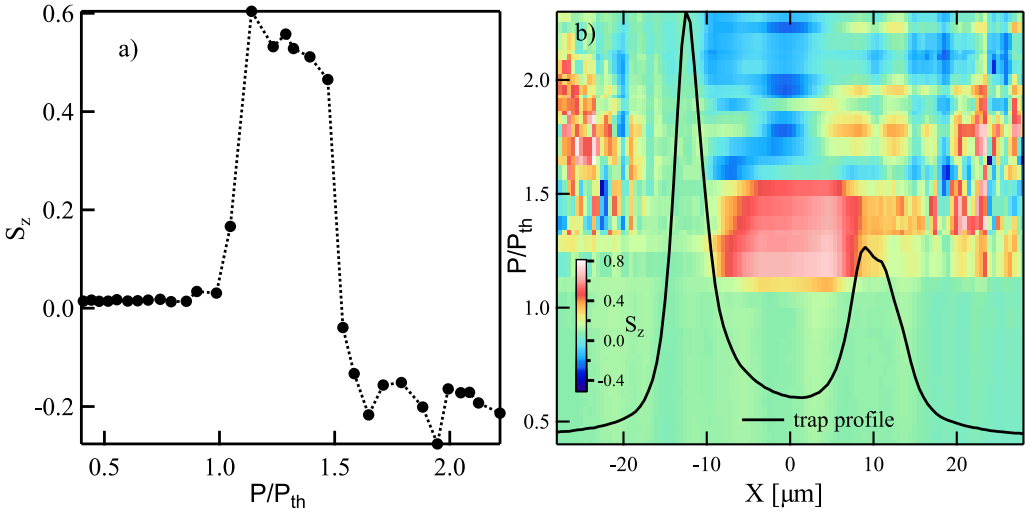

FIGURE 6.4: **a)** S_z as a function of excitation power over threshold. **b)** Corresponding power dependence of the 1D profile of the S_z component in the trap. The black line is the emission below threshold from the trap barriers.

In fig. 6.4a the dependence of the z stokes component on the threshold normalised excitation density is presented, where we observe the sharp rise at threshold is evident. Interestingly we observe a similar depolarisation behaviour as the power is increased up to 1.5 times the threshold value. However at 1.5 times the threshold power we observe a sharp reversal of the z component of the stokes vector of the polariton pseudo-spin and a subsequent gradual build up of the opposite polarisation. Fig. 6.4b depicts the 1D polarisation profile of the emission for increasing power while the black line outlines the relative position of the trap barrier. Interestingly, in the centre of the trap where the overlap with the reservoir is minimal, the effect is much more pronounced. In the pumping regions and outside of the trap the behaviour is more complex. In this implementation of the optical trap the intensity of the excitation along the ring was non-uniform resulting in asymmetric barrier height. It is noteworthy that within the excitation region of the highest

barrier, the polarisation is almost completely suppressed, contrary to the opposite side where the barrier is shallower and a more complex behaviour is observed. This condensate spin reversal behaviour has not been previously reported or observed and cannot be explained with previously developed theoretical tools.

6.3.1 Theory of Spin Inversion in ring excitation experiment

In the ring excitation experiment, a non-resonant continuous-wave laser of linear polarisation induces a circularly polarised condensate. While the laser is linearly polarised, its oblique angle of incidence results in a slight ellipticity of light absorbed by the microcavity. This results in a slight non-zero circular polarisation of the reservoir of hot exciton states that feeds the condensate. Neglecting spatial dynamics, we can write the spin dependent evolution equations of the reservoir spin populations $N_{\sigma\pm}$:

$$\frac{dN_{\sigma\pm}}{dt} = -\left(\Gamma_R + Rn_{\sigma\pm}\right) N_{\sigma\pm} + P_{\sigma\pm} \tag{6.1}$$

where Γ_R is the reservoir decay rate, R is the condensation rate and n_σ represents the polariton condensate spin populations. The pumping rate can be written as $P_{\sigma\pm} = \frac{1+\sigma_\pm \rho_p}{2} P_0$, where P_0 is the pumping strength and ρ_p is the circular polarisation degree of light absorbed by the microcavity, which we take to be small $\rho_p = 0.05$.

The polariton spin populations are given by:

$$\frac{dn_{\sigma\pm}}{dt} = \left(RN_{\sigma\pm} - \Gamma\right) n_{\sigma\pm} - \sigma_\pm \lambda \left(GP_+ - GP_-\right) n_+ n_- \tag{6.2}$$

where Γ is the polariton decay rate. The last term represents an energy relaxation term.

Assuming that $P_+ > P_-$ we can expect blue-shifts for the σ_+ and σ_- polariton spin components of GP_+ and GP_-, respectively, where G represents the "pump-induced repulsion" (previously introduced in Ref. [214]). The implicit assumption here is that the hot excitons introduced by the non-resonant pump can be classed into two types: "active" excitons with the correct spin, energy and momentum to directly scatter into the condensate and "inactive" excitons that do not. N_σ represents only active excitons, while a majority of inactive excitons can still be expected to be present. The inactive excitons can be assumed to have a density proportional to the pump intensity and contribute only to the blueshift experienced by polaritons. The energy relaxation rate is assumed to be proportional to the difference in energies of the σ_+ and σ_- components, caused by this blue-shift. In general this blueshift can be modified by polariton-polariton interactions as well as terms depending on N_σ. However, for the purposes of demonstrating qualitatively the effect of energy relaxation on the spin polarisation, it is more transparent to neglect these secondary effects and avoid introducing additional parameters.

The energy relaxation introduced in this form is phenomenological [181, 182], although physically can be understood in terms of scattering between polaritons and hot excitons [215]. The spin-flip of a polariton undergoing energy relaxation is balanced by a spin-flip of an exciton in a hot exciton state (although assuming the reservoir is large, we neglect any effect on N_σ). Given that the process may be stimulated, the scattering rate is dependent on the polariton density.

Equations 6.1 and 6.2 can be solved for the steady-state for a range of pump intensities, to obtain the circular polarisation degree, $\rho_z = \frac{n_+ - n_-}{n_+ + n_-}$. It is worth noting that, in addition to the pumping rate and the fixed value of ρ_p, only two dimensionless parameters affect the resulting circular polarisation degree: Γ_R/Γ and $\lambda G \rho_p \Gamma^2/R^2$ (this can be seen by working with rescaled quantities $n_\sigma = n'_\sigma \frac{\Gamma}{R}$, $N_\sigma = N'_\sigma \frac{\Gamma}{R}$ and $P_\sigma = P'_\sigma \frac{\Gamma}{R}$).

The circular polarisation of polaritons is shown in Fig. 6.5.

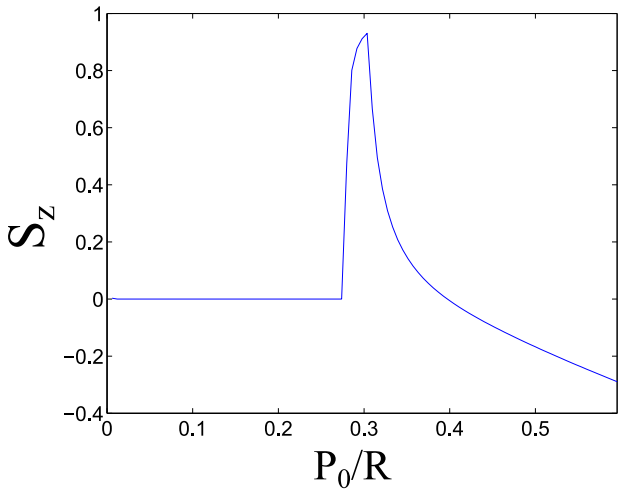

FIGURE 6.5: Variation of the condensate circular polarisation degree with pump intensity, P_0/R. Parameters: $\Gamma_R/\Gamma = 0.146$, $\lambda G \rho_p \Gamma^2/R^2 = 2.392$, $\rho_p = 0.05$.

Although the reservoir is only very slightly spin polarised, this is sufficient to create a significant imbalance of polariton spins due to the fact that the σ_+ population crosses the condensation threshold first. For large densities, the energy relaxation, favours population of the σ_- polarised state, which has lower energy due to the pump induced blue-shifts.

6.4 Conclusions

We have demonstrated the spontaneous emergence of a strongly circularly polarised condensate with the use of an optical trapping scheme under linear excitation. The observed condensate features remarkable circular polarisation tunability by the polarisation properties of the external optical pump. Moreover we demonstrated

a hybrid cw-pulsed excitation scheme that flips the condensate in the ps scale. These results clearly demonstrate that the condensate spin population strongly correlates with the polarisation of the incoherent reservoir and that polariton condensate polarisation can be strongly affected by the optical anisotropy in the cavity mirrors and that decoupling the reservoir from the condensate suppresses spin noise and de-coherence. These results coupled with the understanding of the excited state condensation introduced in chapter 5 can facilitate design of complex polariton based spinoptronic devices [201, 216].

Disclaimer:

The simulations and theoretical modelling of section 6.3.1 were performed by Tim C.H. Liew.

CHAPTER 7

Dispersion Linearisation in the High Density Regime

The unambiguous demonstration of a superfluid phase transition is the demonstration of the linearisation of the momentum distribution of thermalised particles. In solid state systems exciton-polaritons feature prominently as a system for the robust implementation and study of superfluid phenomena and dynamics. In this chapter we discuss the appearance of a linear Bogoliubov-like dispersion in the optical trap configuration under non-resonant pulsed excitation and examine the dynamics of its formation. As previously described, under ring excitation, we obtain polariton condensation in the centre of the ring spatially de-localised from the exciton reservoir. The advantage of this configuration is the increased temporal coherence with respect to Gaussian excitation, which is favourable for discerning linearisation of the dispersion. Additionally separating the condensate from the reservoir filters out the strong interactions of the condensate with the incoherent exciton reservoir allowing us to be in the weakly interacting regime where the interaction strength can be tuned by tuning the exciton coefficient of the lower polariton branch (LP) which can be accomplished by changing the energy detuning between the exciton mode and the cavity resonance. We demonstrate that the observation of the linearisation of the momentum distribution of a polariton condensate, under pulsed non-resonant excitation in the static time-integrated domain, does not necessarily occur due to the transition to a Bogoliubov excitation spectrum but can be an artificial feature arising from the integration over the time varying dynamics of the non-equilibrium system. We evidence how this can be more pronounced in experiments carried out in spatially confined polariton condensates which has

been the case for previous demonstrations of the Bogoliubov dispersion under non-resonant pulsed injection schemes.

7.1 Superfluidity in polariton condensates

Exciton-polariton superfluidity is an attractive prospect both theoretically and experimentally. A phenomenological description by Landau, as well as a microscopic theory by Bogoliubov are at the heart of understanding and quantifying this effect. Bogoliubov's theoretical formulation for the description of a weakly interacting Bose gas predicts the re-normalisation of the parabolic excitation spectrum of the system to a phonon-like linear distribution for low momenta [217]. Shortly after the observation of the first atomic BECs [17, 18, 50], this linearisation of the the momentum distribution was experimentally authenticated by indirect measurements of the speed of sound in the condensed phase [218] and by the optical excitation of phonons in an atomic BEC [219]. The subsequent emergence of solid state analogues to atomic BECs has allowed for a more comprehensive study of the subtle relation of the BEC phase transition with superfluid phenomena [49] and the engineering of potential applications.

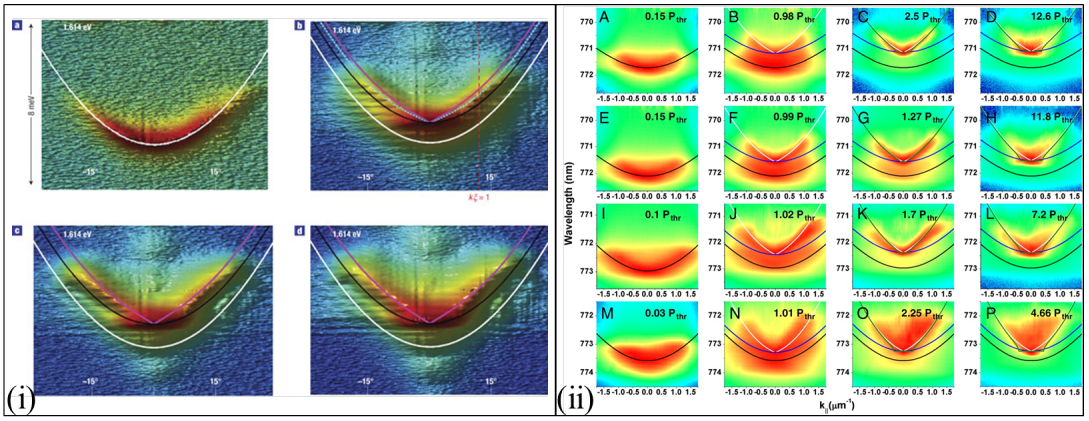

FIGURE 7.1: (i)Time-integrated dispersions for $P = 0.05P_{th}$ (a), $P = 1.2P_{th}$ (b), $P = 4P_{th}$ (c) and $P = 6P_{th}$ (d) fvrom ref. [85]. (ii) Polariton dispersions on a logarithmic scale for different excitation densities and detunings: $\delta = 0meV, -2meV, -4meV, -7meV$ from top to bottom row respectively from ref. [86]. Both reports were done using the same sample on top of which a thin metal film with circular holes is incorporated a trapping potential and were excited with pulsed non-resonant excitation

Experimental demonstrations of superfluid behaviour in microcavity polaritons have been extensively reported [83, 84, 109], as well as the "smoking gun" of superfluidity, the linear Bogoliubov excitation spectrum under non-resonant pulsed excitation [85, 86] and resonant four wave mixing experiments [87, 88]. Advantageously in polaritonic systems the momentum distribution of particles is directly observable

by means of far-field spectroscopy. Therefore the direct observation of the Bogoliubov excitation spectrum of a polariton condensate is experimentally straightforward compared to the atomic case. Interestingly, despite the numerous reports of polariton condensation, in many different materials (i.e [138, 139]), there have only been two reports of the experimental observation of the linear Bogoliubov dispersion above threshold for non-resonant excitation schemes (see fig. 7.1). Both of these reports employed pulsed optical injection in a sample where a thin metal film with circular holes is overlaid on the microcavity structure in order to create a trapping potential [85, 86]. Surprisingly there has not been a report of the linearisation in the dynamic-equilibrium steady state regime where Bosonic condensation was first reported [20]. Moreover, the theoretically expected dependence of the speed of sound on the density of the condensate ($E_{Bog}(k) \approx \hbar k \sqrt{\frac{N_0 U_0}{m_{lp}}}$, where U_0 is the polariton-polariton interaction constant [39]) has not been explicitly experimentally verified as in the atomic case [218], even though it is experimentally straightforward to examine, by increasing the excitation density (N_0) once a Bogoliubov spectrum is observed. Nevertheless, this dependence has been employed indirectly to interpret experimentally observed features in propagating polariton quantum fluids [109].

7.2 Linearisation of the polariton dispersion in the static regime

To probe the condensate features in the high density regime greatly above threshold we utilise a pulsed 100 KHz Q-switched system to amplify the 200fs pulses of our ultra-fast oscillator. Raising the power more than 10 times above threshold we observe the dispersions of fig. 7.2. We note that the emission recorded in this case is integrated for the entire duration of the lifetime of the pulse so that the resulting image is the average of the dynamics of the emission.

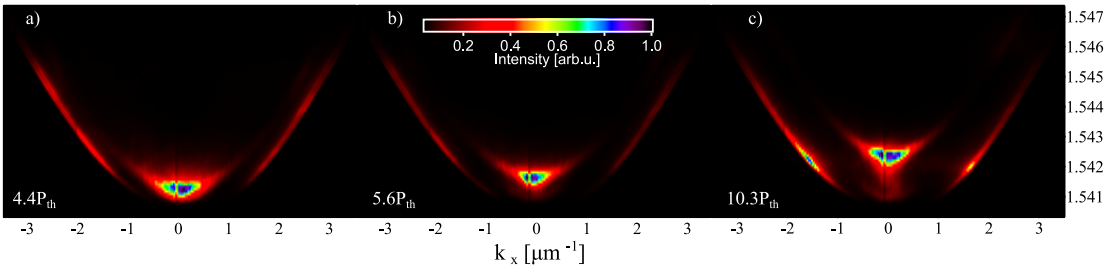

FIGURE 7.2: Static dispersion images above threshold under pulsed excitation for $P = 4.4P_{th}$ a), $P = 5.6P_{th}$ b) and $P = 10.3P_{th}$ c).

In fig. 7.2 the emission from the trapped particles as previously discussed in chapter 4, originates from the high intensity region around $k_x = 0$ while the high momentum polaritons populating the higher energies of the dispersion correspond to

emission from the periphery of the annular excitation. Already at excitation densities 4.4 times above threshold the polariton dispersion appears to strongly deviate from the expected parabolic shape at $k_x = 0$ (fig. 7.2a). Increasing the optical power of the non-resonant excitation pulse, the measured dispersion progressively appears to be linear around $k_x = 0$. Extracting the inclination around $k_x = 0$ for fig. 7.2 we note an increasing trend from $1.085 meV\mu m$ (fig. 7.2a), to $1.406 meV\mu m$ (fig. 7.2b) to $1.661 meV\mu m$ in fig. 7.2c. This behaviour strongly resembles the theoretically expected Bogoliubov distribution and its dependence on density. Namely the increase of the speed of sound in the system, that is proportional to the inclination of the linear Bogoliubov dispersion, for higher densities. Interestingly this apparent linearisation of dispersion forms only under pulsed excitation and this appears to be the case in all previous reports of Bogoliubov dispersion in polariton condensates under non resonant optical excitation [85, 86]. It is noteworthy that for low energies the momentum distribution appears as a filled triangle similar to the observations of ref. [86] presented in z fig. 7.1b. It can be interpreted as an artifact of the transient relaxation of the system during the time integration. At this point it is meaningful to examine the real space emission of the system with these conditions under similar densities. Fig. 7.3 depicts the emission from the sample for similar excitation densities. Although, for these densities we don't expect to observe a clear pattern in the static picture as transient relaxation will artificially mix the eigenstates of the trap we note that for increasing excitation density the emission becomes increasingly uniform while the high density regions are gradually washed out.

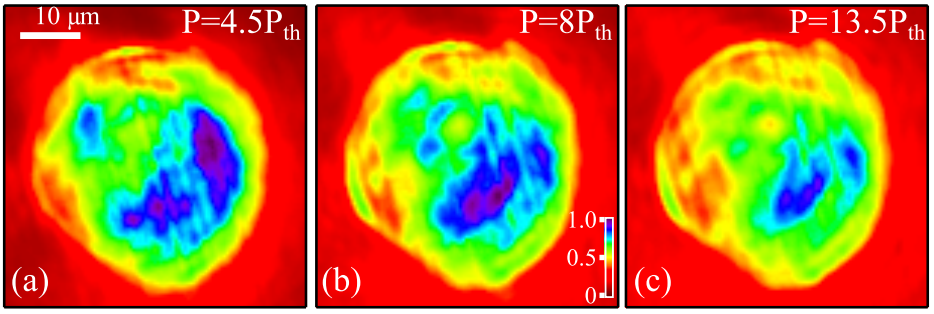

FIGURE 7.3: Static real space images above threshold under pulsed excitation for $P = 4.5P_{th}$ a), $P = 8P_{th}$ b) and $P = 13.5P_{th}$ c).

7.3 Transient domain dispersion imaging

To reveal the true nature of this apparent linearisation of the dispersion for high excitation densities as well as the dynamics of its formation we study the dispersions in the transient domain. Using the temporal tomographic setup section 3.2.4

described in section 3.2.4 we resolve the condensate dispersion with our streak system, while also spatially filtering out the emission coming from the ridges of the ring excitation. Initializing our system with an excitation power 8 times above threshold at a negative detuning of -5meV we reconstruct the transient frames of the dispersion which we also fit with our coupled oscillator model, where the values are set by steady state CW measurements.

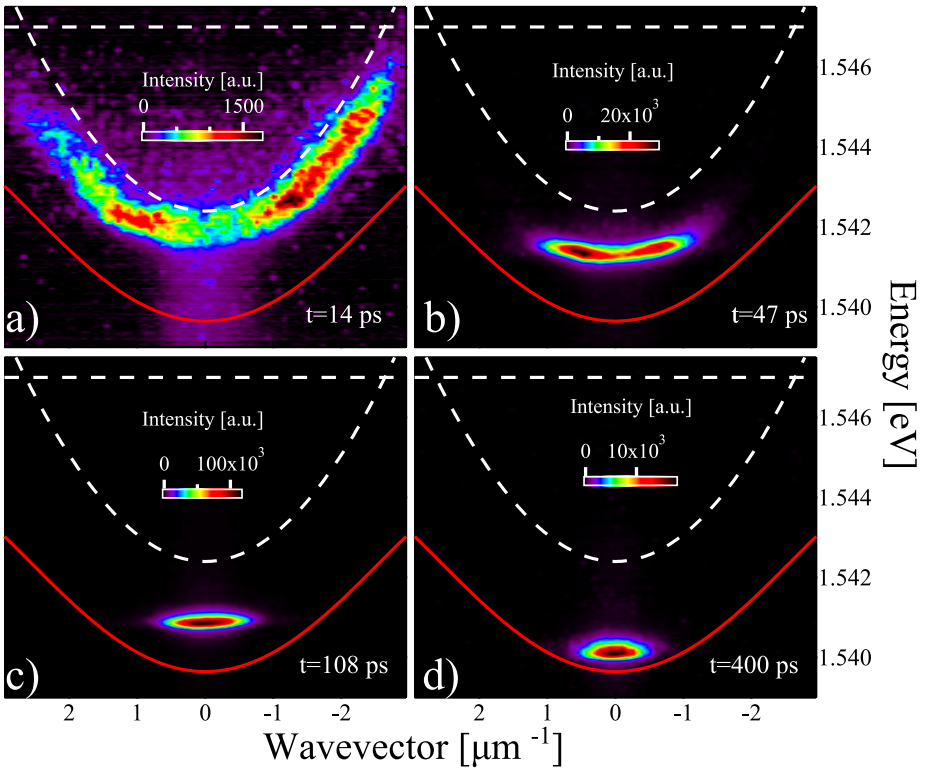

FIGURE 7.4: False color-scale, reconstructed dispersion images from transient dispersion tomography. a) t= 14ps, b) t=47ps, c)=108ps and d) t=400ps. Red lines indicate the unperturbed lower polariton mode, while the dashed lines mark the uncoupled cavity and exciton modes

Approximately 14 ps after the arrival of the pulse we see the formation of Figure 7.4a. The emission for this time frame has a very broad momentum distribution and is arguably in the weak coupling regime. As the excitons and polaritons decay, the dispersion relaxes in energy and also shrinks in momentum space 7.4b eventually entering the polariton condensate regime 7.4c and gradually approaches the unperturbed low density polariton dispersion approximately at 400ps. Previous studies on the crossover from photon to polariton lasing present a similar behaviour [148]. Interestingly, at no point during this dynamic process does the dispersion appear to be linearised close to $k_x = 0$ as in the time-integrated measurements.

A linearisation of the dispersion only appears as the result of integration over time from both the transient measurement or directly from time integrated dispersion imaging (CCD) fig. 7.5. It is worth noting here that when spatially filtering the

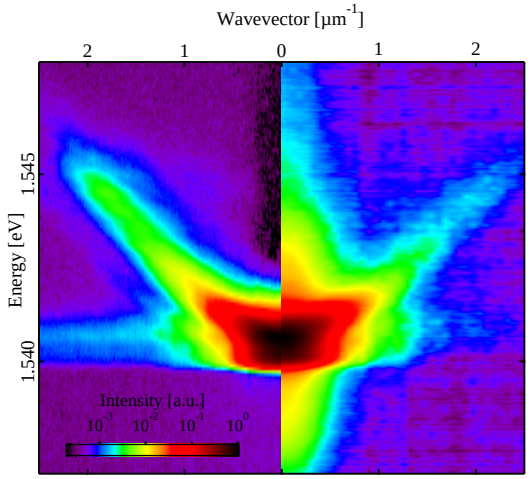

FIGURE 7.5: Comparison of time integrated dispersion images from the CCD (left part) and the streak (right part of the graph).

emission from the microcavity, the measured dispersion is broadened with respect to wave-vector in order to comply with position momentum uncertainty.

The transient energy relaxation of the emission from the weak coupling photon lasing regime to the confined polariton condensate state is indeed expected to shrink the Δk of the energy distribution as the polariton condensate is formed inside the optical trap and the momentum degrees of freedom are reduced. Fig. 7.6b displays the extracted transient energy relaxation of the ground state of the dispersion ($k_x = 0$). An initial fast drop around 25ps is observed, corresponding to the crossover from photon ot polariton lasing, while in fig. 7.6a the dynamic narrowing of Δk_x is observed. This combined dynamical behaviour can lead to an artificial impression of the linearisation of the polariton dispersion in the static, time-integrated domain. For increased density the system is expected to be in the photon

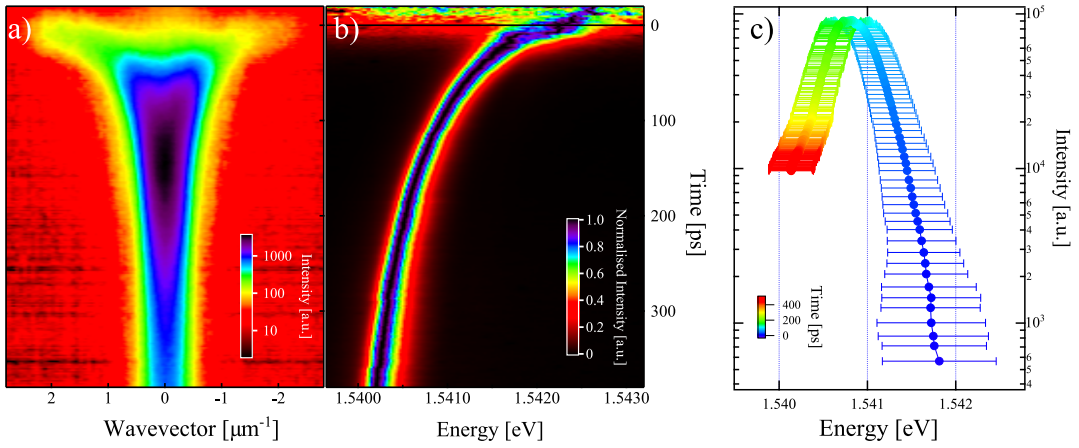

FIGURE 7.6: a) k_x profile (integrated over the entire energy of the dispersion) evolution in time and b) energy relaxation (for $k_x = 0$) vs time. c) Intensity vs energy relaxation colour-coded with the corresponding time. a) and b) are both intensity normalised for every time-frame to better reveal the discussed features.

lasing regime for a longer period while polariton condensation occurs at a later time (after the pulse). This effectively results in a bigger part of the emission originating from the weak coupling regime and therefore the inclination of the time-integrated dispersion will be modified as a result.

7.4 Phenomenological model of dispersion relaxation

To simulate the observed phenomena we construct a phenomenological transient relaxation model based on the coupled oscillator model (COM) described in section 1.2. The lower polariton mode obtained from the COM is artificially dressed with a Bose-Einstein distribution with a temperature of 7K by modulating the intensity of the dispersion of the lower polariton mode. The transition to the weak coupling regime is then approximated by a quick collapse of the Rabi splitting for $t < 25ps$. A time-dependent blue-shift of the exciton resonance is then introduced in order for the energy of the simulated lower polariton mode to as closely correspond to the experimental one for the simulated time-range. Lastly, the maximum intensity for every moment in time is set to correspond to the experimentally measured intensity (fig. 7.6c). For this first order approximation, the cavity resonance and the temperature of the Bose Einstein distribution (T=7K) are kept constant throughout the simulation.

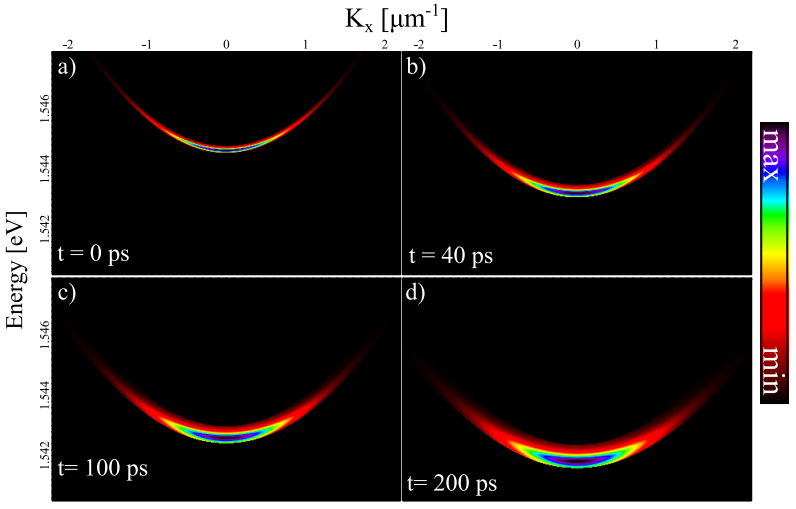

FIGURE 7.7: Simulated dispersion time frames as described in the text, t=0ps a), t=40ps b), t=100ps c) and t=200ps d).

The polariton dispersions of this model for different times are displayed in fig. 7.7. It is meaningful to point out that the anti-crossing of the polariton mode is not observable due to the imposition of the BED on the polariton dispersion, that suppresses the intensity of the higher energies. An indirect consequence of the blue-shift of the exciton resonance and the imposed collapse of the Rabi splitting for early times (t $\leq$ 25 ps) is the narrowing of the linewidth of the lower polariton dispersion

which does not qualitatively agree with the experimental behaviour. Nonetheless, integrating over the simulated time-range (0-350 ps) produces fig. 7.8a that is in good qualitative agreement with the experimentally measured time-integrated dispersions of fig. 7.5. Indeed, the characteristic "filling" of the dispersion around $k = 0$ seen in previous reports [86](fig. 7.1b) as well as in fig. 7.2 and fig. 7.5 is reproduced.

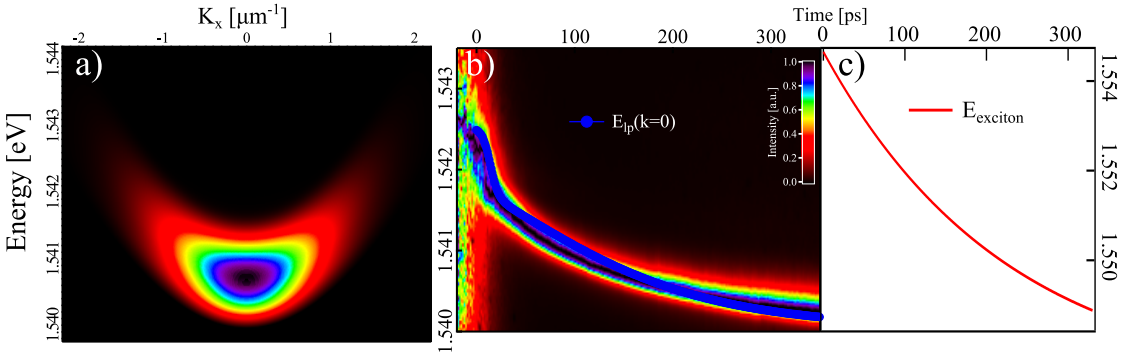

FIGURE 7.8: a) Time averaged simulated dispersion, b) Intensity normalised experimental energy relaxation of $E_{lp}(k = 0)$ overlaid with the corresponding simulated value (blue dots) as a function of time, c) Exciton energy used for the coupled oscillator model throughout the simulation as a function of time.

The time evolution of the energy level of the lower polariton branch at $k_{||} = 0$ superimposed on the experimental values, for the time range of the simulation, is presented in fig. 7.8b and the corresponding exciton energy is shown in fig. 7.8c. In the simulated time-integrated image the artificial linearisation of the distribution is not so pronounced, which can be attributed to a number of reasons but most importantly to the constant temperature of the BED and to the fact that the dispersion at early times is still in the strong coupling regime, albeit with a greatly reduced exciton-photon coupling. However, despite its inherent limitations this phenomenological model is shown to qualitatively reproduce the observed time integrated features.

7.5 Conclusions

Despite numerous observations of superfluid behaviour in polariton condensates, the fundamental theoretically expected distinction of the superfluid phase transition, the linearisation of the dispersion for small wave-vectors, remains to be confirmed in the dynamic equilibrium domain where the first observation of the BEC phase transition in polaritons was reported [20]. Considering the similarity of the observed features presented here as well as the close resemblance of the experimental specificities, previous observations of linearisation of the polariton dispersion under pulsed non-resonant excitation are not substantially conclusive.

Whereas a linear Bogoliubov excitation spectrum in polariton condensates under continuous wave excitation remains to be observed, linear dispersion features under pulsed non-resonant excitation schemes need to be thoroughly investigated also in the transient domain in order to ascertain the true nature of the observed linearities.

Part III

Magnetic Field Effects on Polariton Condensation

CHAPTER 8

Density and Polarisation Dependent Modulation of Polariton Condensate Zeeman Splitting

8.1 Polaritons under magnetic fields

The application of an external magnetic field can have pronounced effects on the energy spectrum of polariton both in the linear an non-linear regimes. Below condensation threshold the magnetic field affects polaritons in microcavities by affecting their excitonic part. Thus one can expect three kinds of linear magneto-polariton effects. Polaritons with spin parallel and anti-parallel to the orientation of the magnetic field will display an energy gap $\Delta E = \mu_B g B$, where μ_B is the Bohr magneton, g is the exciton g-factor that is dependent on the materials and the thickness of the QW [220] as well as the applied magnetic field. Furthermore, the presence of an external magnetic field results in an increase of the Rabi splitting due to the enhancement of the exciton oscillator strength which results from the increase of its binding energy [221]. It is also worth noting that the detuning of the system will change with increasing magnetic field due to the diamagnetic shift of the exciton resonance [222]. Finally, a Landau quantization of the exciton resonance will occur resulting in the emergence of a fine structure of the lower polariton eigenstates.

More interesting phenomena however occur in the polariton condensate regime for magnetic fields parallel to the growth axis (Faraday geometry) which are the result of its inherent two spinor component nature. With no magnetic field present polariton condensates in planar structures and with a spot excitation have been shown to be linearly polarized [20]. When applying a weak magnetic field the condensate is

expected to emit elliptically polarized light. This is derived from the minimization of the free energy of the system over S_z which is the normal-to plane component of the pseudo-spin of the condensate and effectively shows the imbalance of the spin up and spin down populations [223]. Furthermore the Zeeman effect has been predicted to be fully compensated by an increase of the blue-shift of the polariton energy in the condensed phase [223] up to a critical magnetic field where it is recovered and the condensate becomes fully circular polarized. This effect has come to be known as the spin analogue of the Meissner effect. The suppression of the Zeemann splitting can be interpreted as a result of the full paramagnetic screening of the magnetic field from the polariton condensate. This is expected to take place for a polariton condensate at thermal equilibrium.

Since the original introduction of the polariton spin-Meissner effect [223], the suppression of the Zeeman splitting has been reported in a number of experimental configurations. In 2010, Larionov et al reported on the quenching of the lower polariton Zeeman splitting, in a high Q GaAs microcavity with 7 nm quantum wells, up to a critical field of $B_{cr} = 2$ Tesla under non-resonant pulsed excitation [224]. Shortly after, Walker et al, studied the effect in the OPO configuration and demonstrated a density dependent re-normalisation of the energy splitting of the spin components of a polariton condensate which was attributed to phase synchronization of the spinor condensates due to a Josephson-type coupling [225]. The effect was also observed for the lowest trapped state in etched polaritonic traps of 1 to $10\mu m$ [226]. Finally in 2014 Fischer et al, reported on the polariton spin Meissner effect under CW non-resonant linear polarization excitation and demonstrated taken into account the detuning modulation of the system by the magnetic field [227]. The density dependent re-normalization of the Zeeman splitting at high magnetic fields has thus to be reported in the CW excitation regime. This is caused by the anisotropic blue-shift of the polariton spin states due to different population densities, that tends to compensate the Zeeman effect. Moreover it is interesting to examine whether excitations of different polarization would have some effect on this phenomenon due to selective population of one of the two states as described in chapter 6.

8.2 Quenching of Zeemann splitting with increasing polariton density

As the exciton g factor is strongly modulated, even reversing sign, by the width of the quantum well it is meaningful to examine the expected behaviour of the sample presented in section 3.3.1. In fig. 8.1a the g factor for varying quantum well width for GaAs/AlGaAs quantum wells is shown as was recorded in [220]a. For a 10nm GaAs/AlGaAs quantum well the expectation value is shown to be very close to zero

($g_{10nm} \approx 0.08$), therefore the applied magnetic field will have a very weak affect on the energy spectrum for the magnetic field range available in our setup (fig. 8.1b).

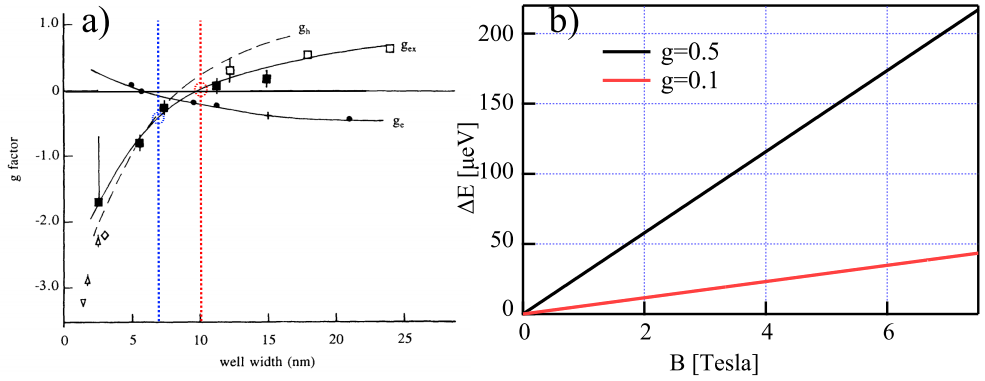

FIGURE 8.1: a) g factor of GaAs/AlGaAs quantum well excitons vs width from ref. [220], red dotted line and circle mark the expectation value for the exciton g factor of the high Q sample of section 3.3.1, blue dotted line and circle mark the expectation value for the exciton g factor of a 7 nm quantum well width microcavity sample. b) Exciton Zeeman splitting (ΔE) for g=0.1 (red line) and g=0.5 (black line) as a function of magnetic filed.

Therefore a different microcavity sample with 7nm GaAs/AlGaAs quantum wells was used to study the density dependence of the Zeeman splitting at high magnetic fields. From fig. 8.1a (blue circle) the expected g factor is found to be $g \approx 0.5$ for this quantum well width. This second AlGaAs based sample was grown in *Wilhelm Conrad Röntgen Research Centre for Complex Material Systems* of Würzburg University by the group of Professor Sven Höfling. It consists of 3 quadruplets of 7nm GaAs quantum wells in a $\lambda/2$ cavity positioned similarly as in ref. [70], while the cavity Q factor was experimentally determined to exceed 10000 and the Rabi splitting is $14.5meV$ [228]. It is worth noting here that the exciton g factor of fig. 8.1 is for $Al_xGa_{1-x}As$ quantum well barriers with x=0.36 which is very close to x=0.3 of the sample of section 3.3.1 but substantially different to x=0.2 of the Würzburg sample.

To probe the density dependence of the polariton spin-Meissner effect we perform a series of spin resolved power dependence experiments using the setup described in section 3.2.5.1 at a temperature of T= 5K. We set the magnetic field B=4 Tesla in order to be well above the critical magnetic field range previously reported in GaAs based microcavities [227] and non-resonantly excite our sample at a detuning of $\approx -4.5meV$ with our Ti:Saph CW laser source(section 3.1.1.1) with a spot of $\approx 25\mu m$ FWHM and 5% duty cycle modulation of the AOM at 10 kHz. We record the polariton dispersion for three different polarizations of the excitation; linear, left and right handed circular polarization. From the S_+ and S_- dispersions the spectra of the lower polariton branch at k=0 is extracted and fitted with a Gaussian curve. The energy difference of the spinor states for each power step is then deduced from the fitting constants of the curves.

8.2.1 Linearly polarised excitation

Fig. 8.2 displays the extracted k=0 spectra of the two spin components for excitation with a linearly polarised beam, for a field of B=4 Tesla. We note a strong Zeeman splitting of $\approx 90\mu eV$ greatly below threshold (Fig. 8.2a) where polaritons are in the linear regime.

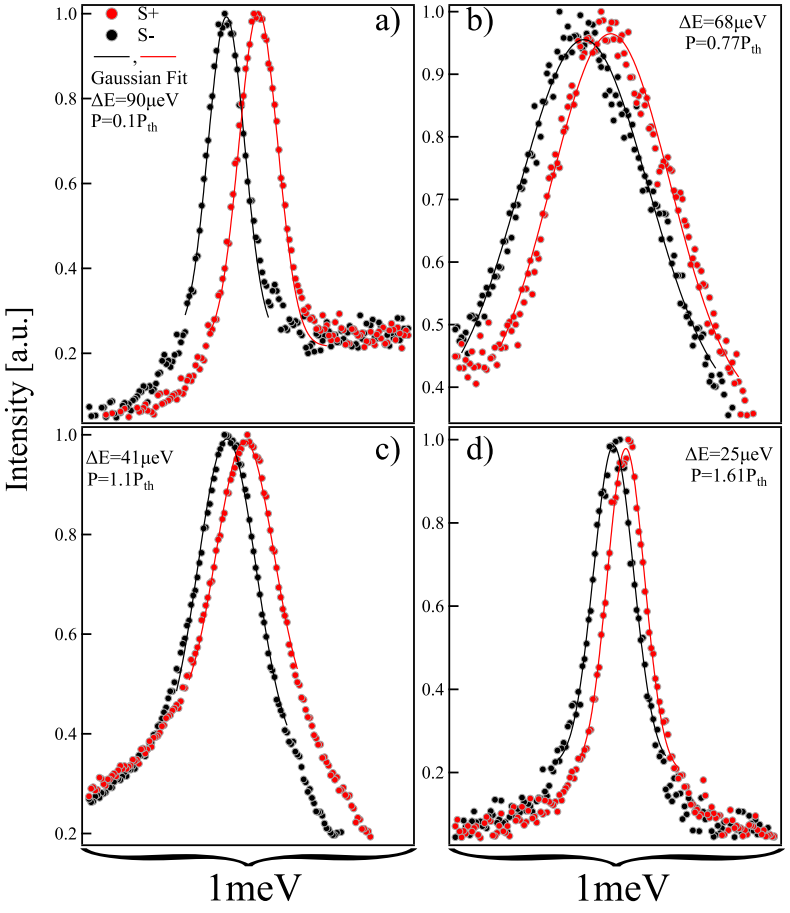

FIGURE 8.2: Spectra of $S+$ (red dots) and $S-$ (black dots) of the lower polariton branch at k=0 in the linear regime (P=0.1P$_{th}$) a), for P=0.77P$_{th}$ b), just above threshold (P=1.1P$_{th}$) c) and for P=1.6P$_{th}$ d). Red and black lines are Gaussian fits to the data.

While increasing the excitation density we observe the appearance of a broadened strongly blue-shifted mode fig. 8.2b that upon reaching the condensation threshold, undergoes a linewidth narrowing (fig. 8.2c,d). Moreover we note an obvious decrease of the energy splitting between the S_+ and S_- modes. Extracting the energy difference for the power range that we have investigated, we note an almost linear reduction of the Zeeman splitting for increasing polariton density(fig. 8.3). It is worth pointing out that this effect was previously demonstrated in the out of equilibrium regime of the polariton optical parametric oscillator [224]. Interestingly,

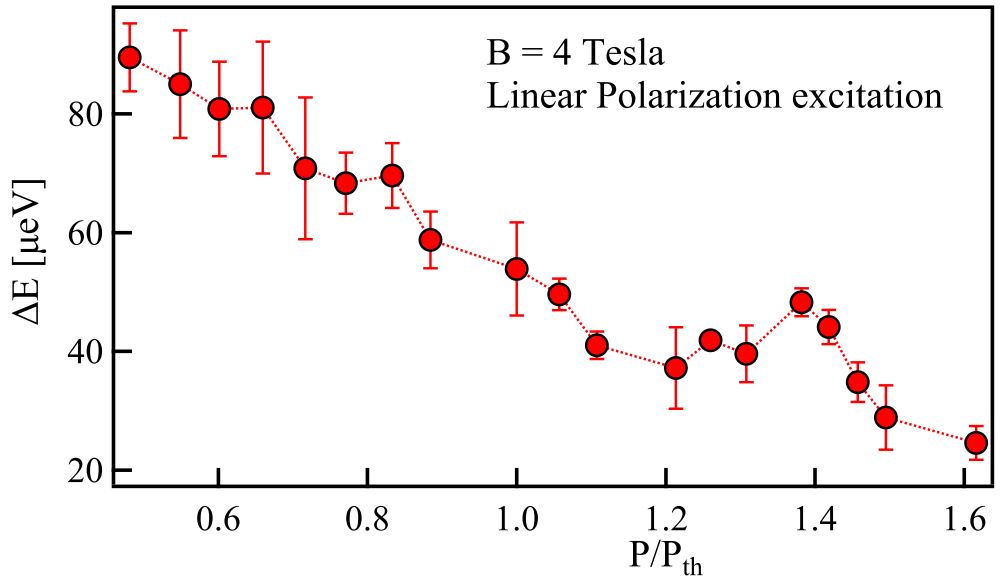

FIGURE 8.3: Polariton Zeeman splitting st k=0 as a function of threshold power density for B=4 Tesla under excitation with linear polarisation

the collapse of the ΔE is observed even below the polariton condensation threshold. The threshold value of $\Delta E \approx 40\mu eV$ is in quantitative agreement to previously reported values in a similar sample [227].

8.2.2 Circularly polarised excitation

A drastically different picture emerges when changing the polarisation of the excitation. Using a quarter wave plate to circularly polarise our excitation, we perform a second power dependence experiment at the same detuning, temperature and magnetic field but with left-handed circular polarisation of the excitation light. Greatly below threshold the energy splitting in the linear regime is very close to that observed under linear polarisation excitation $\Delta E = 105\mu eV$ (fig. 8.4a). However as the polariton density is increased the energy splitting quickly goes to zero before the onset of condensation and is negligible, within the experiment margin of error, for the range of powers that was examined (P=1.4P$_{th}$) (fig. 8.4b). This shows that the paramagnetic screening of the magnetic field and the critical field that this screening breaks down, are strongly dependent on the spin of the injected carriers. It is therefore interesting to examine whether injection of carriers with opposite spin will have the inverse effect on the condensate energy splitting. To this end we perform a reference experiment with the excitation beam cross circularly polarised with the previous case. Here we expect an enhancement of the energy splitting observed relatively to the linear polarisation excitation case. Fig. 8.4c shows the spectra of S_+ and S_- just below threshold where the energy splitting between them is $\approx 135\mu eV$ while increasing the power above threshold up to P=1.5P$_{th}$ the Zeeman splitting is reduced to $\approx 114\mu eV$.

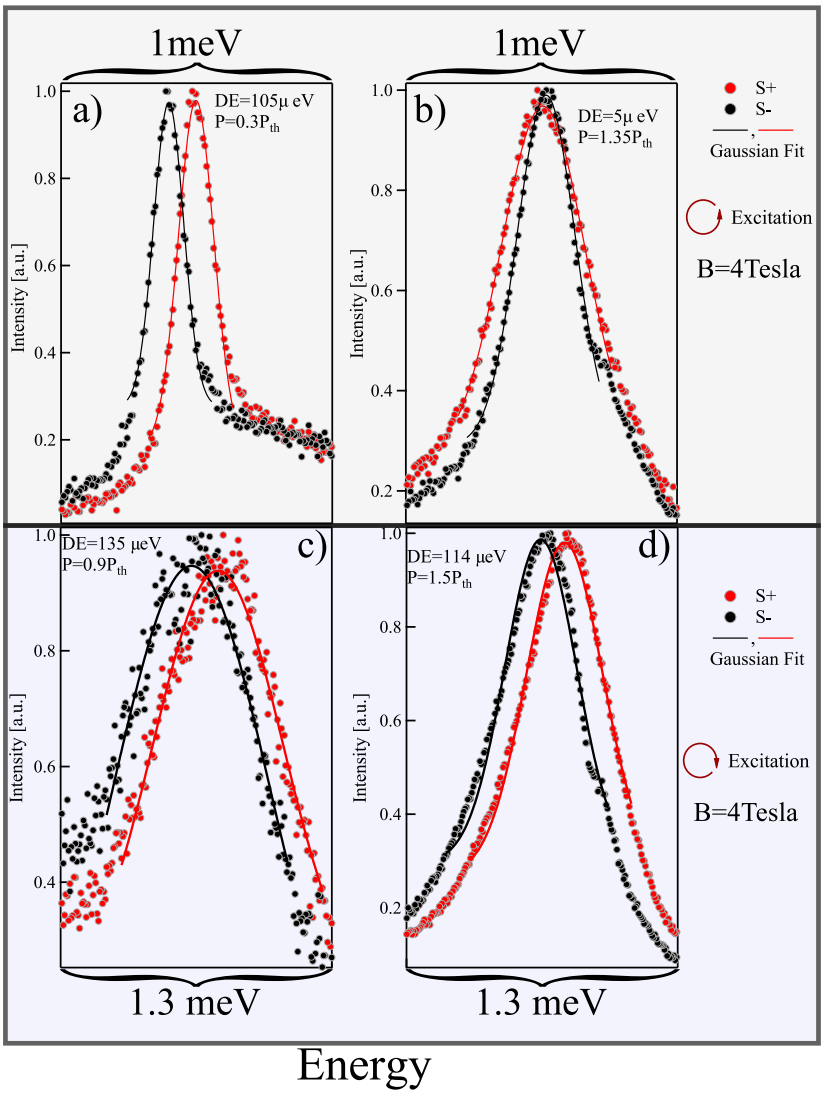

FIGURE 8.4: Spectra of $S+$ (red dots) and $S-$ (black dots) of the lower polariton branch at k=0 for a magnetic field of 4 Tesla for left-handed circular polarisation (a,b) and for right-handed circular polarisation (c,d) below and above threshold. Red and black lines are Gaussian fits to the data.

The variation of the Zeeman splitting for increasing power density for left handed excitation polarisation are shown in fig. 8.5 and for right handed circular polarisation are shown in are shown in fig. 8.6 .

The observed behaviour confirms the suppression of Zeeman splitting for increasing polariton density even below threshold while also clearly demonstrating that the polarization of the excitation can serve so as to counter balance or reinforce the spin-Meissner effect. As the polariton population is increased towards condensation threshold, the initially optically created polarized population will quickly scatter to the condensate state with spin preserving processes. This will result in a strong blue-shift of one of the two spin states, effectively reducing or augmenting the Zeeman splitting at threshold and modulating the critical magnetic field [223].

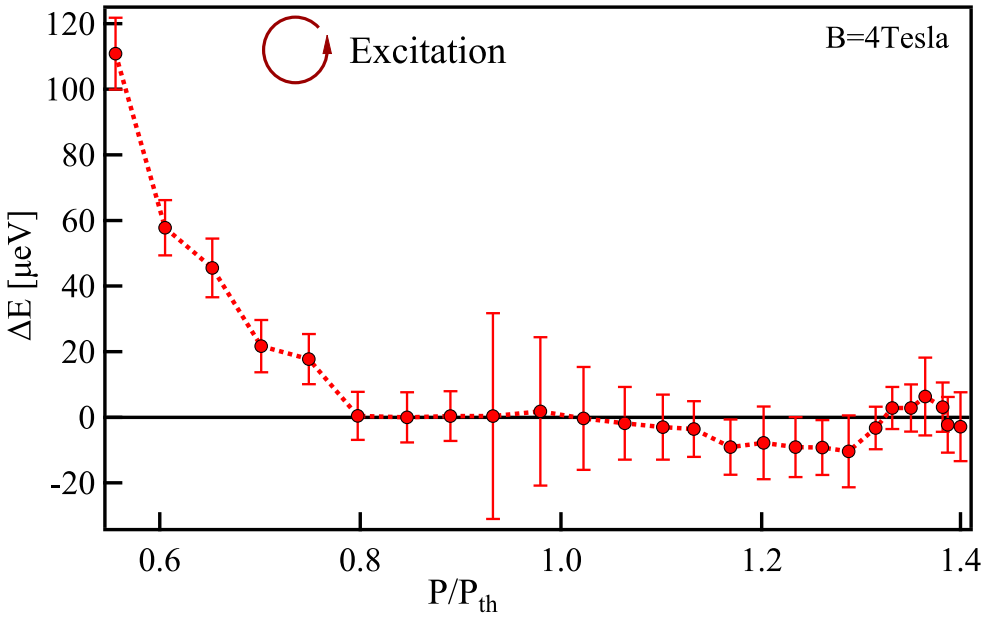

FIGURE 8.5: Polariton Zeeman splitting st k=0 as a function of threshold power density for B=4 Tesla under excitation with left-handed circular polarisation

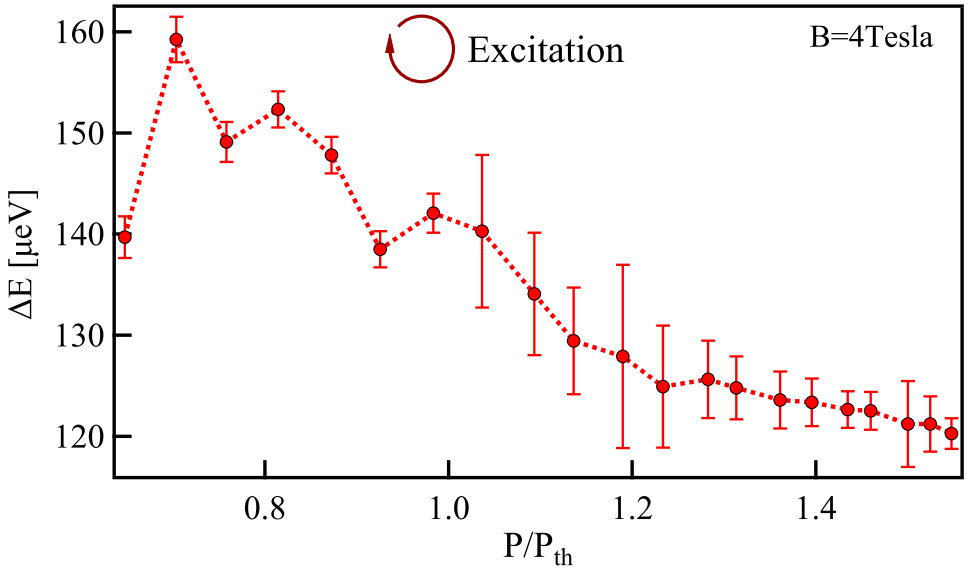

FIGURE 8.6: Polariton Zeeman splitting st k=0 as a function of threshold power density for B=4 Tesla under excitation with right-handed circular polarisation

8.3 Discussion

The polarization modulation of the critical magnetic field demonstrates that the polarization of polariton injection and the magnetic field can be a significant tool in tailoring the polariton condensate spin spectrum. As fast modulation of the polarization is possible with liquid crystals optics a fast switching between circularly and linearly polarised condensates can thus be engineered. Moreover, since at the critical magnetic field the superfluid nature of the condensate is predicted to be

suppressed, the excitation polarization at magnetic fields close to this critical magnetic field can be effectively used as a switch between the superfluid and quantum fluid regimes.

CHAPTER 9

Phase Diagrams of Polaritons in Magnetic Fields

9.1 Threshold modulation with magnetic fields

Clearly, microcavities present a unique laboratory rich in complex many-body processes, where fermionic and bosonic quasi-particles (electrons, holes, excitons and exciton-polaritons) co-exist and interact giving rise to new phases or pseudo-phases [229]. Magnetic fields are an efficient tool for switching between some of these phases, making use of the magnetic field sensitivity of both the internal structure and motion of excitons [230]. Here we present a detailed study of the magnetic field effect on the threshold modification of bosonic lasing in microcavities. So far, polariton lasers are the only existing example of bosonic lasers [231], where coherent light is emitted spontaneously from a bosonic condensate [232]. Magnetic fields was recently shown to be instrumental for the achievement of polariton lasing in electrically pumped microcavities through the enhancement of the exciton oscillator strength [24].

Charged particles in semiconductor microcavities, under the influence of magnetic fields, are bound to their cyclotron orbits, while polaritons being electrically neutral are allowed to move freely in the plane. In the dynamic equilibrium regime, under non-resonant CW excitation, electrons and holes are also abundantly created in the cavity medium before eventually forming excitons. In this section we demonstrate how magnetic fields strongly affect the phase diagram of this mixed Bose-Fermi system, switching between incoherent emission and bosonic lasing regimes in planar microcavities with non-resonant optical pumping.

We perform a series of power-dependence continuous wave excitation measurements for a range of magnetic fields, from 0T to 7T with 0.5T incremental steps. The magnet is oriented in the Faraday geometry and a description of the setup can be found in chapter 3 (see section 3.2.5.1 for a description of the setup). From the power dependent measurements we extract the threshold excitation density where we observe the onset of the non-linear response of the system. In fig. 9.1 the threshold power density for each magnetic field measurement is displayed normalised respectively to the threshold density in the absence of the external magnetic field. For fields of up to 3.5T the effect on the threshold is marginal. From 4T onwards the picture is quite different as the threshold quickly diverges with the applied field and for 7T is almost 1.8 times the original polariton threshold.

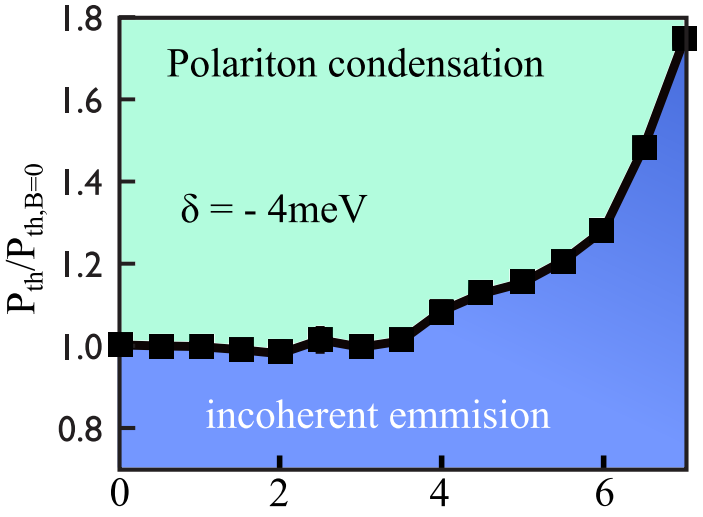

FIGURE 9.1: Polariton condensation threshold modulation with increasing magnetic field for 40μm

9.1.1 Theoretical treatment

These results can be interpreted by the interplay of the magnetic field induced exciton Bohr radius shrinkage and field-controlled diffusion of electrons, holes and excitons. The coherent polariton state within our model is formed during the three-stage process illustrated schematically in fig. 9.2. The first stage is the non-resonant pumping of electrons and holes with high values of wave vectors; the second stage is the energy relaxation of charged carriers followed by the formation of an exciton reservoir, and the final stage is the formation of polaritons followed by their resonant scattering to the ground state of the condensate. The first two processes can be described by the following set of dynamical diffusion equations:

$$\frac{\partial}{\partial t}n_e = D_e\Delta n_e - wn_en_h + J_e \tag{9.1}$$

$$\frac{\partial}{\partial t}n_h = D_h\Delta n_h - wn_en_h + J_h \tag{9.2}$$

$$\frac{\partial}{\partial t}n_{ex} = D_{ex}\Delta n_{ex} + wn_en_h - \frac{n_{ex}}{\tau_{ex}} \tag{9.3}$$

Here n_e, n_h and n_{ex} are the densities of electrons, holes and excitons, respectively, D_e, D_h, D_{ex} are the diffusion coefficients, w describes the exciton formation rate, J_e and J_h are the pump rates for electrons and holes and τ_{ex} is the exciton lifetime. The formation of excitons in our model is described by the term wn_en_h. Since in a strong coupling regime non-radiative losses are negligible, we assume that excitons decay mainly due to radiative processes, so that τ_{ex} corresponds to the radiative lifetime.

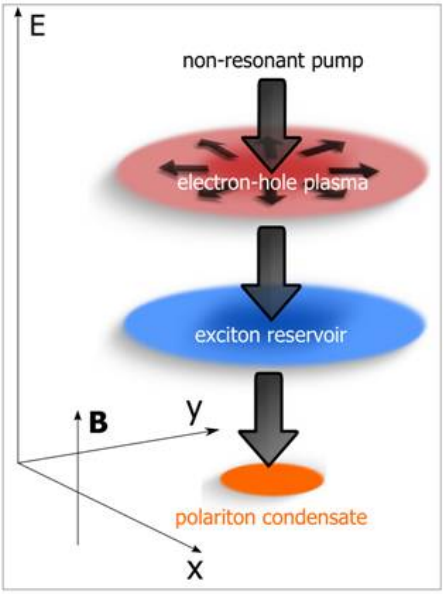

FIGURE 9.2: Schematic representation of condensate formation under non-resonant pumping. The excitation creates electron and holes which then form excitons that couple to the light field and scatter into the polariton ground state forming the condensate.

In order to describe the condensate formation, eq. 9.3 should be supplemented with the a term to account for scattering from the reservoir into the condensed state:

$$\frac{\partial}{\partial t}n_{ex} = D_{ex}\Delta n_{ex} + wn_en_h - \frac{n_{ex}}{\tau_{ex}} - \Gamma^{in}\left(|\psi_+|^2 + |\psi_-|^2\right)n_{ex} \tag{9.4}$$

where Γ^{in} is the transition rate from the reservoir to the condensate. The equations for the condensate spin wavefunctions $\psi_\pm$ are:

$$i\hbar\frac{\partial\psi_{\pm}}{\partial t}+\frac{\hbar^2\nabla^2}{2m_p}\psi_{\pm}=-\frac{i\hbar}{2\tau_c}\psi_{\pm}+\left(a_1\left|\psi_{\pm}\right|^2+a_2\left|\psi_{\mp}\right|^2\pm\frac{\Delta z}{2}\right)\psi_{\pm}+\frac{i\hbar}{2}\Gamma^{in}n_{ex}\psi_{\pm} \quad (9.5)$$

Here m_p is the effective mass of a polariton at zero wave vector, τ_c is the lifetime of the condensate, Δz is the Zeeman splitting and $a_{1,2}$ are the polariton-polariton interaction constants for the parallel and anti-parallel spin configurations. In the present equations, the variation of the drift terms, arising from the different spatial distribution of electrons and holes due to the possible difference in the diffusion coefficients D_e,D_h is neglected. For the exciton reservoir we set the onset of polariton lasing at $n_x = n_x^{(th)}$, where $n_x^{(th)}$ is a critical exciton concentration corresponding to the population of polariton ground state equal to unity. In the following we assume that the electron and hole components are pumped with equal rates by the Gaussian-shaped laser beam, $J_e = J_h = J(r) \equiv J_0 \exp -r^2/R^2$ where R defines the radius of the pump spot. The absence of the drift currents implies equal concentrations for electrons and holes, $n_e = n_h \equiv n$, satisfying the following equation in the stationary limit:

$$D\Delta n - wn^2 + J(r) = 0 \quad (9.6)$$

Non-linear eq. 9.5 can be solved numerically, however a simple variational procedure with the carrier density taken in the form $n(r) = n_0 \exp(-r^2/a^2)$, where a is the spread of carrier density, gives a good approximation preserving all the physical insight. Moreover, there are two limiting cases for eq. 9.6. The first corresponds to a low density pumping regime: in that case one deals with low concentrations and the non-linear term in eq. 9.6 is negligible. The effective lifetime of a particle is then $\tau = \frac{1}{wn_0}$, and the spread of carrier density is $a = \sqrt{D\tau}$. Integration of eq. 9.6 over the space domain gives: $a = \frac{D}{R\sqrt{wJ}}$. This effective radius obviously should be greater than the radius of the pump spot, R, so that $a \gg R$. Neglecting excitonic diffusion, the excitonic density at r = 0 is $n_{ex}(0) = wn_0^2\tau_{ex}$ and it behaves quadratically with the pump intensity:

$$n_{ex}^{lowpump}(0) \propto \frac{wR^4}{2D^2}J^2\tau_e x = \frac{J^2}{J^*}\tau_{ex}, \qquad J^* = 2D^2/(wR^4) \quad (9.7)$$

In the opposite case of a high pumping regime, we can neglect the diffusion term in eq. 9.6 resulting in a very short, linear in pump, expression for the exciton density.

$$n_{ex}^{highpump}(0) = J\tau_{ex} \quad (9.8)$$

Since the transition between the discussed regimes is defined by J^* which is inversely proportional to the fourth power of R, one should expect that the excitonic density distribution dependence on the pump power with and without a magnetic field significantly depends on the excitation spot radius. Application of a magnetic field alters parameters D and $\tau_{ex}x$ as it leads to suppression of the diffusion of charged carriers which can be described using the Einstein relation and the Hall expression for conductivity:

$$D(B) = \frac{k_B T \mu_0 / e}{1 + B^2/B_0^2}, B_0 = c/\mu_0 \tag{9.9}$$

Where $\mu_0 = (e\tau_p)/m$ is the mobility of the electron/hole gas for $B = 0$ and T is the gas temperature. Excitonic lifetime decreases with the magnetic field due to the decrease of the exciton Bohr radius ($\tau_x \propto a_B^2$ in 2D structures [233],) and this dependence has been analysed variationally in Ref. [221] . The radiative life-time is inversely proportional to the exciton oscillator strength. Its dependence on the magnetic field can be approximated by a Lorentzian:

$$\tau_x(B) = \frac{\tau_0}{1 + B^2/B_1^2} \tag{9.10}$$

with B_1 significantly greater than B_0. It becomes obvious now,that for the low pumping regime, $n_{ex}(0) \propto \frac{\tau_{ex}(B)}{D^2(B)}$ which (in the case of $B_1 > B_0$) results in the enhancement of exciton formation at r=0. Further, since parameter J^* depends on the magnetic field via the diffusion coefficient, the magnetic field acts as a switch between the two regimes leading to a non-monotonous behaviour of the excitonic density as illustrated in Fig. 9.4.

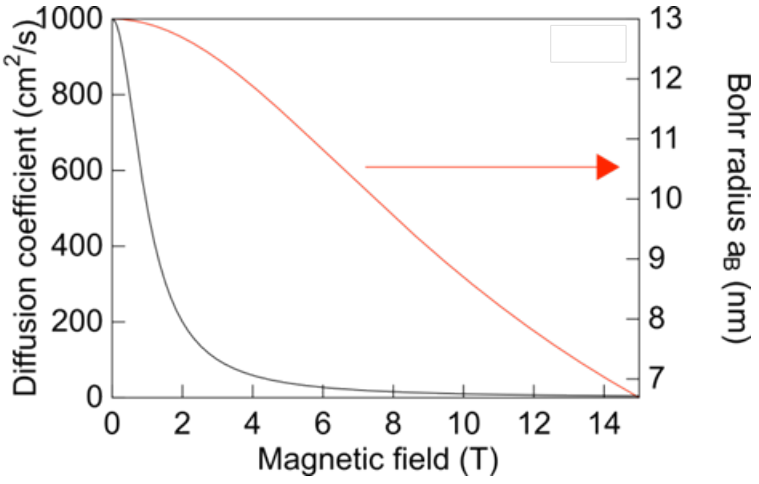

FIGURE 9.3: Bohr radius and diffusion coefficient dependences on magnetic field as used in calculations

9.1.2 Dependence on focusing of excitation

By varying the optical excitation size, a behaviour consistent with the previous theoretical interpretation is observed. These additional experimental measurements were performed on the same microcavity sample by two collaborating laboratories, namely, the Spin Optics Laboratory of St. Petersburg State university of Russia and the Institut Néel in Grenoble France. The polariton lasing threshold was again strongly sensitive to the magnetic field but also to the size of the excitation spot, as the phase diagrams of fig. 9.4 show. For a $10\mu m$ (FWHM) spot size, the threshold depends on the field non-monotonically (fig. 9.4a). For larger spots a steady and monotonic increase with magnetic field is recovered (fig. 9.4b,c). This behaviour is consistent with the kinetic model which predicts a qualitatively similar dependence of the threshold of the magnetic field. At zero fields, the exciton concentration is strongly diluted by carrying diffusion if the pump spot is narrow. On the other hand, for large spots, the diffusion has a marginal effect on the exciton concentration, which is why the suppression of diffusion by a magnetic field does not affect the threshold of polariton lasing so strongly. The threshold increase with a magnetic field observed for all spot sizes is again due to the shrinkage of the exciton Bohr radius. The predictions of the previous simple theoretical model deviate from the data, especially for the small spot sizes. This may be caused by a multitude of many-body effects in the complex Bose-Fermi system we study. One can mention, in particular, the repulsion of exciton-polaritons from the exciton reservoir and the electron-hole plasma.

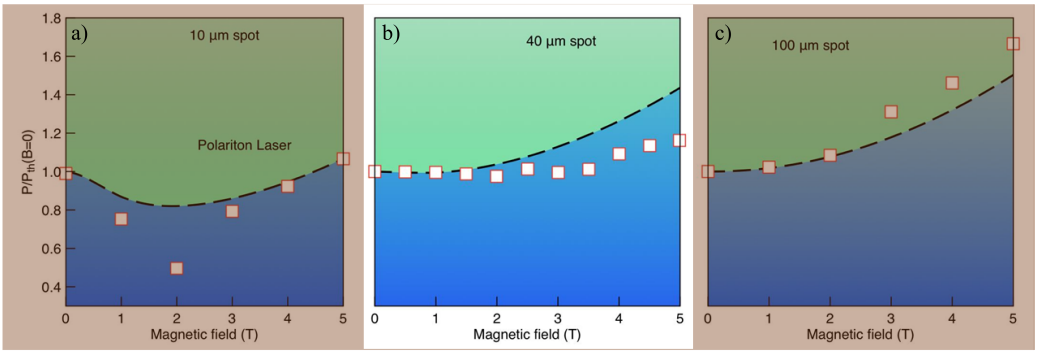

FIGURE 9.4: Polariton condensation threshold modulation with increasing magnetic field for a) 10μm, b) 40μm c) 100μm (FWHM) spot size. Open squares are experimental measurements. Dashed curves correspond to the theoretical calculation of the phase diagram. Figures a) and c) were measured in the Spin Optics Laboratory in St. Petersburg Russia and Institut Néel, CNRS/UJF 25 in Grenoble France respectively

The values used in the simulation of the phase transitions of fig. 9.4 are: $D_0 = 900cm^2/s, B_0 = 1T, B = 7T, w = 1cm^2/s, n_{th} = 3 \times 10^9 cm^{-2}$, while previous reports of the experimental values for w found in literature are $w \geq 0.5cm^2/s$ [234]

The model described here has also been utilised to describe the transition to photon lasing in pillar and planar samples with excellent qualitative agreement [235].

9.2 Conclusion

In conclusion, the polariton and photon lasing thresholds were shown to depend strongly on magnetic field. Particularly, the suppression of charged carrier diffusion may lead to reduction of the polariton lasing threshold. For comparison, photon lasing in the presence of a magnetic field was studied in the same samples, and is governed by the excitonic Mott transition. All the observed experimental features are described within a uniform model based on coupled diffusion equations for electrons, holes and excitons and the Gross-Pitaevskii equation for exciton-polariton condensates. Our results manifest a high potentiality of low threshold polariton lasers for spin-based logic applications

Disclaimer:

The theoretical model and the simulations are the work of M. Durnev, I. Savenko, T.C.H. Liew and I. Shelykh conducted for the collaborative study of ref. [235]

Conclusions and Outlook

Conclusions and Perspectives

The inherent non-linearities of semiconductor microcavities operating in the strong coupling regime offer an ideal laboratory for studying and harnessing light-matter interactions in the micro and nano scale. The light mass of these two-dimensional quasi-particles part is inherited from the "heavy" cavity photons while their interaction strength, that can be fine tuned by the exciton-cavity detuning, originates from their matter component. The perfection of semiconductor growth techniques has made possible the realisation of state of the art structures with increased photon lifetime, even up to 100ps [186], enabling the thermalisation of particles. This allows for the spontaneous appearance of a BEC phase transition in the system driven by stimulated occupation of the ground state [20]. This phase transition has been reported for a wide range of temperatures from 4K for CdTe and GaAs based structures up to room temperature for GaN structures and even as high as 353K for ZnO [236] allowing for experimental studies of the rich physics of coherent quantum ensembles in cryogenic configurations. Robust malleability of the potential landscape in these structures by optical means, demonstrated in 2010 [132], further highlights the flexibility of the system and has triggered the realisation of a plethora of highly interesting phenomena [133, 167, 196, 237].

Summary of experimental results

This thesis presents an experimental investigation of polariton condensation under two-dimensional optically induced confinement. The reduced dimensionality of the system theoretically dictates that a true BEC phase transition can only be observed when the density of states is modulated by a trapping potential. This theoretical

understanding in addition to previous demonstrations of robust potential formation by optical means provided the motivation for fulfilling these experiments.

Polariton condensation facilitated by the presence of an optical potential has thus been demonstrated in chapter 4, where a density dependent non-linearity was demonstrated. A Gaussian shaped condensate was formed and its coherence features probed through energy tomography and interferometric measurements. Moreover, as was shown, efficient trapping of particles significantly reduces the density required for the emergence of a coherent state. This is also accomplished due to efficient ground state relaxation inside the trap. A comparative study with an "unconfined" condensate revealed notably different spectral features between the two cases. This discrepancy is attributed to the suppression of interactions with uncondensed, incoherent particles with high kinetic energies that are present around the pumping region. This de-localisation of the condensate and the excitonic reservoir allows for the formation of a condensate with well defined quantum features.

In chapter 5 the dependence on the geometrical properties of the trap was probed. Non-ground state condensation defined by the potential size and ellipticity in a pure quantum state was demonstrated. The physical mechanism responsible for the state selectivity under non-local pumping was introduced and successfully employed to explain dynamic as well as steady state transitions. The study of the dynamic transition documented the presence of coherent tunnelling modes propagating outside the trap, with an intensity consistently tunable by the dynamic relaxation of the potential barriers. A generalised Gross-Pitaevski model, that was previously used to describe one-dimensional polariton confinement was extended to this two-dimensional case with remarkable consistency with the observed results.

The intriguing spin properties of the ground state system were examined in chapter 6. The presence of the trap was found to facilitate preferential condensation in one of the two polariton spin components under the influence of marginally small imbalances in the injection of carriers, introduced by the tight focus of the excitation. A dependence on the spin selectivity was demonstrated by the modulation of the angle of the linear polarisation of the optical excitation beam. Strong dependence on the density of the condensate was also observed and attributed to coherent Josephson coupling between the two spinor states while experimental simulations qualitatively and quantitatively reproduced the observed effect.

The optical trap configuration was finally studied greatly above condensation threshold. Time integrated dispersion imaging under pulsed excitation revealed a linearisation of the polariton dispersion in the high density regime. However, careful examination of the observed features in the transient domain disproved the association of these feature with the Bogoliubov excitation spectrum. Transient relaxation from photon lasing and Δk narrowing for relaxation inside the optical

trap are sufficient to explain these features, which raises the question for previous demonstrations under similar conditions.

The optical potential studied was imprinted by optical means and defined by the finite diffusion of carriers around the pumping region. Modulation of diffusion can thus be an important factor in defining the geometry of the trap and in extension of the resulting quantum state. In chapter 8 details the results of a study on the magnetic field mediated threshold modulation in polariton condensates. The results demonstrate that for the application of an external magnetic field perpendicular to the cavity growth axis a drastic modulation of the condensation threshold takes place. Although this effect is exacerbated for tight focused optical excitation it is also observable for excitation sizes up to $100\mu m$. This effect originates from the finite diffusion length of injected carriers outside the excitation region. The presence of the magnetic field quenches the diffusion length of the reservoir which in turn modulates the required threshold density.

Future Work and Perspectives

The experimental results described here open the way for a number of fascinating prospects in the field of polariton condensates both in terms of the study of the rich underlying physics as well as towards the realisation of novel devices. The separation of the condensate with the excitonic reservoir filters out the strong exciton-polariton interactions so that intra polariton interactions can be more effectively studied and characterised.

A current direction in the field is the formation of polariton condensate lattices that can interact through dissipative coupling [238] with the implicit goal of creating quantum simulators [239]. However another possibility for the implementation of this scheme can now be envisaged. With the use of a spatial light modulator multiple trapping potentials in a lattice form can be imprinted. This would allow for controllable tunnelling assisted coherent coupling between neighbouring condensates by controlling the intensity of the individual barriers. In lattice condensates, tuning of the coupling is accomplished by changing the lattice constant and bringing the individual nodes closer. In the proposed confined condensate lattice configuration the inherent advantage lies in that the dimensionality need not be altered in order to tune the coupling. Moreover, the coupling between individual neighbours can be individually controlled and this enormously augments the flexibility and potentiality of this proposed system. Non-ground state condensation is an additional degree of freedom here as is the spin of the system.

Bibliography

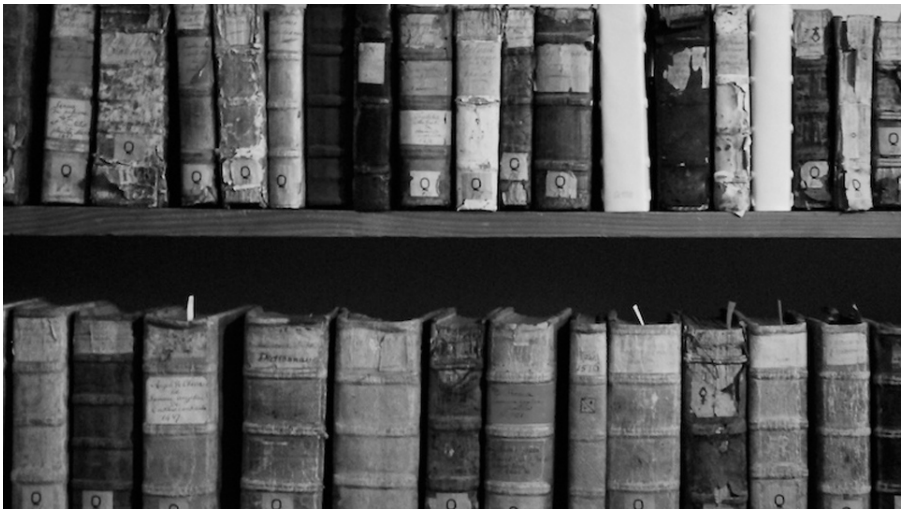

Bibliography

[1] Busch, G. Early history of the physics and chemistry of semiconductors-from doubts to fact in a hundred years. *European Journal of Physics* **10**, 254 (1989). URL http://iopscience.iop.org/0143-0807/10/4/002.

[2] Hirshfeld, A. *The Electric Life of Michael Faraday* (Bloomsbury, 2006). URL http://www.bloomsbury.com/us/the-electric-life-of-michael-faraday-9780802714701/.

[3] Gorton, W. The genesis of the transistor. *Proceedings of the IEEE* **86**, 50–52 (1998).

[4] Ross, I. The invention of the transistor. *Proceedings of the IEEE* **86**, 7–28 (1998).

[5] Maiman, T. H. Stimulated optical radiation in ruby. *Nature* **187**, 493–494 (1960). URL http://www.nature.com/nature/journal/v187/n4736/abs/187493a0.html.

[6] Hall, R. N., Fenner, G. E., Kingsley, J. D., Soltys, T. J. & Carlson, R. O. Coherent Light Emission From GaAs Junctions. *Physical Review Letters* **9**, 366–368 (1962). URL http://link.aps.org/doi/10.1103/PhysRevLett.9.366.

[7] Soda, H., Iga, K.-i., Kitahara, C. & Suematsu, Y. /InP Surface Emitting Injection Lasers. *Japanese Journal of Applied Physics* **18**, 2329 (1979). URL http://iopscience.iop.org/1347-4065/18/12/2329.

[8] Hopfield, J. J. Theory of the Contribution of Excitons to the Complex Dielectric Constant of Crystals. *Physical Review* **112**, 1555–1567 (1958). URL http://link.aps.org/doi/10.1103/PhysRev.112.1555.

[9] Oka, Y. & Cardona, M. Resonance Raman scattering of excitonic polaritons by LO and acoustic phonons in ZnTe. *Solid State Communications* **30**, 447–451 (1979). URL http://www.sciencedirect.com/science/article/pii/0038109879911852.

[10] Tuffigo, H., Cox, R. T., Magnea, N., d'Aubigné, Y. M. & Million, A. Luminescence from quantized exciton-polariton states in $Cd_{1-x}Zn_xTe$/CdTe/$Cd_{1-x}Zn_xTe$ thin-layer heterostructures. *Physical Review B* **37**, 4310–4313 (1988). URL http://link.aps.org/doi/10.1103/PhysRevB.37.4310.

[11] Weisbuch, C., Nishioka, M., Ishikawa, A. & Arakawa, Y. Observation of the coupled exciton-photon mode splitting in a semiconductor quantum microcavity. *Physical Review Letters* **69**, 3314–3317 (1992). URL http://link.aps.org/doi/10.1103/PhysRevLett.69.3314.

[12] Imamoglu, A., Ram, R. J., Pau, S. & Yamamoto, Y. Nonequilibrium condensates and lasers without inversion: Exciton-polariton lasers. *Physical Review A* **53**, 4250–4253 (1996). URL http://link.aps.org/doi/10.1103/PhysRevA.53.4250.

[13] Savvidis, P. G. *et al.* Angle-Resonant stimulated polariton amplifier. *Physical Review Letters* **84**, 1547–1550 (2000). URL http://link.aps.org/doi/10.1103/PhysRevLett.84.1547.

[14] Saba, M. *et al.* High-temperature ultrafast polariton parametric amplification in semiconductor microcavities. *Nature* **414**, 731–735 (2001). URL http://www.nature.com/nature/journal/v414/n6865/full/414731a.html?free=2.

[15] Bose. Plancks Gesetz und Lichtquantenhypothese. *Zeitschrift für Physik* **26**, 178–181 (1924). URL http://link.springer.com/article/10.1007/BF01327326.

[16] Einstein, A. Quantentheorie des einatomigen idealen gases. *Sitzungsberichte / Physikalische Klasse, Preussische Akademie der Wissenschaften* **ii** (1925).

[17] Anderson, M. H., Ensher, J. R., Matthews, M. R., Wieman, C. E. & Cornell, E. A. Observation of Bose-Einstein condensation in a dilute atomic vapor. *Science* **269**, 198 –201 (1995). URL http://www.sciencemag.org/content/269/5221/198.abstract.

[18] Davis, K. B. *et al.* Bose-Einstein Condensation in a Gas of Sodium Atoms. *Physical Review Letters* **75**, 3969–3973 (1995). URL http://link.aps.org/doi/10.1103/PhysRevLett.75.3969.

[19] Cornell, E. A. & Wieman, C. E. Nobel Lecture: Bose-Einstein condensation in a dilute gas, the first 70 years and some recent experiments. *Reviews of Modern Physics* **74**, 875–893 (2002). URL http://link.aps.org/doi/10.1103/RevModPhys.74.875.

[20] Kasprzak, J. *et al.* Bose-Einstein condensation of exciton polaritons. *Nature* **443**, 409–14 (2006). URL http://dx.doi.org/10.1038/nature05131.

[21] Christopoulos, S. *et al.* Room-temperature polariton lasing in semiconductor microcavities. *Physical Review Letters* **98**, 126405 (2007). URL http://link.aps.org/doi/10.1103/PhysRevLett.98.126405.

[22] Deveaud-Plédran, B. Solid-state physics: Polaritronics in view. *Nature* **453**, 297–298 (2008). URL http://www.nature.com/nature/journal/v453/n7193/full/453297a.html.

[23] Tsintzos, S. I., Pelekanos, N. T., Konstantinidis, G., Hatzopoulos, Z. & Savvidis, P. G. A GaAs polariton light-emitting diode operating near room temperature. *Nature* **453**, 372–375 (2008). URL http://www.nature.com/nature/journal/v453/n7193/full/nature06979.html.

[24] Schneider, C. *et al.* An electrically pumped polariton laser. *Nature* **497**, 348–352 (2013). URL http://www.nature.com/nature/journal/v497/n7449/full/nature12036.html.

[25] Bhattacharya, P., Xiao, B., Das, A., Bhowmick, S. & Heo, J. Solid State Electrically Injected Exciton-Polariton Laser. *Physical Review Letters* **110**, 206403 (2013). URL http://link.aps.org/doi/10.1103/PhysRevLett.110.206403.

[26] Bhattacharya, P. *et al.* Room Temperature Electrically Injected Polariton Laser. *Physical Review Letters* **112**, 236802 (2014). URL http://link.aps.org/doi/10.1103/PhysRevLett.112.236802.

[27] Žutić, I., Fabian, J. & Das Sarma, S. Spintronics: Fundamentals and applications. *Reviews of Modern Physics* **76**, 323–410 (2004). URL http://link.aps.org/doi/10.1103/RevModPhys.76.323.

[28] Mott, N. F. The Electrical Conductivity of Transition Metals. *Proceedings of the Royal Society of London A: Mathematical, Physical and Engineering Sciences* **153**, 699–717 (1936). URL http://rspa.royalsocietypublishing.org/content/153/880/699.

[29] Paraïso, T. K., Wouters, M., Léger, Y., Morier-Genoud, F. & Deveaud-Plédran, B. Multistability of a coherent spin ensemble in a semiconductor microcavity. *Nature Materials* **9**, 655–660 (2010). URL http://www.nature.com/nmat/journal/v9/n8/abs/nmat2787.html.

[30] Savona, V. Linear optical properties of semiconductor microcavities with embedded quantum wells. In Benisty, H. *et al.* (eds.) *Confined Photon Systems*, no. 531 in Lecture Notes in Physics, 173–242 (Springer Berlin Heidelberg, 1999). URL http://link.springer.com/chapter/10.1007/BFb0104383.

[31] Coldren, L. A., Corzine, S. W. & Mašanović, M. L. *Diode Lasers and Photonic Integrated Circuits, Second Edition* (Wiley, 2012). URL http://onlinelibrary.wiley.com/book/10.1002/9781118148167.

[32] Savona, V., Andreani, L. C., Schwendimann, P. & Quattropani, A. Quantum well excitons in semiconductor microcavities: Unified treatment of weak and strong coupling regimes. *Solid State Communications* **93**, 733–739 (1995). URL http://www.sciencedirect.com/science/article/pii/0038109894008655.

[33] Babic, D. I. & Corzine, S. Analytic expressions for the reflection delay, penetration depth, and absorptance of quarter-wave dielectric mirrors. *IEEE Journal of Quantum Electronics* **28**, 514–524 (1992).

[34] Benisty, H., De Neve, H. & Weisbuch, C. Impact of planar microcavity effects on light extraction-Part I: basic concepts and analytical trends. *IEEE Journal of Quantum Electronics* **34**, 1612–1631 (1998).

[35] Fowles, G. R. *Introduction to modern optics*. Dover books on physics (Dover Publications, New York, 1989), 2 edn. URL http://store.doverpublications.com/0486659577.html.

[36] Yariv, A. *Quantum electronics* (John Wiley and sons, New Jersey, 1988), 3 edn. URL http://eu.wiley.com/WileyCDA/WileyTitle/productCd-0471609978.html.

[37] Wannier, G. H. The Structure of Electronic Excitation Levels in Insulating Crystals. *Physical Review* **52**, 191–197 (1937). URL http://link.aps.org/doi/10.1103/PhysRev.52.191.

[38] Diouri, J., Taqi, A., Haddad, A. E., Katih, M. & Feddi, E. Parametrized equations for excitons in two-dimensional semiconductor quantum wells with arbitrary potential profiles. *Semiconductor Science and Technology* **18**, 377 (2003). URL http://iopscience.iop.org/0268-1242/18/4/331.

[39] Kavokin, A. V., Baumberg, J., Malpuech, G. & Laussy, F. P. *Microcavities* (Oxford Univ. Press, Oxford, 2007).

[40] Kavokin, A. V. Exciton oscillator strength in quantum wells: From localized to free resonant states. *Physical Review B* **50**, 8000–8003 (1994). URL http://link.aps.org/doi/10.1103/PhysRevB.50.8000.

[41] Kroemer, H. *Quantum Mechanics: For Engineering, Materials Science, and Applied Physics* (Prentice Hall, 1994).

[42] Purcell, E. M. Spontaneous emission probabilities at radio frequencies. *Physical Review* **69**, 681 (1946). URL http://link.aps.org/doi/10.1103/PhysRev.69.674.2.

[43] De Liberato, S. Light-Matter Decoupling in the Deep Strong Coupling Regime: The Breakdown of the Purcell Effect. *Physical Review Letters* **112**, 016401 (2014). URL http://link.aps.org/doi/10.1103/PhysRevLett.112.016401.

[44] Li, F. *et al.* From Excitonic to Photonic Polariton Condensate in a ZnO-Based Microcavity. *Physical Review Letters* **110**, 196406 (2013). URL http://link.aps.org/doi/10.1103/PhysRevLett.110.196406.

[45] Goldberg, D. *et al.* Exciton-lattice polaritons in multiple-quantum-well-based photonic crystals. *Nature Photonics* **3**, 662–666 (2009). URL http://www.nature.com/nphoton/journal/v3/n11/full/nphoton.2009.190.html.

[46] Askitopoulos, A. *et al.* Bragg Polaritons: Strong Coupling and Amplification in an Unfolded Microcavity. *Physical Review Letters* **106**, 076401 (2011). URL http://link.aps.org/doi/10.1103/PhysRevLett.106.076401.

[47] Winkler, R. *Spin-orbit Coupling Effects in Two-Dimensional Electron and Hole Systems* (Springer, 2003). URL http://www.springer.com/materials/optical+%26+electronic+materials/book/978-3-540-01187-3.

[48] Pauli, W. The Connection Between Spin and Statistics. *Physical Review* **58**, 716–722 (1940). URL http://link.aps.org/doi/10.1103/PhysRev.58.716.

[49] Pethick, C. J. & Smith, H. *Bose-Einstein Condensation in Dilute Gases* (Cambridge University Press, 2001).

[50] Bradley, C. C., Sackett, C. A., Tollett, J. J. & Hulet, R. G. Evidence of Bose-Einstein condensation in an atomic gas with attractive interactions. *Physical Review Letters* **75**, 1687–1690 (1995). URL http://link.aps.org/doi/10.1103/PhysRevLett.75.1687.

[51] Malpuech, G., Rubo, Y. G., Laussy, F. P., Bigenwald, P. & Kavokin, A. V. Polariton laser: thermodynamics and quantum kinetic theory. *Semiconductor Science and Technology* **18**, S395–S404 (2003). URL http://iopscience.iop.org/0268-1242/18/10/314.

[52] Petrov, D. S., Gangardt, D. M. & Shlyapnikov, G. V. Low-dimensional trapped gases. *Journal de Physique IV (Proceedings)* **116**, 5–44 (2004). URL http://www.edpsciences.org/10.1051/jp4:2004116001.

[53] Mermin, N. D. & Wagner, H. Absence of Ferromagnetism or Antiferromagnetism in One- or Two-Dimensional Isotropic Heisenberg Models. *Physical Review Letters* **17**, 1307–1307 (1966). URL http://link.aps.org/doi/10.1103/PhysRevLett.17.1307.

[54] Kosterlitz, J. M. & Thouless, D. J. Ordering, metastability and phase transitions in two-dimensional systems. *Journal of Physics C: Solid State Physics* **6**, 1181 (1973). URL http://iopscience.iop.org/0022-3719/6/7/010.

[55] Nikuni, T., Oshikawa, M., Oosawa, A. & Tanaka, H. Bose-Einstein Condensation of Dilute Magnons in $TlCuCl_3$. *Physical Review Letters* **84**, 5868–5871 (2000). URL http://link.aps.org/doi/10.1103/PhysRevLett.84.5868.

[56] Eisenstein, J. P. & MacDonald, A. H. Bose–Einstein condensation of excitons in bilayer electron systems. *Nature* **432**, 691–694 (2004). URL http://www.nature.com/nature/journal/v432/n7018/full/nature03081.html.

[57] High, A. A. *et al.* Spontaneous coherence in a cold exciton gas. *Nature* **483**, 584–588 (2012). URL http://www.nature.com/nature/journal/v483/n7391/full/nature10903.html.

[58] Alloing, M. *et al.* Evidence for a Bose-Einstein condensate of excitons. *EPL (Europhysics Letters)* **107**, 10012 (2014). URL http://iopscience.iop.org/0295-5075/107/1/10012.

[59] Klaers, J., Schmitt, J., Vewinger, F. & Weitz, M. Bose-Einstein condensation of photons in an optical microcavity. *Nature* **468**, 545–548 (2010). URL http://www.nature.com/nature/journal/v468/n7323/full/nature09567.html.

[60] Schmitt-Rink, S., Chemla, D. S. & Miller, D. A. B. Theory of transient excitonic optical nonlinearities in semiconductor quantum-well structures. *Physical Review B* **32**, 6601–6609 (1985). URL http://link.aps.org/doi/10.1103/PhysRevB.32.6601.

[61] Moskalenko, S. A. & Snoke, D. *Bose Einstein Condensation of Excitons and Biexcitons And Coherent Nonlinear Optics with Excitons* (Cambridge University Press, 2000). URL http://goo.gl/PUhil9.

[62] Hulin, D., Mysyrowicz, A. & à la Guillaume, C. B. Evidence for Bose-Einstein Statistics in an Exciton Gas. *Physical Review Letters* **45**, 1970–1973 (1980). URL http://link.aps.org/doi/10.1103/PhysRevLett.45.1970.

[63] Butov, L. V., Lai, C. W., Ivanov, A. L., Gossard, A. C. & Chemla, D. S. Towards Bose–Einstein condensation of excitons in potential traps. *Nature* **417**, 47–52 (2002). URL http://www.nature.com/nature/journal/v417/n6884/full/417047a.html.

[64] Christmann, G. *et al.* Oriented polaritons in strongly-coupled asymmetric double quantum well microcavities. *Applied Physics Letters* **98**, 081111 (2011). URL http://scitation.aip.org/content/aip/journal/apl/98/8/10.1063/1.3559909.

[65] Miesner, H.-J. *et al.* Bosonic Stimulation in the Formation of a Bose-Einstein Condensate. *Science* **279**, 1005–1007 (1998). URL http://www.sciencemag.org/content/279/5353/1005.

[66] Dang, L. S., Heger, D., André, R., Bœuf, F. & Romestain, R. Stimulation of Polariton Photoluminescence in Semiconductor Microcavity. *Physical Review Letters* **81**, 3920–3923 (1998). URL http://link.aps.org/doi/10.1103/PhysRevLett.81.3920.

[67] Ciuti, C., Schwendimann, P., Deveaud, B. & Quattropani, A. Theory of the angle-resonant polariton amplifier. *Physical Review B* **62**, R4825–R4828 (2000). URL http://link.aps.org/doi/10.1103/PhysRevB.62.R4825.

[68] Stevenson, R. M. *et al.* Continuous Wave Observation of Massive Polariton Redistribution by Stimulated Scattering in Semiconductor Microcavities. *Physical Review Letters* **85**, 3680–3683 (2000). URL http://link.aps.org/doi/10.1103/PhysRevLett.85.3680.

[69] Baumberg, J. J. *et al.* Parametric oscillation in a vertical microcavity: A polariton condensate or micro-optical parametric oscillation. *Physical Review B* **62**, R16247–R16250 (2000). URL http://link.aps.org/doi/10.1103/PhysRevB.62.R16247.

[70] Deng, H., Weihs, G., Santori, C., Bloch, J. & Yamamoto, Y. Condensation of semiconductor microcavity exciton polaritons. *Science* **298**, 199–202 (2002). URL http://www.sciencemag.org/content/298/5591/199.

[71] Richard, M., Kasprzak, J., Romestain, R., André, R. & Dang, L. S. Spontaneous Coherent Phase Transition of Polaritons in CdTe Microcavities. *Physical Review Letters* **94**, 187401 (2005). URL http://link.aps.org/doi/10.1103/PhysRevLett.94.187401.

[72] Richard, M. *et al.* Experimental evidence for nonequilibrium Bose condensation of exciton polaritons. *Physical Review B* **72**, 201301 (2005). URL http://link.aps.org/doi/10.1103/PhysRevB.72.201301.

[73] Balili, R., Hartwell, V., Snoke, D., Pfeiffer, L. & West, K. Bose-Einstein condensation of microcavity polaritons in a trap. *Science* **316**, 1007 –1010 (2007). URL http://www.sciencemag.org/content/316/5827/1007.abstract.

[74] Nardin, G. *et al.* Dynamics of long-range ordering in an exciton-polariton condensate. *Physical Review Letters* **103**, 256402 (2009). URL http://link.aps.org/doi/10.1103/PhysRevLett.103.256402.

[75] Deng, H., Solomon, G. S., Hey, R., Ploog, K. H. & Yamamoto, Y. Spatial coherence of a polariton condensate. *Physical Review Letters* **99**, 126403 (2007). URL http://link.aps.org/doi/10.1103/PhysRevLett.99.126403.

[76] Ohadi, H. *et al.* Spontaneous Symmetry Breaking in a Polariton and Photon Laser. *Physical Review Letters* **109**, 016404 (2012). URL http://link.aps.org/doi/10.1103/PhysRevLett.109.016404.

[77] Penrose, O. & Onsager, L. Bose-Einstein Condensation and Liquid Helium. *Physical Review* **104**, 576–584 (1956). URL http://link.aps.org/doi/10.1103/PhysRev.104.576.

[78] Yang, C. N. Concept of Off-Diagonal Long-Range Order and the Quantum Phases of Liquid He and of Superconductors. *Reviews of Modern Physics* **34**, 694–704 (1962). URL http://link.aps.org/doi/10.1103/RevModPhys.34.694.

[79] Pitaevskii, L. P. & Stringari, S. *Bose-Einstein Condensation* (Clarendon Press | International Series of Monographs on Physics 116, 2003).

[80] Wouters, M. & Carusotto, I. Excitations in a Nonequilibrium Bose-Einstein Condensate of Exciton Polaritons. *Physical Review Letters* **99**, 140402 (2007). URL http://link.aps.org/doi/10.1103/PhysRevLett.99.140402.

[81] Wertz, E. *et al.* Propagation and Amplification Dynamics of 1d Polariton Condensates. *Physical Review Letters* **109**, 216404 (2012). URL http://link.aps.org/doi/10.1103/PhysRevLett.109.216404.

[82] Kapitza, P. Viscosity of liquid helium below the λ-point. *Nature* **141** (1938). URL http://www.nature.com/nphys/journal/v5/n11/full/nphys1364.html.

[83] Amo, A. *et al.* Collective fluid dynamics of a polariton condensate in a semiconductor microcavity. *Nature* **457**, 291–295 (2009). URL http://www.nature.com/nature/journal/v457/n7227/full/nature07640.html.

[84] Amo, A. *et al.* Superfluidity of polaritons in semiconductor microcavities. *Nature Physics* **5**, 805–810 (2009). URL http://www.nature.com/nphys/journal/v5/n11/full/nphys1364.html.

[85] Utsunomiya, S. *et al.* Observation of Bogoliubov excitations in exciton-polariton condensates. *Nature Physics* **4**, 700–705 (2008). URL http://www.nature.com/nphys/journal/v4/n9/full/nphys1034.html#a3.

[86] Assmann, M. *et al.* From polariton condensates to highly photonic quantum degenerate states of bosonic matter. *Proceedings of the National Academy of Sciences of the United States of America* **108**, 1804–1809 (2011). URL http://www.ncbi.nlm.nih.gov/pmc/articles/PMC3033249/.

[87] Kohnle, V. *et al.* From Single Particle to Superfluid Excitations in a Dissipative Polariton Gas. *Physical Review Letters* **106**, 255302 (2011). URL http://link.aps.org/doi/10.1103/PhysRevLett.106.255302.

[88] Kohnle, V. *et al.* Four-wave mixing excitations in a dissipative polariton quantum fluid. *Physical Review B* **86**, 064508 (2012). URL http://link.aps.org/doi/10.1103/PhysRevB.86.064508.

[89] Keeling, J. & Berloff, N. G. Spontaneous Rotating Vortex Lattices in a Pumped Decaying Condensate. *Physical Review Letters* **100**, 250401 (2008). URL http://link.aps.org/doi/10.1103/PhysRevLett.100.250401.

[90] Donnelly, R. J. *Quantized Vortices in Helium II* (Cambridge University Press, 1991).

[91] Lagoudakis, K. G. *et al.* Quantized vortices in an exciton–polariton condensate. *Nature Physics* **4**, 706–710 (2008). URL http://www.nature.com/nphys/journal/v4/n9/full/nphys1051.html#B3.

[92] Lagoudakis, K. G. *et al.* Observation of Half-Quantum Vortices in an Exciton-Polariton Condensate. *Science* **326**, 974–976 (2009). URL http://www.sciencemag.org/content/326/5955/974.

[93] Nardin, G. *et al.* Hydrodynamic nucleation of quantized vortex pairs in a polariton quantum fluid. *Nat Phys* **7**, 635–641 (2011). URL http://dx.doi.org/10.1038/nphys1959.

[94] Sanvitto, D. *et al.* Persistent currents and quantized vortices in a polariton superfluid. *Nature Physics* **6**, 527–533 (2010). URL http://www.nature.com/nphys/journal/v6/n7/full/nphys1668.html.

[95] Krizhanovskii, D. N. *et al.* Effect of Interactions on Vortices in a Nonequilibrium Polariton Condensate. *Physical Review Letters* **104**, 126402 (2010). URL http://link.aps.org/doi/10.1103/PhysRevLett.104.126402.

[96] Stegeman, G. I. & Segev, M. Optical spatial solitons and their interactions: Universality and diversity. *Science* **286**, 1518–1523 (1999). URL http://www.sciencemag.org/content/286/5444/1518.

[97] Segev, M. & Stegeman, G. Self-trapping of optical beams: Spatial solitons. *Physics Today* **51**, 42–48 (1998). URL http://link.aip.org/link/?PTO/51/42/1.

[98] Chen, Z., Segev, M. & Christodoulides, D. N. Optical spatial solitons: historical overview and recent advances. *New J. Phys.* **75**, 086401 (2012). URL http://iopscience.iop.org/0034-4885/75/8/086401.

[99] Hercher, M. Laser-induced damage in transparent media. *J. Opt. Soc. Am.* **54**, 563 (1964).

[100] Segev, M., Crosignani, B., Yariv, A. & Fischer, B. Spatial solitons in photorefractive media. *Phys. Rev. Lett.* **68**, 923–926 (1992). URL http://link.aps.org/doi/10.1103/PhysRevLett.68.923.

[101] Hayata, K. & Koshiba, M. Multidimensional solitons in quadratic nonlinear media. *Phys. Rev. Lett.* **71**, 3275–3278 (1993). URL http://link.aps.org/doi/10.1103/PhysRevLett.71.3275.

[102] Nakazawa, M. & Suzuki, K. 10 gbit/s pseudorandom dark soliton data transmission over 1200 km. *Electronics Letters* **31**, 1076–1077 (1995).

[103] Miller, P. D. Zero-crosstalk junctions made from dark solitons. *Phys. Rev. E* **53**, 4137–4142 (1996). URL http://link.aps.org/doi/10.1103/PhysRevE.53.4137.

[104] Sich, M. *et al.* Observation of bright polariton solitons in a semiconductor microcavity. *Nature Photonics* **6**, 50–55 (2012). URL http://www.nature.com/nphoton/journal/v6/n1/full/nphoton.2011.267.html.

[105] Sich, M. *et al.* Effects of Spin-Dependent Interactions on Polarization of Bright Polariton Solitons. *Physical Review Letters* **112**, 046403 (2014). URL http://link.aps.org/doi/10.1103/PhysRevLett.112.046403.

[106] Tsuzuki, T. Nonlinear waves in the pitaevskii-gross equation. *J. Low Temp. Phys.* **4**, 441–457 (1971). URL http://www.springerlink.com/content/w576565460h03131/abstract/.

[107] Kivshar, Y. Dark solitons in nonlinear optics. *J. Quantum. Electron.* **29**, 250–264 (1993).

[108] Denschlag, J. *et al.* Generating Solitons by Phase Engineering of a Bose-Einstein Condensate. *Science* **287**, 97–101 (2000). URL http://www.sciencemag.org/content/287/5450/97.

[109] Amo, A. *et al.* Polariton superfluids reveal quantum hydrodynamic solitons. *Science* **332**, 1167–1170 (2011). URL http://www.sciencemag.org/content/332/6034/1167.

[110] Grosso, G., Nardin, G., Morier-Genoud, F., Léger, Y. & Deveaud-Plédran, B. Soliton Instabilities and Vortex Street Formation in a Polariton Quantum Fluid. *Physical Review Letters* **107**, 245301 (2011). URL http://link.aps.org/doi/10.1103/PhysRevLett.107.245301.

[111] Grosso, G., Nardin, G., Morier-Genoud, F., Léger, Y. & Deveaud-Plédran, B. Dynamics of dark-soliton formation in a polariton quantum fluid. *Phys. Rev. B* **86**, 020509 (2012). URL http://link.aps.org/doi/10.1103/PhysRevB.86.020509.

[112] Hivet, R. *et al.* Half-solitons in a polariton quantum fluid behave like magnetic monopoles. *Nature Physics* **8**, 724–728 (2012). URL http://www.nature.com/nphys/journal/v8/n10/full/nphys2406.html.

[113] Deng, H., Weihs, G., Snoke, D., Bloch, J. & Yamamoto, Y. Polariton lasing vs. photon lasing in a semiconductor microcavity. *Proceedings of the National Academy of Sciences* **100**, 15318–15323 (2003). URL http://www.pnas.org/content/100/26/15318.

[114] Pigeon, S., Carusotto, I. & Ciuti, C. Hydrodynamic nucleation of vortices and solitons in a resonantly excited polariton superfluid. *Phys. Rev. B* **83**, 144513 (2011). URL http://link.aps.org/doi/10.1103/PhysRevB.83.144513.

[115] Zajac, J. & Langbein, W. Structure and zero-dimensional polariton spectrum of natural defects in GaAs/AlAs microcavities. *Phys. Rev. B* **86** (2012).

[116] Fujiwara, K., Kanamoto, K., Ohta, Y., Tokuda, Y. & Nakayama, T. Classification and origins of GaAs oval defects grown by molecular beam epitaxy. *Journal of Crystal Growth* **80**, 104–112 (1987). URL http://www.sciencedirect.com/science/article/pii/002202488790529X.

[117] Chand, N. & Chu, S. A comprehensive study and methods of elimination of oval defects in MBE-GaAs. *Journal of Crystal Growth* **104**, 485–497 (1990). URL http://www.sciencedirect.com/science/article/pii/002202489090151A.

[118] Berry, M. V. *Rays, wavefronts and phase: a picture book of cusps* (Elsevier Science Publishers B.V., Amsterdam, 1992), 1992 edn. URL http://www.phy.bris.ac.uk/people/berry_mv/the_papers/Berry228.pdf.

[119] Berry, M. V., Nye, J. F. & Wright, F. J. The elliptic umbilic diffraction catastrophe. *Philosophical Transactions of the Royal Society of London. Series A, Mathematical and Physical Sciences* **291**, 453–484 (1979). URL http://www.jstor.org/stable/75150. ArticleType: research-article / Full publication date: Apr. 12, 1979 / Copyright © 1979 The Royal Society.

[120] P. Senthilkumaran, S. V. Two dimensional vortex lattices from pure wavefront tilts. *Opt Commun* **283**, 2767–2771 (2010). URL http://202.114.89.42/resource/pdf/5496.pdf.

[121] Ruben, G. & Paganin, D. M. Phase vortices from a young's three-pinhole interferometer. *Phys. Rev. E* **75**, 066613 (2007). URL http://link.aps.org/doi/10.1103/PhysRevE.75.066613.

[122] Flayac, H., Solnyshkov, D. & Malpuech, G. Oblique half-solitons and their generation in exciton-polariton condensates. *Phys. Rev. B* (2011). URL http://arxiv.org/abs/1103.4516. H. Flayac, D. D. Solnyshkov, and G. Malpuech, Phys. Rev. B 83, 193305 (2011).

[123] Panzarini, G. *et al.* Exciton-light coupling in single and coupled semiconductor microcavities: Polariton dispersion and polarization splitting. *Phys. Rev. B* **59**, 5082–5089 (1999). URL http://link.aps.org/doi/10.1103/PhysRevB.59.5082.

[124] Kavokin, A., Malpuech, G. & Glazov, M. Optical spin hall effect. *Phys. Rev. Lett.* **95**, 136601 (2005). URL http://link.aps.org/doi/10.1103/PhysRevLett.95.136601.

[125] Leyder, C. *et al.* Observation of the optical spin hall effect. *Nature Physics* **3**, 628–631 (2007). URL http://www.nature.com/nphys/journal/v3/n9/full/nphys676.html.

[126] Maragkou, M. *et al.* Optical analogue of the spin hall effect in a photonic cavity. *Opt. Lett.* **36**, 1095–1097 (2011). URL http://ol.osa.org/abstract.cfm?URI=ol-36-7-1095.

[127] Cilibrizzi, P. *et al.* Linear Wave Dynamics Explains Observations Attributed to Dark Solitons in a Polariton Quantum Fluid. *Physical Review Letters* **113**, 103901 (2014). URL http://link.aps.org/doi/10.1103/PhysRevLett.113.103901.

[128] Kamchatnov, A. M. & Pavloff, N. Interference effects in the two-dimensional scattering of microcavity polaritons by an obstacle: phase dislocations and resonances. *The European Physical Journal D* **69**, 1–11 (2015). URL http://link.springer.com/article/10.1140/epjd/e2014-50750-9.

[129] Amo, A. *et al.* Comment on "Linear Wave Dynamics Explains Observations Attributed to Dark Solitons in a Polariton Quantum Fluid". *Physical Review Letters* **115**, 089401 (2015). URL http://link.aps.org/doi/10.1103/PhysRevLett.115.089401.

[130] Cilibrizzi, P. *et al.* Cilibrizzi \textit{et al.} Reply:. *Physical Review Letters* **115**, 089402 (2015). URL http://link.aps.org/doi/10.1103/PhysRevLett.115.089402.

[131] Amo, A. *et al.* Light engineering of the polariton landscape in semiconductor microcavities. *Physical Review B* **82**, 081301 (2010). URL http://link.aps.org/doi/10.1103/PhysRevB.82.081301.

[132] Wertz, E. *et al.* Spontaneous formation and optical manipulation of extended polariton condensates. *Nature Physics* **6**, 860–864 (2010). URL http://www.nature.com/nphys/journal/v6/n11/full/nphys1750.html.

[133] Tosi, G. *et al.* Sculpting oscillators with light within a nonlinear quantum fluid. *Nature Physics* **8**, 190–194 (2012). URL http://www.nature.com/nphys/journal/v8/n3/full/nphys2182.html.

[134] Manek, I., Ovchinnikov, Y. & Grimm, R. Generation of a hollow laser beam for atom trapping using an axicon. *Optics Communications* **147**, 67–70 (1998). URL http://www.sciencedirect.com/science/article/pii/S0030401897006457.

[135] Wehner, M. U., Ulm, M. H. & Wegener, M. Scanning interferometer stabilized by use of Pancharatnam's phase. *Optics Letters* **22**, 1455–1457 (1997). URL http://ol.osa.org/abstract.cfm?URI=ol-22-19-1455.

[136] Lagoudakis, K. *The Physics of Exciton-Polariton Condensates* (EPFL Press, 2013). URL http://www.crcpress.com/product/isbn/9781482212143.

[137] Tsotsis, P. *et al.* Lasing threshold doubling at the crossover from strong to weak coupling regime in GaAs microcavity. *New Journal of Physics* **14**, 023060 (2012). URL http://iopscience.iop.org/1367-2630/14/2/023060.

[138] Daskalakis, K. S., Maier, S. A., Murray, R. & Kéna-Cohen, S. Nonlinear interactions in an organic polariton condensate. *Nature Materials* **13**, 271–278 (2014). URL http://www.nature.com/nmat/journal/v13/n3/full/nmat3874.html.

[139] Wertz, E. *et al.* Spontaneous formation of a polariton condensate in a planar GaAs microcavity. *Applied Physics Letters* **95**, 051108 (2009). URL http://scitation.aip.org/content/aip/journal/apl/95/5/10.1063/1.3192408.

[140] Zajac, J. M., Langbein, W., Hugues, M. & Hopkinson, M. Polariton states bound to defects in GaAs/AlAs planar microcavities. *Physical Review B* **85**,

165309 (2012). URL http://link.aps.org/doi/10.1103/PhysRevB.85.165309.

[141] Gurioli, M. *et al.* Experimental study of disorder in a semiconductor microcavity. *Physical Review B* **64**, 165309 (2001). URL http://link.aps.org/doi/10.1103/PhysRevB.64.165309.

[142] Langbein, W. & Hvam, J. M. Elastic Scattering Dynamics of Cavity Polaritons: Evidence for Time-Energy Uncertainty and Polariton Localization. *Physical Review Letters* **88**, 047401 (2002). URL http://link.aps.org/doi/10.1103/PhysRevLett.88.047401.

[143] Langbein, W. Energy and momentum broadening of planar microcavity polaritons measured by resonant light scattering. *Journal of Physics: Condensed Matter* **16**, S3645 (2004). URL http://iopscience.iop.org/0953-8984/16/35/006.

[144] Abbarchi, M. *et al.* Discretized disorder in planar semiconductor microcavities: Mosaicity effect on resonant Rayleigh scattering and optical parametric oscillation. *Physical Review B* **85**, 045316 (2012). URL http://link.aps.org/doi/10.1103/PhysRevB.85.045316.

[145] Zajac, J. M., Clarke, E. & Langbein, W. Suppression of cross-hatched polariton disorder in GaAs/AlAs microcavities by strain compensation. *Applied Physics Letters* **101**, 041114 (2012). URL http://scitation.aip.org/content/aip/journal/apl/101/4/10.1063/1.4739245.

[146] Houdré, R. *et al.* Saturation of the strong-coupling regime in a semiconductor microcavity: Free-carrier bleaching of cavity polaritons. *Physical Review B* **52**, 7810–7813 (1995). URL http://link.aps.org/doi/10.1103/PhysRevB.52.7810.

[147] Sanvitto, D. *et al.* All-optical control of the quantum flow of a polariton condensate. *Nature Photonics* **5**, 610–614 (2011). URL http://www.nature.com/nphoton/journal/v5/n10/full/nphoton.2011.211.html.

[148] Kammann, E., Ohadi, H., Maragkou, M., Kavokin, A. V. & Lagoudakis, P. G. Crossover from photon to exciton-polariton lasing. *New Journal of Physics* **14**, 105003 (2012). URL http://iopscience.iop.org/1367-2630/14/10/105003.

[149] Cilibrizzi, P. *et al.* Polariton condensation in a strain-compensated planar microcavity with InGaAs quantum wells. *Applied Physics Letters* **105**, 191118 (2014). URL http://scitation.aip.org/content/aip/journal/apl/105/19/10.1063/1.4901814.

[150] Balili, R. B., Snoke, D. W., Pfeiffer, L. & West, K. Actively tuned and spatially trapped polaritons. *Applied Physics Letters* **88**, 031110–031110–3 (2006). URL http://apl.aip.org/resource/1/applab/v88/i3/p031110_s1.

[151] Maragkou, M. *et al.* Spontaneous nonground state polariton condensation in pillar microcavities. *Physical Review B* **81**, 081307 (2010). URL http://link.aps.org/doi/10.1103/PhysRevB.81.081307.

[152] Bajoni, D. *et al.* Polariton laser using single micropillar GaAs-GaAlAs semiconductor cavities. *Physical Review Letters* **100**, 047401 (2008). URL http://link.aps.org/doi/10.1103/PhysRevLett.100.047401.

[153] Ferrier, L. *et al.* Interactions in confined polariton condensates. *Physical Review Letters* **106**, 126401 (2011). URL http://link.aps.org/doi/10.1103/PhysRevLett.106.126401.

[154] Das, A., Bhattacharya, P., Heo, J., Banerjee, A. & Guo, W. Polariton Bose–Einstein condensate at room temperature in an al(Ga)N nanowire–dielectric microcavity with a spatial potential trap. *Proceedings of the National Academy of Sciences* **110**, 2735–2740 (2013). URL http://www.pnas.org/content/110/8/2735. PMID: 23382183.

[155] Spano, R. *et al.* Coherence properties of exciton polariton OPO condensates in one and two dimensions. *New Journal of Physics* **14**, 075018 (2012). URL http://iopscience.iop.org/1367-2630/14/7/075018.

[156] Antón, C. *et al.* Energy relaxation of exciton-polariton condensates in quasi-one-dimensional microcavities. *Physical Review B* **88**, 035313 (2013). URL http://link.aps.org/doi/10.1103/PhysRevB.88.035313.

[157] Sanvitto, D. *et al.* Exciton-polariton condensation in a natural two-dimensional trap. *Physical Review B* **80**, 045301 (2009). URL http://link.aps.org/doi/10.1103/PhysRevB.80.045301.

[158] Gao, T. *et al.* Polariton condensate transistor switch. *Physical Review B* **85**, 235102 (2012). URL http://link.aps.org/doi/10.1103/PhysRevB.85.235102.

[159] Antón, C. *et al.* Dynamics of a polariton condensate transistor switch. *Applied Physics Letters* **101**, 261116 (2012). URL http://scitation.aip.org/content/aip/journal/apl/101/26/10.1063/1.4773376.

[160] Antón, C. *et al.* Quantum reflections and shunting of polariton condensate wave trains: Implementation of a logic AND gate. *Physical Review B* **88**, 245307 (2013). URL http://link.aps.org/doi/10.1103/PhysRevB.88.245307.

[161] Heller, W., Filoramo, A., Roussignol, P. & Bockelmann, U. Direct measurement of exciton diffusion in quantum wells. *Solid-State Electronics* **40**, 725–728 (1996). URL http://www.sciencedirect.com/science/article/pii/0038110195003517.

[162] Nagamune, Y., Watabe, H., Sogawa, F. & Arakawa, Y. One-dimensional exciton diffusion in GaAs quantum wires. *Applied Physics Letters* **67**, 1535–1537 (1995). URL http://apl.aip.org/resource/1/applab/v67/i11/p1535_s1.

[163] Roumpos, G., Nitsche, W. H., Höfling, S., Forchel, A. & Yamamoto, Y. Gain-induced trapping of microcavity exciton polariton condensates. *Physical Review Letters* **104**, 126403 (2010). URL http://link.aps.org/doi/10.1103/PhysRevLett.104.126403.

[164] Kreis, T. *Holographic interferometry: principles and methods* (Akademie Verlag, 1996).

[165] Gulia, M., Rossi, F., Molinari, E., Selbmann, P. E. & Lugli, P. Phonon-assisted exciton formation and relaxation in GaAs/Al_{x}Ga_{1-x}As quantum wells. *Physical Review B* **55**, R16049–R16052 (1997). URL http://link.aps.org/doi/10.1103/PhysRevB.55.R16049.

[166] Adrados, C. *et al.* Motion of Spin Polariton Bullets in Semiconductor Microcavities. *Physical Review Letters* **107**, 146402 (2011). URL http://link.aps.org/doi/10.1103/PhysRevLett.107.146402.

[167] Cristofolini, P. *et al.* Optical superfluid phase transitions and trapping of polariton condensates. *Physical Review Letters* **110**, 186403 (2013). URL http://link.aps.org/doi/10.1103/PhysRevLett.110.186403.

[168] Kasprzak, J., Solnyshkov, D. D., André, R., Dang, L. S. & Malpuech, G. Formation of an Exciton Polariton Condensate: Thermodynamic versus Kinetic Regimes. *Physical Review Letters* **101**, 146404 (2008). URL http://link.aps.org/doi/10.1103/PhysRevLett.101.146404.

[169] Vishnevsky, D. V., Solnyshkov, D. D., Gippius, N. A. & Malpuech, G. Multistability of cavity exciton polaritons affected by the thermally generated exciton reservoir. *Physical Review B* **85**, 155328 (2012). URL http://link.aps.org/doi/10.1103/PhysRevB.85.155328.

[170] Love, A. P. D. *et al.* Intrinsic decoherence mechanisms in the microcavity polariton condensate. *Physical Review Letters* **101**, 067404 (2008). URL http://link.aps.org/doi/10.1103/PhysRevLett.101.067404.

[171] Tassone, F. & Yamamoto, Y. Lasing and squeezing of composite bosons in a semiconductor microcavity. *Physical Review A* **62**, 063809 (2000). URL http://link.aps.org/doi/10.1103/PhysRevA.62.063809.

[172] Porras, D. & Tejedor, C. Linewidth of a polariton laser. *Physical Review B* **67**, 161310 (2003). URL http://link.aps.org/doi/10.1103/PhysRevB.67.161310.

[173] Sun, Y. *et al.* Polaritons are Not Weakly Interacting: Direct Measurement of the Polariton-Polariton Interaction Strength. *arXiv:1508.06698 [cond-mat]* (2015). URL http://arxiv.org/abs/1508.06698. ArXiv: 1508.06698.

[174] Maragkou, M. *et al.* Spontaneous nonground state polariton condensation in pillar microcavities. *Physical Review B* **81**, 081307 (2010). URL http://link.aps.org/doi/10.1103/PhysRevB.81.081307.

[175] Nardin, G., Léger, Y., Pietka, B., Morier-Genoud, F. & Deveaud-Plédran, B. Phase-resolved imaging of confined exciton-polariton wave functions in elliptical traps. *Physical Review B* **82**, 045304 (2010). URL http://link.aps.org/doi/10.1103/PhysRevB.82.045304.

[176] Eastham, P. R. Mode locking and mode competition in a nonequilibrium solid-state condensate. *Physical Review B* **78**, 035319 (2008). URL http://link.aps.org/doi/10.1103/PhysRevB.78.035319.

[177] Portolan, S., Hauke, P. & Savona, V. Parametric photoluminescence of spatially confined polaritons in patterned microcavities. *physica status solidi (b)* **245**, 1089–1092 (2008). URL http://onlinelibrary.wiley.com/doi/10.1002/pssb.200777626/abstract.

[178] Manni, F., Lagoudakis, K. G., Liew, T. C. H., André, R. & Deveaud-Plédran, B. Spontaneous pattern formation in a polariton condensate. *Physical Review Letters* **107**, 106401 (2011). URL http://link.aps.org/doi/10.1103/PhysRevLett.107.106401.

[179] Askitopoulos, A. *et al.* Polariton condensation in an optically induced two-dimensional potential. *Physical Review B* **88**, 041308 (2013). URL http://link.aps.org/doi/10.1103/PhysRevB.88.041308.

[180] Wouters, M. & Carusotto, I. Excitations in a nonequilibrium bose-einstein condensate of exciton polaritons. *Physical Review Letters* **99**, 140402 (2007). URL http://link.aps.org/doi/10.1103/PhysRevLett.99.140402.

[181] Wouters, M. Energy relaxation in the mean-field description of polariton condensates. *New Journal of Physics* **14**, 075020 (2012). URL http://iopscience.iop.org/1367-2630/14/7/075020.

[182] Wouters, M., Liew, T. C. H. & Savona, V. Energy relaxation in one-dimensional polariton condensates. *Physical Review B* **82**, 245315 (2010). URL http://link.aps.org/doi/10.1103/PhysRevB.82.245315.

[183] Solnyshkov, D. D., Terças, H., Dini, K. & Malpuech, G. Hybrid Boltzmann–Gross-Pitaevskii theory of bose-einstein condensation and superfluidity in open driven-dissipative systems. *Physical Review A* **89**, 033626 (2014). URL http://link.aps.org/doi/10.1103/PhysRevA.89.033626.

[184] Sieberer, L. M., Huber, S. D., Altman, E. & Diehl, S. Nonequilibrium functional renormalization for driven-dissipative bose-einstein condensation. *Physical Review B* **89**, 134310 (2014). URL http://link.aps.org/doi/10.1103/PhysRevB.89.134310.

[185] Haug, H., Doan, T. D. & Tran Thoai, D. B. Quantum kinetic derivation of the nonequilibrium Gross-Pitaevskii equation for nonresonant excitation of microcavity polaritons. *Physical Review B* **89**, 155302 (2014). URL http://link.aps.org/doi/10.1103/PhysRevB.89.155302.

[186] Nelsen, B. *et al.* Dissipationless Flow and Sharp Threshold of a Polariton Condensate with Long Lifetime. *Physical Review X* **3**, 041015 (2013). URL http://link.aps.org/doi/10.1103/PhysRevX.3.041015.

[187] Steger, M., Gautham, C., Snoke, D. W., Pfeiffer, L. & West, K. Slow reflection and two-photon generation of microcavity exciton–polaritons. *Optica* **2**, 1 (2015). URL https://www.osapublishing.org/optica/abstract.cfm?uri=optica-2-1-1.

[188] Dreismann, A. *et al.* Coupled counterrotating polariton condensates in optically defined annular potentials. *Proceedings of the National Academy of Sciences* 201401988 (2014). URL http://www.pnas.org/content/early/2014/05/30/1401988111.

[189] Gavrilov, S. S. *et al.* Polariton multistability and fast linear-to-circular polarization conversion in planar microcavities with lowered symmetry. *Applied Physics Letters* **102**, 011104–011104–4 (2013). URL http://apl.aip.org/resource/1/applab/v102/i1/p011104_s1.

[190] Martin, M. D., Viña, L., Son, J. K. & Mendez, E. E. Spin dynamics of cavity polaritons. *Solid State Communications* **117**, 267–271 (2001). URL http://www.sciencedirect.com/science/article/pii/S0038109800004269.

[191] Martin, M. D., Viña, L. & Mendez, E. E. Ultrafast light-polarization dynamics in semiconductor microcavities. *Solid State Communications* **119**, 259–270 (2001). URL http://www.sciencedirect.com/science/article/pii/S0038109801001156.

[192] Martín, M., Aichmayr, G., Viña, L. & André, R. Polarization Control of the Nonlinear Emission of Semiconductor Microcavities. *Physical Review Letters* **89**, 077402 (2002). URL http://link.aps.org/doi/10.1103/PhysRevLett.89.077402.

[193] Lagoudakis, P. G. *et al.* Stimulated spin dynamics of polaritons in semiconductor microcavities. *Physical Review B* **65**, 161310 (2002). URL http://link.aps.org/doi/10.1103/PhysRevB.65.161310.

[194] Kavokin, A., Lagoudakis, P. G., Malpuech, G. & Baumberg, J. J. Polarization rotation in parametric scattering of polaritons in semiconductor microcavities. *Physical Review B* **67**, 195321 (2003). URL http://link.aps.org/doi/10.1103/PhysRevB.67.195321.

[195] Ballarini, D. *et al.* All-optical polariton transistor. *Nature Communications* **4**, 1778 (2013). URL http://www.nature.com/ncomms/journal/v4/n4/abs/ncomms2734.html.

[196] Antón, C. *et al.* Operation speed of polariton condensate switches gated by excitons. *Physical Review B* **89**, 235312 (2014). URL http://link.aps.org/doi/10.1103/PhysRevB.89.235312.

[197] Amo, A. *et al.* Exciton–polariton spin switches. *Nature Photonics* **4**, 361–366 (2010). URL http://www.nature.com/nphoton/journal/v4/n6/abs/nphoton.2010.79.html.

[198] Kammann, E. *et al.* Nonlinear Optical Spin Hall Effect and Long-Range Spin Transport in Polariton Lasers. *Physical Review Letters* **109**, 036404 (2012). URL http://link.aps.org/doi/10.1103/PhysRevLett.109.036404.

[199] Antón, C. *et al.* Optical control of spin textures in quasi-one-dimensional polariton condensates. *Physical Review B* **91**, 075305 (2015). URL http://link.aps.org/doi/10.1103/PhysRevB.91.075305.

[200] Liew, T. C. H., Kavokin, A. V. & Shelykh, I. A. Optical Circuits Based on Polariton Neurons in Semiconductor Microcavities. *Physical Review Letters* **101**, 016402 (2008). URL http://link.aps.org/doi/10.1103/PhysRevLett.101.016402.

[201] Espinosa-Ortega, T. & Liew, T. C. H. Complete architecture of integrated photonic circuits based on and and not logic gates of exciton polaritons in

semiconductor microcavities. *Physical Review B* **87**, 195305 (2013). URL http://link.aps.org/doi/10.1103/PhysRevB.87.195305.

[202] Cuadra, J. *et al.* Polarized emission in polariton condensates: Switching in a one-dimensional natural trap versus inversion in two dimensions. *Physical Review B* **88**, 235312 (2013). URL http://link.aps.org/doi/10.1103/PhysRevB.88.235312.

[203] Martin, M. D. *et al.* Striking dynamics of II–VI microcavity polaritons after linearly polarized excitation. *physica status solidi (c)* **2**, 3880–3883 (2005). URL http://onlinelibrary.wiley.com/doi/10.1002/pssc.200562036/abstract.

[204] Laussy, F. P., Shelykh, I. A., Malpuech, G. & Kavokin, A. Effects of Bose-Einstein condensation of exciton polaritons in microcavities on the polarization of emitted light. *Physical Review B* **73**, 035315 (2006). URL http://link.aps.org/doi/10.1103/PhysRevB.73.035315.

[205] del Valle, E. *et al.* Dynamics of the Formation and Decay of Coherence in a Polariton Condensate. *Physical Review Letters* **103**, 096404 (2009). URL http://link.aps.org/doi/10.1103/PhysRevLett.103.096404.

[206] Richards, B. & Wolf, E. Electromagnetic Diffraction in Optical Systems. II. Structure of the Image Field in an Aplanatic System. *Proceedings of the Royal Society of London A: Mathematical, Physical and Engineering Sciences* **253**, 358–379 (1959). URL http://rspa.royalsocietypublishing.org/content/253/1274/358.

[207] Ha, T., Laurence, T. A., Chemla, D. S. & Weiss, S. Polarization Spectroscopy of Single Fluorescent Molecules. *The Journal of Physical Chemistry B* **103**, 6839–6850 (1999). URL http://dx.doi.org/10.1021/jp990948j.

[208] Lindfors, K., Friberg, A. T., Setälä, T. & Kaivola, M. Degree of polarization in tightly focused optical fields. *Journal of the Optical Society of America A* **22**, 561–568 (2005). URL http://josaa.osa.org/abstract.cfm?URI=josaa-22-3-561.

[209] Glazov, M. M., Semina, M. A., Sherman, E. Y. & Kavokin, A. V. Spin noise of exciton polaritons in microcavities. *Physical Review B* **88**, 041309 (2013). URL http://link.aps.org/doi/10.1103/PhysRevB.88.041309.

[210] Fainstein, A. *et al.* In-plane birefringence of GaAs/AlAs multiple quantum wells. *Physical Review B* **50**, 11850–11860 (1994). URL http://link.aps.org/doi/10.1103/PhysRevB.50.11850.

[211] Sirenko, A. A., Etchegoin, P., Fainstein, A., Eberl, K. & Cardona, M. Linear Birefringence in GaAs/AlAs Multiple Quantum Wells. *physica status solidi (b)* **215**, 241–246 (1999). URL http://onlinelibrary.wiley.com/doi/10.1002/(SICI)1521-3951(199909)215:1<241::AID-PSSB241>3.0.CO;2-3/abstract.

[212] Ohke, S., Umeda, T. & Cho, Y. TM-mode propagation and form birefringence in a GaAs-AlGaAs multiple quantum well optical waveguide. *Optics Communications* **70**, 92–96 (1989). URL http://www.sciencedirect.com/science/article/pii/0030401889902757.

[213] Levrat, J. *et al.* Pinning and Depinning of the Polarization of Exciton-Polariton Condensates at Room Temperature. *Physical Review Letters* **104**, 166402 (2010). URL http://link.aps.org/doi/10.1103/PhysRevLett.104.166402.

[214] Wouters, M., Carusotto, I. & Ciuti, C. Spatial and spectral shape of inhomogeneous nonequilibrium exciton-polariton condensates. *Physical Review B* **77**, 115340 (2008). URL http://link.aps.org/doi/10.1103/PhysRevB.77.115340.

[215] Porras, D., Ciuti, C., Baumberg, J. J. & Tejedor, C. Polariton dynamics and Bose-Einstein condensation in semiconductor microcavities. *Physical Review B* **66**, 085304 (2002). URL http://link.aps.org/doi/10.1103/PhysRevB.66.085304.

[216] Shelykh, I. A., Johne, R., Solnyshkov, D. D. & Malpuech, G. Optically and electrically controlled polariton spin transistor. *Physical Review B* **82**, 153303 (2010). URL http://link.aps.org/doi/10.1103/PhysRevB.82.153303.

[217] Bogoliubov, N. N. On the theory of superfluidity. *J. Phys USSR* **11**, 23–32 (1947).

[218] Andrews, M. R. *et al.* Propagation of sound in a Bose-Einstein condensate. *Physical Review Letters* **79**, 553–556 (1997). URL http://link.aps.org/doi/10.1103/PhysRevLett.79.553.

[219] Stamper-Kurn, D. M. *et al.* Excitation of Phonons in a Bose-Einstein Condensate by Light Scattering. *Physical Review Letters* **83**, 2876–2879 (1999). URL http://link.aps.org/doi/10.1103/PhysRevLett.83.2876.

[220] Snelling, M. J., Blackwood, E., McDonagh, C. J., Harley, R. T. & Foxon, C. T. B. Exciton, heavy-hole, and electron g factors in type-i GaAs/Al_xGa_1-xAs quantum wells. *Physical Review B* **45**, 3922–3925 (1992). URL http://link.aps.org/doi/10.1103/PhysRevB.45.3922.

[221] Berger, J. D. *et al.* Magnetic-field enhancement of the exciton-polariton splitting in a semiconductor quantum-well microcavity: The strong coupling threshold. *Physical Review B* **54**, 1975–1981 (1996). URL http://link.aps.org/doi/10.1103/PhysRevB.54.1975.

[222] Piętka, B. *et al.* Magnetic field tuning of exciton-polaritons in a semiconductor microcavity. *Physical Review B* **91**, 075309 (2015). URL http://link.aps.org/doi/10.1103/PhysRevB.91.075309.

[223] Rubo, Y. G., Kavokin, A. & Shelykh, I. Suppression of superfluidity of exciton-polaritons by magnetic field. *Physics Letters A* **358**, 227–230 (2006). URL http://www.sciencedirect.com/science/article/pii/S0375960106007158.

[224] Larionov, A. V. *et al.* Polarized Nonequilibrium Bose-Einstein Condensates of Spinor Exciton Polaritons in a Magnetic Field. *Physical Review Letters* **105**, 256401 (2010). URL http://link.aps.org/doi/10.1103/PhysRevLett.105.256401.

[225] Walker, P. *et al.* Suppression of Zeeman Splitting of the Energy Levels of Exciton-Polariton Condensates in Semiconductor Microcavities in an External Magnetic Field. *Physical Review Letters* **106**, 257401 (2011). URL http://link.aps.org/doi/10.1103/PhysRevLett.106.257401.

[226] Rahimi-Iman, A. *et al.* Zeeman splitting and diamagnetic shift of spatially confined quantum-well exciton polaritons in an external magnetic field. *Physical Review B* **84**, 165325 (2011). URL http://link.aps.org/doi/10.1103/PhysRevB.84.165325.

[227] Fischer, J. *et al.* Anomalies of a Nonequilibrium Spinor Polariton Condensate in a Magnetic Field. *Physical Review Letters* **112**, 093902 (2014). URL http://link.aps.org/doi/10.1103/PhysRevLett.112.093902.

[228] Fischer, J. *et al.* Spatial Coherence Properties of One Dimensional Exciton-Polariton Condensates. *Physical Review Letters* **113**, 203902 (2014). URL http://link.aps.org/doi/10.1103/PhysRevLett.113.203902.

[229] Ogawa, T. Exciton Mott transition and quantum condensation in electron-hole systems. *physica status solidi (c)* **6**, 28–33 (2009). URL http://onlinelibrary.wiley.com/doi/10.1002/pssc.200779880/abstract.

[230] Gorkov, L. P. & Dzyaloshinskii, I. E. Contribution to the theory of the mott exciton in a strong magnetic field. *physica status solidi (c)* **26**, 449 (1967). URL http://www.jetp.ac.ru/cgi-bin/e/index/e/26/2/p449?a=list.

[231] Kavokin, A. Polaritons: The rise of the bosonic laser. *Nature Photonics* **7**, 591–592 (2013). URL http://www.nature.com/nphoton/journal/v7/n8/full/nphoton.2013.196.html.

[232] Andreani, L. C., Benedek, G. & Molinari, E. *Radiation-matter Interaction in Confined Systems. Dedicated to the Memory of Giovanna Panzarini* (SIF Edizioni Scientifiche, 2002).

[233] Ivchenko, E. L. *Optical Spectroscopy of Semiconductor Nanostructures* (Alpha Science, 2005).

[234] Kumar, R., Vengurlekar, A. S., Prabhu, S. S., Shah, J. & Pfeiffer, L. N. Picosecond time evolution of free electron-hole pairs into excitons in GaAs quantum wells. *Physical Review B* **54**, 4891–4897 (1996). URL http://link.aps.org/doi/10.1103/PhysRevB.54.4891.

[235] Kochereshko, V. P. *et al.* Phase diagrams of magnetopolariton gases. *arXiv:1309.6983 [cond-mat]* (2013). URL http://arxiv.org/abs/1309.6983.

[236] Lai, Y.-Y., Lan, Y.-P. & Lu, T.-C. High-Temperature Polariton Lasing in a Strongly Coupled ZnO Microcavity. *Applied Physics Express* **5**, 082801 (2012). URL http://iopscience.iop.org/1882-0786/5/8/082801.

[237] Christmann, G. *et al.* Polariton ring condensates and sunflower ripples in an expanding quantum liquid. *Physical Review B* **85**, 235303 (2012). URL http://link.aps.org/doi/10.1103/PhysRevB.85.235303.

[238] Ohadi, H. *et al.* Dissipative phase locking of exciton-polariton condensates. *arXiv:1406.6377 [cond-mat]* (2014). URL http://arxiv.org/abs/1406.6377. arXiv: 1406.6377.

[239] Georgescu, I., Ashhab, S. & Nori, F. Quantum simulation. *Reviews of Modern Physics* **86**, 153–185 (2014). URL http://link.aps.org/doi/10.1103/RevModPhys.86.153.

Appendices

Trapped modes calculation

1. The pump profile was taken as:

$$f_r(\mathbf{r}) = \frac{L_0^4}{\left(\left(x^2 + \beta y^2 - r_0^2\right)^2 + L_0^4\right)} \tag{9.11}$$

where L_0 determines the thickness of the ring, β is related to the ellipticity, and r_0 is the radius. Note that this profile has a non-zero intensity in the center.

2. In addition to the parameters already written in the text, we have $\beta = 1.2$. The other parameters were tuned to give the various mode profiles and we have taken:

Figure	L_0 (μm)	x_0 (μm)	N_r (μm^{-2})
1f)	8.5	7.5	192
1g)	7.5	8.5	192
1h)	7.5	7.5	183
1i)	9	9	167
1j)	9	8	183

TABLE 9.1: Additional parameters for theoretical simulations.

3. To define the chemical potential, we follow a similar technique to Ref.[M Wouters, New J. Phys., **14**, 075020 (2012)]. The energy relaxation term has the form:

$$\mathfrak{R}\left[\psi(\mathbf{r},t)\right] = -\lambda N_r f_r(\mathbf{r}) \left(\hat{E}_{\mathrm{LP}} - \mu(\mathbf{r},t)\right) \psi(\mathbf{r},t) \tag{9.12}$$

$$= \left.\frac{d\psi(\mathbf{r},t)}{dt}\right|_{\mathfrak{R}} \tag{9.13}$$

where the notation used in the last line indicates that this is the contribution to $d\psi(\mathbf{r},t)/dt$ due to energy relaxation. The local effective chemical potential $\mu(\mathbf{r},t)$ is defined to enforce the condition that energy relaxation does not change the total polariton density, $n(\mathbf{r},t)$:

$$\left.\frac{d\sqrt{n(\mathbf{r},t)}}{dt}\right|_{\mathfrak{R}} = 0 \tag{9.14}$$

Note, however, that other terms in $d\psi(\mathbf{r},t)/dt$ may change the polariton density (e.g., pumping and decay terms). The polariton density is related to the wavefunction by $\psi(\mathbf{r},t) = \sqrt{n(\mathbf{r},t)}e^{i\theta(\mathbf{r},t)}$, where $\theta(\mathbf{r},t)$ is the local condensate phase. Note that:

$$\begin{aligned}\left.\frac{d\psi(\mathbf{r},t)}{dt}\right|_{\mathfrak{R}} = &\left.\frac{d\sqrt{n(\mathbf{r},t)}}{dt}\right|_{\mathfrak{R}} e^{i\theta(\mathbf{r},t)} \\ &+ i\sqrt{n(\mathbf{r},t)}e^{i\theta(\mathbf{r},t)}\left.\frac{d\theta(\mathbf{r},t)}{dt}\right|_{\mathfrak{R}}\end{aligned} \tag{9.15}$$

Multiplying by $e^{-i\theta(\mathbf{r},t)}$ and taking the real parts, we find that:

$$\begin{aligned}&\mathrm{Re}\left\{\left.\frac{d\psi(\mathbf{r},t)}{dt}\right|_{\mathfrak{R}} e^{-i\theta(\mathbf{r},t)}\right\} && (9.16)\\ &= \mathrm{Re}\left\{\mathfrak{R}\left[\psi(\mathbf{r},t)\right]e^{-i\theta(\mathbf{r},t)}\right\} && (9.17)\\ &= \mathrm{Re}\left\{-\lambda N_r f_r(\mathbf{r})\hat{E}_{\mathrm{LP}}\psi(\mathbf{r},t)e^{-i\theta(\mathbf{r},t)}\right\} && (9.18)\\ &\quad + \mathrm{Re}\left\{\lambda N_r f_r(\mathbf{r})\mu(\mathbf{r},t)\psi(\mathbf{r},t)e^{-i\theta(\mathbf{r},t)}\right\} && (9.19)\\ &= \left.\frac{d\sqrt{n(\mathbf{r},t)}}{dt}\right|_{\mathfrak{R}} && (9.20)\end{aligned}$$

According to condition 9.14, this term must vanish. This is precisely the condition enforced by the chemical potential $\mu(\mathbf{r},t)$. This leaves only the imaginary part non-zero:

$$\begin{aligned}&\mathfrak{R}\left[\psi(\mathbf{r},t)\right]e^{-i\theta(\mathbf{r},t)} \\ &\qquad = i\mathrm{Im}\left\{\mathfrak{R}\left[\psi(\mathbf{r},t)\right]e^{-i\theta(\mathbf{r},t)}\right\} && (9.21)\\ &\qquad = i\mathrm{Im}\left\{-\lambda N_r f_r(\mathbf{r})\hat{E}_{\mathrm{LP}}\psi(\mathbf{r},t)e^{-i\theta(\mathbf{r},t)}\right\} && (9.22)\end{aligned}$$

or

$$\mathfrak{R}\left[\psi(\mathbf{r},t)\right] = ie^{-i\theta(\mathbf{r},t)}\mathrm{Im}\left\{-\lambda N_r f_r(\mathbf{r})\hat{E}_{\mathrm{LP}}\psi(\mathbf{r},t)e^{-i\theta(\mathbf{r},t)}\right\} \tag{9.23}$$

This shows that in practice we do not need the explicit form of $\mu(\mathbf{r},t)$ as the above expression can be used in the evolution equation for the polariton wavefunction.

List of publications

Publications

Journal Articles

- A. Askitopoulos, L. Mouchliadis, I. Iorsh, G. Christmann, J. J. Baumberg, M. A. Kaliteevski, Z. Hatzopoulos, and P. G. Savvidis, *Bragg Polaritons: Strong Coupling and Amplification in an Unfolded Microcavity*, Phys. Rev. Lett., vol. 106, no. 7, p. 076401, Feb. 2011

- G. Christmann, A. Askitopoulos, G. Deligeorgis, Z. Hatzopoulos, S. I. Tsintzos, P. G. Savvidis, and J. J. Baumberg, *Oriented polaritons in strongly-coupled asymmetric double quantum well microcavities*, Applied Physics Letters, vol. 98, no. 8, p. 081111, Feb. 2011

- A. Askitopoulos, H. Ohadi, A. V. Kavokin, Z. Hatzopoulos, P. G. Savvidis, and P. G. Lagoudakis, *Polariton condensation in an optically induced two-dimensional potential*, Phys. Rev. B, vol. 88, no. 4, p. 041308, Jul. 2013

- P. Cilibrizzi, H. Ohadi, T. Ostatnicky, A. Askitopoulos, W. Langbein, and P. Lagoudakis, *Linear wave dynamics explains observations attributed to dark-solitons in a polariton quantum fluid*, Phys. Rev. Lett., vol. 113, no. 10, p. 103901

- P. Cillibrizzi, A. Askitopoulos, M. Silva, F. Bastiman, E. Clarke, J. M. Zajac, W. Langbein, P.G. Lagoudakis *Polariton condensation in a strain-compensated planar microcavity with InGaAs quantum wells* Applied Physics Letters, vol. 105, no. 19, p. 191118 (2014)

- A. Askitopoulos, T.C.H. Liew, H. Ohadi, Z. Hatzopoulos, P.G. Savvidis and P.G. Lagoudakis, *Robust platform for engineering pure-quantum-state transitions in polariton condensates* Phys. Rev. B., vol. 92, no. 3, p. 035305, Jul. 2015

- V. P. Kochereshko, M. V. Durnev, L. Besombes, H. Mariette, V. F. Sapega, A. Askitopoulos, I. G. Savenko, T. C. H. Liew, I. A. Shelykh, A. V. Platonov, S. I. Tsintzos, Z. Hatzopoulos, P. Lagoudakis, P. G. Savvidis, C. Schneider, M. Amthor, C. Metzger, M. Kamp, S. Hoefling, and A. Kavokin, *Phase diagrams of magnetopolariton gases*, arXiv:1309.6983 [cond-mat], Sep. 2013 (under review in Nature Scientific Reports)

Conference proceedings

- A. Askitopoulos, H. Ohadi, P. Savvidis, H. Zaharias, A. Kavokin, and P.G. Lagoudakis, Condensation of polaritons through optical confinement: increased coherence and reduced threshold, CLEO: 2013, p. CM2M.5

- A. Askitopoulos, H. Ohadi, T.C. Liew, Z. Hatzopoulos, P. Savvidis, A. Kavokin, and P.G. Lagoudakis Ultra-fast spinor switching in polariton condensates, CLEO: 2014, p. STu3O.3

- P. Cilibrizzi, H. Ohadi, T. Ostatnicky, A. Askitopoulos, W. Langbein, and P.G. Lagoudakis*A study of the formation of dark-solitons in semiconductor microcavities*, CLEO: 2014, p. STu2O.3

Unpublished

- A. Askitopoulos, T.C.H. Liew, N. Berloff, Z. Hatzopoulos, P.G. Savvidis and P.G. Lagoudakis, *Non-resonant optical control of a spinor polariton condensate* (paper under construction)

- A. Askitopoulos, Z. Hatzopoulos, P.G. Savvidis and P.G. Lagoudakis, *Transient energy relaxation and momentum narrowing induces dispersion linearisation in a trapped polariton condensate* (paper under construction)